Electronic Thesis and Dissertation Repository

8-10-2021 10:00 AM

Biomaterial for Cervical Intervertebral Disc Prosthesis

Helium Mak, *The University of Western Ontario*

Supervisor: Wan, Wankei, *The University of Western Ontario*
A thesis submitted in partial fulfillment of the requirements for the Doctor of Philosophy degree in Biomedical Engineering
© Helium Mak 2021

Abstract

Recent long-term follow-up studies have shown that the cervical disc arthroplasty treatment have potentials in developing surrounding heterotopic ossification (HO). While its cause requires further investigation, this thesis has hypothesized that it may be the result of the continual remodeling of the injured vertebrae caused by the prostheses with smaller footprints introducing abnormal stresses. The research objective of this thesis is to develop a new prosthesis material that can be molded into any form conforming to the size and shape of the end-plates of the affected patient vertebrae. For prototype development, a composite material consisting of 10wt% polyvinyl alcohol cryogel (PVA) with embedded long circumferentially oriented bamboo fibers was proposed. An analytical model developed predicts that the compressive strength of such prosthesis is a monotonous increasing function of the fiber volumetric content. Specimens containing volumetric bamboo fiber contents of 0v% (control), 0.6v% and 3v% with 1xPBS were prepared for assessment. The cranial compressive and torsional viscoelastic behavior of specimens were studied with emphasis on its large-scale (till yield) characteristics measured under different strain rates. The mechanical properties measured are compared to that of kangaroo C5-C6 IVDs as our animal model.

Mechanical properties such as torsional stress, strain, modulus and impact resistance for viscoelastic materials are not well defined in literatures. This thesis has proposed new definitions for these properties and their derivation methods.

It was found that the cryogel process had resulted in a 37v% shrinkage of the composite material which may have caused the bamboo fibers to wrinkle up. A pre-strain of 35% to 45% of the specimens was required to unwrinkled the mid portion of the 3v% composite to match the strength prediction of the analytical model and that of the animal IVD. However, the fiber has not increase much of the torsional strength.

With a higher fiber content (e.g., ~5v%), this material may provide the compressive strength comparable to that of our animal model. A prosthesis fabricated with this composite material will be functionally comparable to a class of FDA-approved IVD prostheses with the

advantages that it can be molded quickly into patient specific size and shape with no spinal axil rotational alignment required.

Keywords

Intervertebral disc, cervical IVD prosthesis, compressive and torsional viscoelasticity, impact resistance, kangaroo cervical IVD, polyvinyl alcohol cryogel, bamboo fiber characterization, composite compressive modeling.

Summary for Lay Audience

The intervertebral disc (IVD) that is sandwiched in between two vertebrae serves to support the body weight, to provide spinal mobility and to provide shock-absorption in the spinal column. Cervical IVD failure could be caused by neck injuries resulting from traumatic incidents such as in automobile collisions, sports and uncontrolled falls, and the aging process. IVD replacement is often required for correction. Long term follow-up studies have identified problems related to postoperative abnormal bone growth around the device, known as heterotopic ossification (HO), which may be the result of the continual remodeling of the injured vertebrae caused by the prostheses with smaller footprints. The research aims at developing a new prosthesis material that can be molded into any form conforming to the size and shape of the end-plates of the affected patient vertebrae. The new material will have mechanical properties closely matching that of the native IVD. Properties of the IVD from kangaroo, a bipedal mammal with posture similar to human, will be used to guide this development. We have prepared a polyvinyl alcohol – bamboo fiber composite hydrogel using the low temperature thermal cycling process that has mechanical properties within the range of interest for IVD device development. Prototype IVDs were designed and fabricated

iii

using this composite hydrogel with 3 different fiber contents. Their mechanical properties were evaluated with reference to properties derived from the kangaroo data. Our results showed that the trends of compressive and viscoelastic properties of the composite hydrogel closely parallels to that of the animal model. An increase in the bamboo fiber contents in the prototype may provide the mechanical properties required based on our animal model data. Based on our study, it may be possible to create an improved IVD device using our design and composite hydrogel material developed that is functionally comparable to currently available IVD prostheses but would overcome the postoperative HO problems encountered. In addition, patient specific manufacturing could also be envisioned.

Co-Authorship Statement

 The "Summary for Lay Audience" section had been totally redrafted by Dr. Wan so that it can fit within the word limit required.

I was responsible for the remainder of the work in the development of the theories and mathematical models involved, the design of experiments and tools required, the preparation of specimens and conducting the experiments, the results capturing, performing data analysis and developing the software codes in MATLAB for data analysis.

Acknowledgments

Table of Contents

List of Tables

List of Figures

List of Abbreviations

Abbreviations used in Chapter 2

Abbrev.	Full name	Explanation
ACDF	Anterior Cervical Discectomy and Fusion	The common surgical treatment for cervical disc problem by removing the damaged disc and fusing the two adjacent vertebrae together with a bone graft. The surgery is performed from the front of the neck.
ASD	Adjacent Segment Degeneration / Disease	Disc degeneration or disease above and below a given index level that has been treated with ACDF or CDA.
COR	Center of Rotation	It is the center of rotation of the superior vertebrae in relative to the inferior vertebrae in a spinal motion. The instantaneous location of the COR of a natural IVD can change during a complex spinal movement. For an IVD prosthesis, the extends of the movement and the capability of supporting variable instantaneous COR in comparison with a natural IVD can be a measure on the quality of vertebral motion provided by the prosthesis[31].
FDA	Food and Drug Administration	A US government authority to approve drugs and medical devices to be used in US.
HO	Heterotopic Ossification	Abnormal bone growth from the adjacent surfaces of the vertebrae of an IVD. For a CDA device, they are typically formed postoperatively surrounding the

		metallic endplates of the prosthesis. The degree of HO is typically graded using the McAfee[23] classification: • Grade 0: no HO observed • Grade 1: HO present but within the baseline of the CDA device • Grade 2: HO developed beyond the baseline of the CDA device but not sufficient to interfere with ROM • Grade 3: HO developed with some degree of interfering with the segmental ROM • Grade 4: HO formation bridging the gap of the CDA device leaving < 3° of flexion-extension movement.
IDE	Investigational Device Exemption	An FDA process to allow the clinical trial of a medical device prior to its approval. The trial is typical for 2 years.
JOA[32]	Japanese Orthopedic Association	A patient self-evaluated clinical score to establish criteria for mild, moderate and severe impairment. In some clinical studies a modified shorten version are used (mJOA).
KL[33]	Kellgren-Lawrence Grading System for Osteoarthritis	A grading system for the severity of osteoarthritis in joints from interfering with their mobility function. It is also used in classifying the pre-operative condition of the vertebrae sandwiching a target IVD for treatment. The gradings of severity are from Grade 0 to 4 similar

		to that of the McAfee system on HO. Grade 0 is no osteoarthritis. Grade 1 is doubtful and Grade 4 most severe.
NDI	Neck Disability Index	A clinical score completed by the patient to access the severity of neck and upper back pain to evaluate how do they affect the patient's everyday life. It consists of a set of 10 questions, each contains 6 graded answers for the patient to choose from.
Odem's criteria[34]		A typical surgeon's perspective on the surgical outcome, which is either poor, fair, good or excellent.
ROM	Range of motion	Mobility of the spine. In many clinical studies, it is typically measured on the sagittal plane using dynamic radiographic techniques.
SF-12 SF-36	Short Form Survey on 12 or 36 items	A patient completed questionnaires to evaluate the quality-of-life measures. It may contain a physical component summary (PCS) and mental component summary (MCS) scores.
VAS[35]	Visual Analog Scale	A patient self-evaluated clinical score to measure the degree of pain. The scores are recorded by making a mark on a 10 cm line ranging from no pain (left most) to worst pain (right most).

Abbreviations used in Section 3.3.2

a	Lateral width of IVD
b	Posterior-anterior depth of IVD
h	Height of IVD
A	Area of IVD = $\pi ab/4$
V	Volume of IVD = Ah
τ	Applied torque on the IVD
θ	Angle of rotation of the IVD
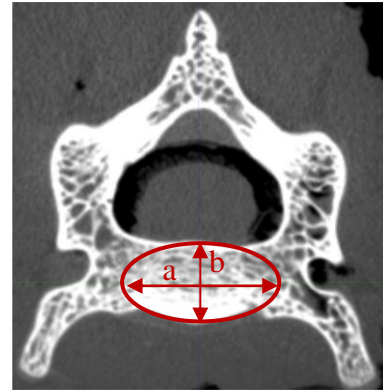
Abbreviations used in Section 4.6

Variable	Definition
Sub_C	Subscript C represents entities in circumferential direction
Sub_N	Subscript N represents entities in normal/vertical direction
R_o	Original radius of the cylinder
L_o	Initial half height of the cylinder
F	Applied compressive force
R_m	The radius at the mid-section of the barrel
r_m	Radius of the circular cross-section at a distance z.
r	Radial distance from origin
L	Half height of the barrel at half compression distance $\varDelta z$
z	Vertical distance from origin
α_L	Ratio L/L_o, degree of compression in height
α_R	Ratio R_m/R_o, degree of expansion in radius
ε	Strain
σ	Stress
E	Young's modulus
e	Energy
f	Force

Abbreviations used in Section 0

Variable	Definition
Sub_m	Subscript m stands for matrix entity
Sub_f	Subscript f represents fibre entity
A	Cross-sectional area of the slice perpendicular to the tensile force
p	Volumetric percentage
F	Force
ε	Strain
E	Young's modulus

<div align="center">Chapter 1</div>

1   Research Objectives and Background

This Chapter outlines the motivation, research objective and scope of research.

1.1   A Brief Background on Cervical Disc Arthroplasty (CDA)

1.1.1   Anatomy and pathologies of our intervertebral discs

Our spine consists of 33 vertebrae and 23 intervertebral discs (IVDs). Physiologically it is divided into 5 regions: cervical(C), thoracic(T), lumbar(L), sacral(S) and coccyx. There are 7, 12, 5, 5 and 4 vertebrae in each region respectively. The vertebrae are identified by their position number in the region. For example, C1 to C7 for the 7 cervical vertebrae. There is an IVD located in between each pair of vertebrae from C2 to S1. The vertebrae in sacral and coccyx region are fused together. An IVD is identified by the pair of vertebrae it is sandwiched in between. For example, IVD C5-C6.

The IVD is a fibrocartilage tissue. Its main functions are to support the body weight, absorb shock waves from damaging our brain and provide the spinal mobility such as in flexion/extension, lateral bending and rotation. Anatomically it consists of two regions: an outer anulus fibrosus (AF) enclosing a nucleus pulposus (NP) (Figure 1-1). The AF has a laminar structure. Each lamella consists of almost parallel type I collagen fibers running at an angle approximately 30° to the horizontal. The angle reverses direction from one lamella to another forming a crisscross pattern to resist compressive and torsional forces. The NP is a gel-like material consists of mainly proteoglycan and water held together by a network of type II collagen fibers and elastin. Combining the almost impermeable nature of the AF and the incompressible gel-like nature of the NP, the IVD provides a good viscoelastic compressive and impact resistant properties to support the bodily weight and external impact forces. Unfortunately, the water content of the NP decreases as one ages. At one's childhood, the NP is fully hydrated. A normal compressive force is evenly shared between the AF and NP across the entire surface of the IVD in contact with the vertebrae. As one ages, the proteoglycan and water content decreases and the load of a normal compressive force is gradually shifted towards the AF.

The height of the IVD decreases. The AF may also be compromised due to inflammation, prolong daily activities or simply by wear and tear throughout our life. The NP contents may be squeezed out from a weakened part of the AF forming different degree of bulging and herniation. As the spinal cord is located posterior to the IVD, a heavy traffic of neural network runs in-between the gaps provided by the IVDs from the spinal cord to our entire body. As the height of the IVD decreases or it becomes herniated due to aging or other factors, there is a possibility that some nearby nerves may get pinched (radiculopathy) or the spinal cord get compressed (myelopathy). This may cause intractable pain to the person. The whole symptom is called degenerated disc disease. In addition, our IVD can also be damaged in impact-prompt sports such as weight lifting, American football, basketball etc., traumatic incidents such as in an automotive accident or uncontrolled falls such as slipping. Professions like heavy laborers or soldiers are more likely to have IVD problems.
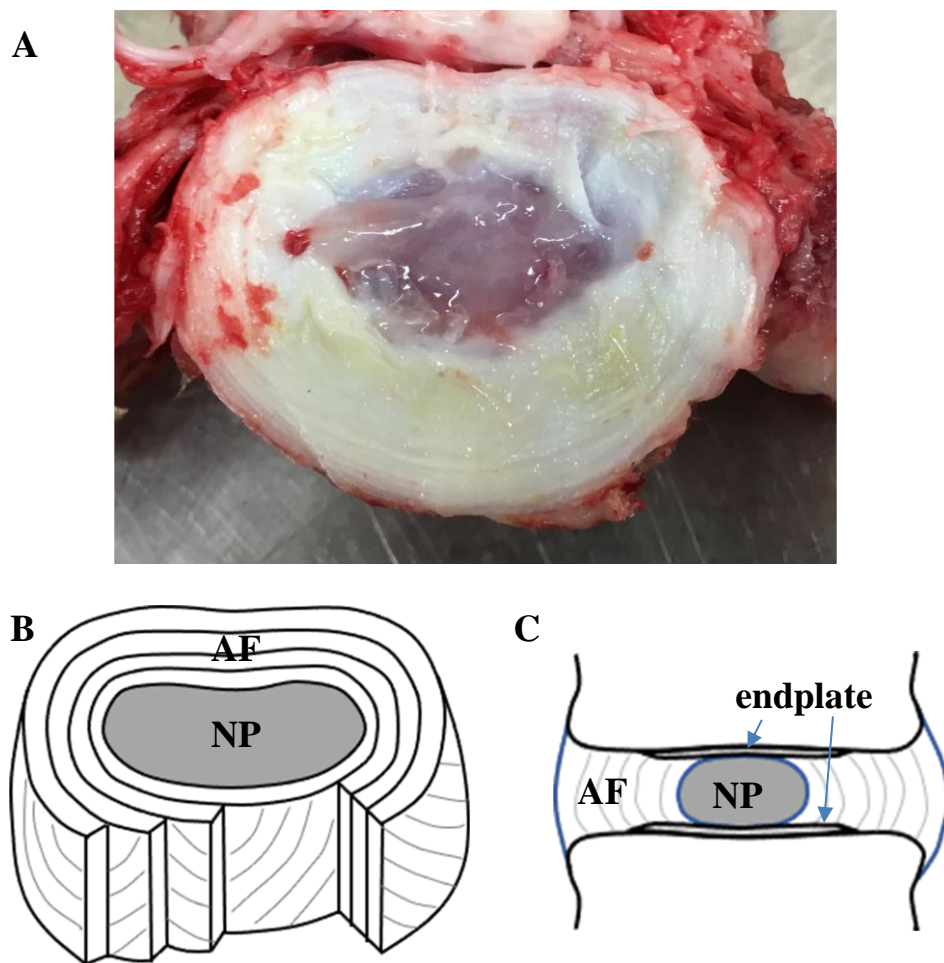
Figure 1-1: Anatomic structure of an IVD

A: A horizontal cross-section of a porcine C5-C6 IVD showing the laminar structure of the AF enclosing the gel-like nature of the NP.

B: A cut-out view of the AF laminae showing the alternate angle arrangement of the Type 1 collagen fiber from one lamina to another.

C: A vertical cross-section of the IVD showing the cartilaginous endplates and the vertebrae housing the IVD.

1.1.2   Cervical surgical treatment

Typical first treatments of pains originated from a damaged IVD is via physiotherapy or medication to relax the surrounding tissues or numb the pain. If the pain persists, surgical treatments may be required to replace the damaged IVD to decompress the pinched nerves. The long standing standard surgical treatment for the cervical IVDs is the anterior cervical discectomy and fusion (ACDF). The IVD is surgically removed from the anterior position and replaced with a bone allograft to restore the natural height of the replaced disc. In some cases, the bone graft is held in position by an anterior cervical metal bracket (e.g., Caspar plating) to attach to the adjoining vertebrae body to stabilize the fusion site. Patient's live bone cells are added to the allograft to encourage the fusion of the vertebrae bodies and the graft. Even though this approach relieves the pain caused by the damaged/deteriorated IVD, the fused vertebrae will reduce the range of motion (ROM) of the spine. Long term problems are reported to cause the adjacent IVDs to deteriorate, a phenomenon called adjacent segment degeneration[1] (ASD). To address this issue, an emerging treatment is to replace the damaged IVD with a prosthetic device.

1.1.3   CDA devices

The aim of these prostheses is to restore some spinal mobilities apart from supporting the bodily weight. A group of FDA(US) and CE(EU) approved devices have been developed in the past 30 years improving in capabilities in mimicking the mechanical behavior/properties of a human IVD. Earlier designs of the IVD prostheses employ a simple ball-and-socket or ball-and-trough joint (e.g., Prestige-ST[Section 2.3], ProDisc-C[2]) to provide the rotational capability. Second generation designs (e.g., Bryan [Section 2.1]) provide more degrees of freedom and have compressive and rotational elasticity/resistivity in spinal mobilities. More recent ones (e.g., M6-C [Section 2.2], CP-ESP [Section 2.5]) may have some degree of viscoelasticity, impact resistance and variable instant center of rotation capabilities.

To anchor the device onto the inferior surface of the cranial and superior surface of the caudal vertebra bodies (adjacent surfaces), most designs employ a pair of metal endplates with anchoring features[3] like keel, spikes, teeth, rails, ridges and screws. The main

function is to prevent the movement of the device especially from affecting the posterior longitudinal ligament, which protects the spinal cord. As the devices come only in a set of standard sizes, to surgically insert the device, after the removal of the IVD, a suitable size is selected to fit the space available. The adjacent surfaces may have to be machined to conform with the shape of the devices and to accommodate the anchoring features. This will cut into the cortical and cancellous bone of the vertebra bodies. This may trigger the continual remodeling of the vertebral bodies[3].

Popular materials[4] for the metal endplates are titanium alloys (e.g. TiAlV), stainless steel alloys (e.g. 316LV) or cobalt chromium alloys (e.g. CoCrMo). The surfaces of the device in contact with the vertebral bodies may be textured and chemically coated[3,4] with calcium phosphate (CaP), hydroxyapatite and plasma-sprayed titanium (CPTi) to aid the osseous integration with the vertebral bodies.

The middle layer that articulates the mobility of the prosthesis may consist of sliding surfaces[3] (e.g., ball-and-socket, ball-and-trough), which, according to the materials used, can be classified as metal on metal (Prestige ST), metal on polymer (e.g. UHMWPE or polyurethane) (Bryan [Section 2.1], ProDisc-C[2], ProDisc Vivo[5]), ceramic on polymer or ceramic on ceramic (Prestige-LP [Section 2.4]) types. These designs may have wear and tear concerns that produce harmful debris[6]. To address the debris issue, some designs (Bryan, M6-C) include a cover-up membrane to enclose the entire middle layer to prevent the debris from leaking out to the surrounding. Some designs consist of multiple components (Bryan or M6-C) or a single block (CP-ESP).

1.1.4 Pathological studies on CDA

Even though the benefits of ACDF vs CDA treatments are still under debate[7–11], the FDA(US) & CE(EU) approved devices have reported benefits to the patient in clinical studies[2,5,20,12–19]. Most of these reports are follow-up studies for postoperative results less than 10 years. This may be due to the relatively short history of devices in this field. A few reports of longer periods are coming out. Benefits reported include maintaining physiological segmental spinal motion, improved preoperative clinical scores (Neck Disability Index, Odom Criteria, Visual Analogue Scale, modified Japanese Orthopedic

Association scale, Short Form-12/36 PCS/MCS, etc.) on pain, health and quality of life, lower rate of secondary revision surgeries, shorter hospital stay, lower incidents of adjacent segment disease and degeneration, more cost effective[21], etc. Even in studies of less than 10 years and later validated in longer follow-up studies, reported problems include adjacent segment disease and degeneration[17,22](ASD), heterotopic ossification[17,19,22–24] (HO) of Class 3 or 4 in the McAfee classification[25], increase Class 4 HO in time[19,26], subsequent fusion or spontaneous ankylosis[22], reduced ROM[17,22], postoperative kyphosis[18,27], myelopathy and radiculopathy[17]. The nature of all these studies was qualitative, the precise causes of these culprits remain unclear. Some studies tried to correlate clinical observations with postoperative occurrence of ASD and HO. Existence of preoperative conditions of ASD[13] and HO[23] may lead to the development of similar postoperative conditions[26]; low preoperative lordosis with low postoperative ASD[7]; kyphosis of the prosthesis with HO[18]; patients with postoperative anterior or enlarging osteophyte formation with upper ASD[18], prostheses with anterior lips with lower occurrence of anterior HO[23] (Bryan & Prestige ST/LP vs PCM), design of prostheses with degree of HO (Bryan 49%, PCM 80%, Prestige LP 60%)[23], preoperative ossification with HO in the posterosuperior disc space[23], etc.

1.2   Motivation and insights of this research

From the above-mentioned pathologies observed on CDA, apart from existence of preoperative conditions, postoperative ASD & HO are likely to be induced by the prosthesis. This shows that there are rooms for further improvements on current devices.

Borrowing knowledge from other fields of orthopedic research[28,29] and biomechanics may bring some insights into possible improvements affecting the occurrence of postoperative ASD and HO. A possible cause may be these devices have introduced foreign level or type of stresses to the adjacent vertebrae. The injured vertebrae just keep remodeling to respond to these foreign stresses, HO, and these foreign stresses may affect adjacent level IVDs to promote their deterioration, ASD.

From the view of this angle, there are a few observable drawbacks of existing prosthesis devices.

Smaller footprint introducing concentrated stress

All IVD prostheses come in a set of standard sizes. All fitted devices must be smaller than the space available of the replaced IVD. This means the body weight is now concentrated into a smaller area, producing a higher level of stress in the middle of the vertebral body instead of evenly spread over the entire adjacent surfaces of the vertebrae. With the machining of the vertebrae surfaces for installing the devices, the cortical bone may be removed exposing the full concentrated stress to the much weaker cancellous bone of the vertebra body. The surrounding remaining areas of the fitted device are exposed. There is no stoppage for the continuing ossification formation for the vertebrae to heal themselves.

Fixed axes and center of rotation

To provide rotational freedom, most existing IVD prostheses use a design similar to ball-on-socket that has fix axes and centers of rotations, while our IVDs can provide 6 degree of freedom in motion capable of having variable axes and centers of rotations. The restrained freedom of movement introduced by these prostheses require careful axes alignment with the spine during the surgical insertion. Even with perfect alignment, and worse if not, they will produce foreign torsional stresses on the vertebrae/spine during spinal movements.

Mismatch device endplate material strength with vertebrae

Stanton et al[4] tabled the Young's modulus of the cortical and cancellous bone of the vertebrae body to be 15,000 MPa and 1000 MPa respectively. The Young's moduli of common endplate material of devices for titanium alloy (TiAlV), stainless steel (316LV) and cobalt chrome alloy (CoCrMo) are 100,000 MPa, 200,000 MPa and 230,000 MPa respectively. The metal endplates materials are much stronger than those of the vertebra bones. For IVD prostheses using a metal-to-metal articulation (e.g., Prestige-ST and Prestige-LP), any compressive strain at the index level will be mainly borne by the adjacent vertebrae instead of the prostheses.

1.3   Research objective, focus and approach

1.3.1   Research objective

The central idea of this research is on the proposal and evaluation of a new prosthesis material. The prosthesis is constructed from a composite material of polyvinyl alcohol cryogel (PVA) with embedded long circumferentially oriented bamboo fibers spiraling from bottom to top. The length of the fiber should circle the circumference of the prosthesis at least once. The PVA is chosen because of its biocompatibility, long-term stability and moldability into any patient specific IVD shape. The prosthesis when under compression, assuming the incompressibility of PVA, the mid-height portion of the prosthesis will bulge out creating tensile forces on the embedded fiber, hence increase the compressive strength of the prosthesis. When under torsion, the torsional strain may stretch the circumferentially and spirally oriented fibers putting them in tension, hence producing torsional strength. The compressive and torsional strength of this prosthesis material will be tunable to match that of any IVD required by increasing or decreasing the fiber contents.

Benefits of this prosthesis material will be the abilities of quickly (around a week) moldable into any patient specific shape, strength tunable to match the requirement of any IVD level, biocompatibility, long-term stability, single block structure and have variable center of rotations. These may address many drawbacks of existing prosthesis.

The objective of this research is to perform a feasibility study on evaluating if this new material can be a viable material for IVD prostheses.

1.3.2   Research focus

Focusing this research into certain area is to conserve research resources and time into a manageable level without loss of generality.

Focus 1: IVD C5-C6

Our spine has 23 IVDs. For a feasibility study on the new prosthesis material, there is no need to match the properties of all 23 IVDs individually simultaneously. This repetitive

work can be left for future work once this research has validated the concept. Hence this research will focus only on studying the properties of the IVD C5-C6 as the target. The techniques developed can apply to any IVD without loss of generality. Many studies already exist on the lumbar section, while the cervical section was reported to lack similar studies[30]. In addition, IVD C5-C6 has noticeably higher instances of surgical treatments than other levels among CDA studies[16,17] signifying the higher relevance of this IVD among others in the cervical region.

<u>Focus 2: Large-scale viscoelastic cranial compressive and torsional properties</u>

Our IVD provides 6 degrees of freedoms (DOF). In terms of externally applied excitation strains, they can be compression, shear and torsion in any of the 6 DOF. This study will focus on cranial compression and torsion. Many existing studies are performed on excitations within physiological limits and on determining the size of neutral zones. To complement the existing knowledge in this area, this study will focus on characterizing the large-scale unrestricted (all limiting structures and tissues removed) viscoelastic behavior of IVD from zero to yield situation. This may contribute to the research in cervical spinal behavior during a traumatic event such as in a whiplash injury study.

1.3.3   Out of scope area (OOSA)

Out of scope areas outlines research works to be performed for future studies not included in this one. These areas may require special knowledge or areas of interest but may be better to be studied in as separate studies that are not directly related to the objective of this research.

<u>OOSA 1: Prosthesis attachment method</u>

One key concept on the design of this new prosthesis is to eliminate the metallic endplates used in existing CDA devices. This will eliminate the need to cut into the adjacent vertebra bodies for its installation. With the matching material properties of existing IVD, the prosthesis may be transparent to the vertebrae as if a real IVD is in place. This may reduce the occurrences of postoperative HO and ASD. For attachment to the affected vertebra bodies, the superior and inferior surfaces of this new prosthesis

should have the shape exactly matching that of the adjacent vertebrae surfaces of the patient CDA site. In addition, these surfaces may be molded to have shallow pockets to grip the vertebra bodies in contact and hold the prosthesis in position under compression. The shallow pocket idea is similar to existing IVDs as shown in Figure 1-1C. To further increase its holding strength, a suitable adhesive may be added in a short-term solution. For a long-term solution, these surfaces of the prosthesis can be functionalized to encourage osseous integration with the vertebral bodies.

OOSA 2: Patient specific molding of prosthesis

The cross-linking of the PVA solution into hydrogel using freeze-thaw cycles require to have the PVA solution contained in a water tight mold that allows for heat exchange. This mold can be made starting from the CT scan of the patient's affected vertebrae intended for CDA treatment. Using an image processing software in the medical field (e.g., 3D Slicer or MicroView), the surface geometry of the two vertebrae can be extracted through segmentation techniques. The vertebral bodies can be pull apart to a distance satisfying the decompression requirement. The geometry of the IVD prosthesis required can be created by filing the space between the vertebrae. The geometry of the mold can be made by subtracting the volume of this prosthesis within in a block of material of dimensions large enough to cover the entire prosthesis. Air holes and a removable cover can be incorporate into the mold. The final geometry of the mold can be sent to a 3D printer to make the mold. The feasibility of this concept has been evaluated using the 3D Slicer in creating the mold geometry but hasn't physically 3D-printed it out. As the actual geometry requirement of the prosthesis will be a result from OOSA 1. In addition, the mold geometry has to be adjusted to accommodate any shrinkage of the PVA hydrogel to obtain the desired geometry of the intended prosthesis. This research is left as a future study.

1.3.4   Research Approach (RA)

Research approaches refer to the selected methods used on this study on how to carry out the evaluation on the suitability of the new proposed material.

RA 1: Kangaroo IVD C5-C6 as animal model

The key underlying concept on this feasibility study is to measure and compare the compressive and torsional viscoelastic behavior and strength of the new prosthesis material to that of human IVD C5-C6. Unfortunately, large quantities of uniform human IVD C5-C6 specimens are difficult to obtain, the kangaroo IVD C5-C6 is used instead. The choice is based on the kangaroo's similarity to human in bi-ped upright standing posture, height and weight.

RA 2: Model based approach in fiber selection

Instead of blindly testing a matrix of different combinations of different types of fibers and fiber contents to access their suitability for the prosthesis to meet the target viscoelastic behavior and strength of kangaroo C5-C6 IVD measured, a model-based approach is adopted to minimize this effort. A rough analytical model was first developed relating the compressive strength of the prosthesis as a function of fiber strength and fiber content. In this analytical model, the prosthesis geometry was modeled as a simple short cylinder to simplify the mathematical derivations. Base on this model and the mean yield strength measured from the kangaroo IVD, one can roughly determine the fiber characteristics needed for preparing the prosthesis specimens for testing, such as fiber length, the tensile strength (Young's Modulus) and the volumetric content in the prosthesis.

RA 3: Validating strategy on the strength tunable nature of the prosthesis

The ultimate goal of this study is to determine the volumetric content of the fiber to match that of the kangaroo IVD measured. However, this will require a large number of batches of specimen with different fiber contents to be prepared and testing efforts to perform binary searching to determine the correct volumetric fiber content required. This will involve too much testing efforts. Instead, this feasibility study took a different but just as effective approach. The validating strategy was performed to validate the monotonic increasing nature of the prosthesis compressive strength with volumetric fiber contents as predicted by the analytical model. Once the tunable nature is established, one

can perform the binary search as future works. With this strategy, only three batches of specimens of three volumetric fiber contents (0v%, 0.6v% and 3.0v%) are required. This has simplified the specimen preparation and testing efforts.

1.4   Chapter layout & summary

This thesis consists of 5 chapters. Apart from Chapter 1 Background introduction, Chapter 2 literature review and Chapter 6 Conclusion, Chapter 3 to 5 contain the research work in this study. These three chapters are written in the paper manuscript format such that they can be individually extracted to become a publishable paper. Hence, when describing the motivation of the research, there may be some duplications in these chapters. Each of these three chapters includes an abstract for the chapter and sections for introduction, methods & materials, results, discussion and conclusion. A brief list of research objectives is included in the beginning of each Chapter to highlight the research focus (foci) of the Chapter.

Chapter 1

This Chapter contains a brief background on CDA, the motivation for this research, its objective, focus, approach and out-of-scope areas.

Chapter 2

This Chapter provides literature review of currently FDA approved, CE certified and experimental IVD prostheses relating to this research.

Chapter 3

This Chapter measures the compressive and torsional viscoelastic properties of kangaroo IVDs C5-C6 with all movement restraining bone structures, muscles and tendons removed (unrestricted). The measured properties are used as the gold standards for the prosthesis specimens to compare with in Chapter 4 and 5. The individual geometries (height and area) of each IVD are obtained by micro-CT scans. The individual yield stress and yield strain are measured with a bi-axal material tester. As viscoelasticity is the key material property of concern, a technique using a polynomial viscoelastic surface is

introduced to model the collective viscoelastic behavior of all the kangaroo IVDs measured.

A few viscoelastic material properties, such as impact resistance, torsional stress and strain, are not well defined in the literature. This Chapter attempts to propose new definitions to these material properties.

This Chapter also introduces a new method for deriving mathematically the impact resistance of a viscoelastic material from its viscoelastic surface when subjected to an impulse stress of a given waveform. To demonstrate this method on the kangaroo IVDs, this Chapter uses a set of simple sawtooth impact stresses of increasing peak values to derive the impact resistance value in each case. With the new definitions for torsional stress and strain, the impact resistance derivation can apply to both compressive and torsional cases.

Chapter 4

The foci of this Chapter are to characterize the compressive viscoelastic behavior of a proposed new composite material formed with 10wt% PVA and bamboo fibers and to evaluate its suitability as an IVD prosthesis material candidate basing on the results obtained from the kangaroo IVDs.

It derived a rough analytical model on the compressive behavior of the new prosthesis material proposed. From this model, using 10wt% PVA as the matrix, it determines the tensile modulus and the volumetric contents of the fiber required to achieve the strength of the kangaroo IVD measured.

Using a small random sample (n=19) of the bamboo fiber, it measured the geometric and tensile properties of the bamboo fiber and validated it is a suitability fiber candidate basing on the requirements derived from the analytical model.

The compressive properties of 3 batches of specimens with 0v%(control), 0.6v% and 3v% fiber contents were measured using a set of different strain rates. The monotonic increase of compressive strength of the specimen with increase of fiber volumetric

content was validated. The viscoelastic nature of the specimens was evaluated using the test results of the batch with 3v% fiber content.

The test results of the 3v% specimen batch were found weaker than the model prediction. This Chapter hypothesized that the main cause of this was due to the 37% volumetric shrinkage of the PVA hydrogel during the 6 cycles of freeze-thaw process. As a result, the bamboo fibers had to be wrinkled up within. To achieve the strength predicted in the model, the specimens must be pre-strained to unwrinkled the embedded fibers. It had demonstrated that with a pre-strain value of 35% to 45% on the 3v% specimens, the final strength will match that of the kangaroo IVDs.

Chapter 5

This Chapter contains the characterization on the viscoelastic torsional behavior of the proposed new prothesis material and evaluates its suitability as an IVD prosthesis material basing on the results obtained from the kangaroo IVDs.

The torsional stress and strain values measured had used the same definition as in the kangaroo section.

The torsional stress-strain behavior of 3 batches of specimens containing 0v%(control), 0.6v% and 3v% fiber contents were measured using a set of different torsional strain rates.

It had found that the specimens had very low torsional strength (<1 MPa) as compared to that of the kangaroo IVDs measured (~13 MPa). The fiber content had close to no effect on the torsional strength of the specimens. It postulated that the low torsional strength may be due to the 37v% shrinkage of the PVA matrix. With this shrinkage, the embedded fibers may be wrinkled up inside. To stretch back the fiber so that they can provide the tensile strength required in torsion, each layer of fibers has to subject to around 60° rotation. This angle of rotation is cumulative from the bottom to the top of the specimen. As the diameter of the fiber is around $21\mu m$, this will require a large torsional strain applied before a meaningful torsional stress can be obtained.

Even with low torsional strength but has sufficient compressive strength, this new material can be a viable material candidate for IVD prosthesis. Many existing FDA approved IVD prosthesis using a ball-on-socket design have similar properties. In addition, this material has the benefits that it can be molded into patient specific shape and size and has no fix axes and center of rotation.

Chapter 6

This Chapter contains a summary of the research findings, conclusion and proposed future works.

Chapter 2

2 Literature reviews on CDA prostheses

This section conducts a literature review on a set of CDA prosthesis devices. Some are FDA (USA) or CE (EU) approved devices and some are still in their experimental stage. They are selected basing on their popularity in published literatures and relevance to this research. The main review focus is on the long-term effects of these CDA devices especially on HO and ASD. It is conducted on a per device basis basing on the assumption that these long-term effects are partly due to their unique design and material used.

(**For abbreviations, see section "List of Abbreviations"**)

2.1 Bryan cervical disc

<u>Owner</u>: Medtronic Sofamor Danek, Memphis, TN, USA

<u>FDA approval</u>: Case P060023, May 12, 2009, single level

<u>Construction</u>[36,37]:
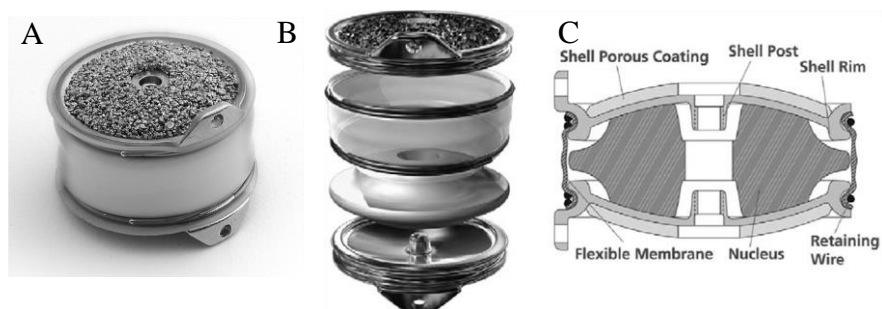
Figure 2-1: Bryan cervical disc*

Figure A shows the external view of a Bryan cervical disc showing its top and bottom titanium alloy endplates with the mid-section fully enclosed by a polyurethane sheath.

Figure B is an exploded view of the internal components of the device.

Figure C is a cross-sectional schematic view showing how each component fits together.

*A: Reprint from article[103] with permission from *Spine (license # 5077671114136)*

*B & C: Reprint from article[104] with permission from *Clinical Spine Surgery (license # 5077710310419)*

The Bryan cervical disc employs a double ball-and-socket construction providing two metal-on-polymer articulating surfaces at the top and bottom of the device for supporting rotational movements and compression. It has a polyurethane inner nucleus (99% polycarbonate-urethane, 1% silicon) sandwiched in between a top and bottom titanium alloy (Ti-6Al-4V) roughly circular shell. The top and bottom surfaces of the inner nucleus in contact with the outer metallic shells are part spherical. A circular pocket is made in the center of the top spherical surface and a smaller diameter metal post is inserted into the pocket from the center of the top shell. Same arrangement is made for the bottom spherical surface. Both arrangements provide a soft stop to limit the rotational movements of the device. The inner nucleus is totally enclosed in a flexible polyurethane outer sheath (94% polyurethaneurea, 6% silicon) filled with saline and fixed to the side of the top and bottom shells with retaining rings. The outer surfaces of the two shells are coated with commercially pure titanium beads (CP Ti B.I. Thortex K-coat) to provide porosity for promoting bone cell adhesion. Each shell has a small vertical anterior lip for anchoring the device onto the adjacent vertebrae body with a screw.

The device is available in 5 sizes of diameter from 14 to 18mm in 1mm increments and the resulting interbody height is approximately 6mm.

ROM & mechanical properties[37]:

- Flexion/Extension: ±10º

- Lateral Bending: ±11º

- Rotation: ±7º

- Translation: ±1 mm

- Axial compression: physiological 130N, max 1164N

Clinical studies:

A 24-months primary clinical study[37] (IDE#G00123) was conducted by Medtronic at 30 sites in US with patients operated on between May 28, 2002 to October 8, 2004 and the

study was concluded on June 5, 2006. The prime objective of this study was to support the FDA approval of the device by demonstrating it is non-inferior to the standard ACDF treatment. A total of 300 patients (160 BRYAN, 140 ACDF) had completed the 2-year follow-up study with evaluation points at 6 weeks, 3, 6, 12 and 24 months. The majority of the treated IVD levels were at C5-C6 (57.9% BRYAN, 49.8% ACDF) and C6-C7 (36% BRYAN, 42.5% ACDF). The evaluation was based on pre-operative (< 4 weeks before operation) and post-operative conditions on NDI, SF-36 (PCS & MCS), Neck Pain Score, Arm Pain Score, radiography (to determine the FSU height and fusion) and axial ROM (BRYAN only). The conclusion of the study on the BRYAN cervical disc was that most clinical scores and safety data were non-inferior to ACDF and with superiority in overall success, NDI results, lower rates of second surgical procedures related to supplemental fixations and lower second surgery failure rate. For axial ROM, the mean angular range of motion at 12- and 24-months values were 7.77º (n=226) and 7.74º (n=154) respectively in comparison to preoperative value of 6.43º (n=214).

Lei Cheng et al[38] had performed a 3 years follow-up study comparing with ACDF. Total 83 patients (41 BRYAN, 42 ACDF) were treated from December 2004 to September 2006 at one center. The study covered treatments at single level (58.5% BRYAN, 50% ACDF), 2 levels (34.1% BRYAN, 40.5% ACDF) and 3 levels (7.3% BRYAN, 9.5% ACDF). Evaluations were based on preoperative and postoperative scores of NDI, Odom's criteria, SF-36 and JOA scale taken at 1 and 6 week, 3, 6, and 12 months and 2 and 3 years. The study found BRYAN cervical disc had scored significantly better in NDI, SF-36 and mJOA evaluations. It had fewer complications than the ACDF group. Adverse complications included one dysphagia and one HO case.

Feifei Zhou et al[26], 5-year follow-up concluding that patients with severe preoperative spondylosis had higher rate of developing postoperative HO.

Justin Miller et al[20], 7-year follow-up study on the ASD effect. Basing on the ratio of the vertical disc height and the anteroposterior distance of the cephalad endplate of the vertebral body below the adjacent level disc, it had concluded that there was a significant decrease in disc height over time to indicate ASD in both the CDA and ACDF patients.

Gerald M.Y. Quan et al[13], 8-year follow-up on clinical and radiological results finding HO had tendency to increase from 17.8% at year 1 to 69.2% of Grade 3 & 4 at year 8. ASD was detected in 19% of the related treated segment but all patients had same preoperative conditions.

Suo Zhou Yan et al[7], 8-year follow-up study on the ASD effect. In comparison between CDA and ACDF patients, they found there had no significant differences of ASD incidents between the two groups (44.83% vs 48.72%). However old age, low preoperative overall and segmental lordosis were statistically correlated with ASD.

Yanbin Zhao et al[17] had performed a 10 years follow-up study in 1 center in China. Total 33 patients had completed the study with 25 patients treated at single level, 7 at 2 levels and 1 at 3 levels, total 42 levels included 3 @ C3-C4, 7 @ C4-C5, 26 @ C5-C6 and 6 @ C6-C7. The treatments were carried out between December 2003 to Jan 2005. Evaluations were based on pre- and postoperative mJOA, NDI, VAS scores and radiographic outcomes. This study found the mean ROM had decreased from 7.8° (immediate after treatment) to 4.7° at the 10-year point. HO was observed in 29 (69%) of the 42 levels, among which 14 (33.3%) at Grade 3 and 14 (33.3%) at Grade 4. A total of 63 adjacent segments were evaluated, of which 30 (47.6%) had developed ASD, but no patient suffered from ASD. It concluded that the HO was common in BRYAN cervical disc arthroplasty and patients might suffer reduced ROM.

Xiao Han et al[39], 10-year follow-up on the CDA effect on patients with myelopathy and radiculopathy. It reported the incident of Grade 3 & 4 HO was detected in 28.9% the myelopathy patients and 32.1% in the radiculopathy patients. Segmental kyphosis was detected in 21.1% of the myelopathy and 21.4% of the radiculopathy patients.

William F Lavelle et al[40], FDA IDE 10-year follow-up concluding that, in comparing CDA vs ACDF patients, a significantly higher overall success rate (81.3% vs 66.3%), significant improvement in NDI score and good improvements on VAS neck and arm score.

Vincent Pointillart et al[18] had performed a 15 years follow-up study in the University Hospital of Bordeaux in France. Total 18 patients (14 single level and 4 two levels total 22 implants) had completed the 15 years study. The locations of the implants were 2@C4-C5, 11@C5-C6 and 9@C6-C7. Treatments were performed between July 2000 to July 2001. Evaluation matrix included Odom's criteria, VAS, NDI, SF-12 (PCS & MCS) and radiological analysis. It had found 15 of the 22 (68.2%) implants had maintain mobility with $9^o \pm 3.9^o$ (range 4-15°) flexion-extension ROM. HO had developed in 12 of the 22 levels (54.5%), among which 11 (50%) were of Grade 3 & 4, and 11 of 18 (64.7%) patients had developed upper ASD. There was a positive correlation between kyphosis and HO occurrences.

Discussion

Medtronic had started the clinical trials of the BRYAN Cervical Disc in 2000 outside USA prior to the FDA approval, enabling it to have a longer (15-years) follow-up history in comparison to other devices. This had provided valuable opportunity to observe its long-term effects on patients. The common reported problems were HO, ASD and kyphosis.

The clinical studies had shown HO might have started to develop after year 2 and its severity had increased on time. Both the 10- and 15-year studies had shown over half of the patients had developed severe (Grade 3 & 4) HO. This may render the effective operation of the device, reducing ROM and clinical scores of the patients. Yong Jun Jin et al[23], by comparing BRYAN cervical disc with two other devices (PCM & Prestige-LP) in a 46-month investigation, had found BRYAN cervical disc had a lower HO incidence (49% vs 80% and 60%) and, might be due to its anchoring anterior lips, most HO occurred in the uncovered posterosuperior disc space. They had also attributed this development to the biomechanical compressive stress. This has linked the development of HO to the design of the device. In addition, the location characteristics of HO may also indicate that the smaller footprint issue may be a factor to consider. Vincent Pointillart et al[18] also linked HO with kyphosis.

ASD was also a common long-term problem, however Yanbin Zhao et al[17] in their 10 years follow-up study had found no patients had suffered from ASD.

2.2   M6-C™ Artificial Cervical Disc (M6-C)

Owner: Spinal Kinetics LLC, Sunnyvale, CA, USA

FDA Approval: Case P170036, February 6, 2019, single level

Construction[41,42]:
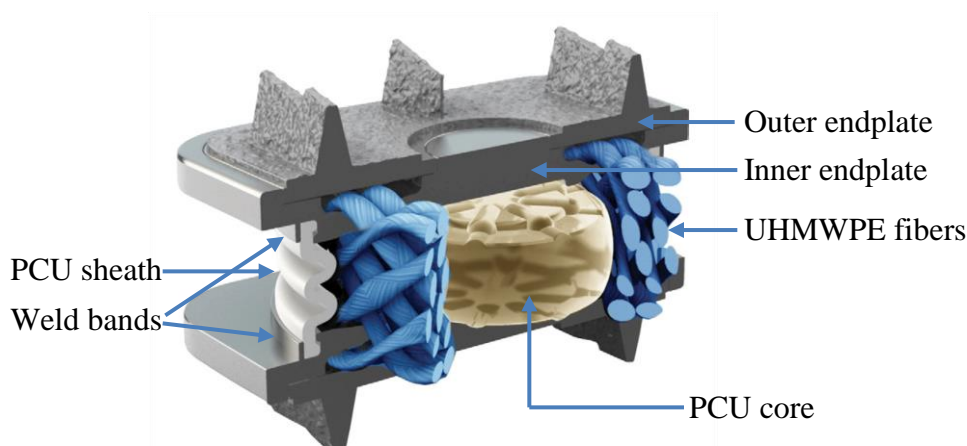
Figure 2-2: M6-C cervical disc*

A schematic view of the device showing its internal components and structure, especially its PCU core and how the UHMWPE fibers interweave and loop between the top and bottom outer endplates giving the device its torsional strength.

*Reprint from article[43] with permission from *International Journal of Spine Surgery*.

The M6-C was designed to have 6 degrees of freedom in movements with progressive resistances. It provides independent angular rotations in all three axes (flexion-extension, lateral bending and axial rotation) and translational movements in all three axes (anterior-posterior, lateral and axial compression).

It has a polycarbonate urethane (PCU) core sandwiched in between, in contact with but not affixed to, a top and a bottom titanium alloy (Ti6Al4V) rectangular internal endplate.

Multilayers of strong polymer fibers (UHMWPE) were weaved in a wavy up-and-down interlocking pattern surrounding the PCU core forming a simulated annulus. The polymer fibers effectively elastically tie the relative movements of the upper and lower internal endplate together. The whole mid portion of the device is enclosed in a flexible PCU sheath to prevent debris, if any, from leaking outside. The sheath is retained by two circular Ti6Al4V bands welded onto the inner endplates. Two outer Ti6Al4V endplates with low profile anchoring fins are also welded onto the inner endplates. The external surfaces of the outer endplates are coated with titanium plasma spray to enhance bone cell adhesion.

M6-C comes in 4 width x depth combinations (15x12.5mm, 15x15mm, 17x14mm & 17x16mm) and 2 heights (6mm & 7mm) each making totally 8 sizes.

Characteristics[42]:

- Axial compression: $\geq$ 3.2kN (@ 0.2mm/s, no failure to 25kN)
- Compression-shear: $\geq$ 845N (45º with device in 7.5º extension @0.01mm/s, max yield 6714 $\pm$ 113N)
- Torsion: $\geq$ 4 Nm (@0.5º/s, max yield 10.26 $\pm$ 1.23 Nm)
- Axial compressive creep: inter-endplate distance $\leq$ 1.0 mm under 100N extrapolated to 100 years (100N for 42 days followed by a simulated 10 days of sleep/wake cycle of 100N for 16hr and 53N for 8hrs)
- Lateral and anteroposterior translation: $\leq$ 3.5 mm (shear load 2kN + axial compression 100N)
- The flexion-extension load-displacement curve (torque vs angle) compared favorably with an intact human C5-C6 IVD.

Clinical studies:

Owner had performed a 2 years 12 sites investigational study in US (IDE#G050254) for its FDA approval application. A total of 206 patients (152 M6-C, 46 ACDF) were treated between May 2014 and June 2016 and had completed the full study period. 98 ACDF

patients' data from a previous study was included to boost the total number of ACDF patients to 144. The majority of the treated IVD levels were C5-C6 (51.3% M6-C, 54% ACDF) and C6-C7 (40% M6-C, 38.6% ACDF). The study had concluded in May 2018. Evaluations of NDI, VAS (neck and arm pain), SF-12/36 (PCS & MCS), Odom's criteria and patient satisfaction were performed at preoperative (≤ 30 days prior to surgery), 6-week, 3-month, 6-month, 1-year and 2-year points. Radiographic evaluations were also performed to investigate ROM, center of rotation, disc angle, disc height, device condition, device subsidence, device migration, ASD and HO. At the 24-month point, this study had produced multiple findings. Total ASD incidents, which required subsequent surgical intervention, were 3.1% for M6-C and 2.1% for ACDF. Overall HO (Grade 1 to 4) incidents were 59.3%, among which, severe HO (Grade 3 & 4) were 11.4% for the M6-C group while fusion was observed in 78.6% of the ACDF patients. In quantifying the improvements in ROM between the M6-C and ACDF group, comparisons were made on the measurements at pre-op and at month 24. The mean flexion to extension rotation for the M6-C group was 8.33º (pre-op) and 8.78º (month-24) and for ACDF were 8.02º and 1.16º respectively. The mean flexion to extension translation for M6-C was 0.83 and 0.82 mm and for ACDF were 0.87 and 0.13 mm respectively. The mean disc angle for the M6-C group was 2.21º and 7.21º and for the ACDF group was 1.96º and 5.87º respectively. The mean disc height for M6-C group was 3.22 and 5.31 mm and for ACDF group 3.32 and 4.27 mm respectively. The mean lateral rotation for the M6-C group was 5.78º and 6.88º and for ACDF group was 5.77º and 1.34º respectively. The ROM analysis had shown M6-C patients had improved the pre-operation condition and maintained the physiological movements required throughout the 24-months study but decreased in the ACDF group. The study had concluded that the overall success rate for the M6-C subjects (86.8%) was non-inferior to the ACDF subjects (79.3%).

Carl Lauryseen et al[43] had conducted a 2-years investigational study on 1-level and 2-levels treatments following FDA approval (IDE#G050254/S003) on March 12, 2008. The study was conducted on 3 sites in US with total 28 patients (12 1-level, 16 2-levels). The majority of treatments were at C5-C6 (56.2%) and C6-C7 (29.2%). The evaluation

protocol was similar to the main IDE study above. It had found that the M6-C implant had provided a significant improvement on the anterior disc height (pre-op 4.2 mm, month-24 7.0 mm), which might lead to the improvement of the mean disc angle (pre-op 2.8º, at month-24 6.5º). The compressibility of the device was associated with significant improvements of clinical scores. If the device was positioned within 1 mm of the disc midline, then the center of rotation would match that of the intact spine. Generally, there were no significant differences between the two groups over the improvements on clinical scores except in the neck pain VAS score where the 2-level patients had shown significant improvements. The overall success rate was similar between the two groups (83.3% 1-level, 93.3% 2-level).

V.A. Byval'tsev et al[14] had conducted a 3 years study on 112 patients with single level treatments in Russia (date unknown, prior to 2017). Comparing the pre-op and at month 36, patients had significant improvements over clinical scores (VAS, NDI) and mean segmental ROM (6.4±2.5º pre-op, 8.8±2.6º month 36). Only initial (Grade 1) and moderate (Grade 2) HO was detected in 15.1% and 10.7% patients respectively. ASD was detected in 2.8% cases.

Discussion

M6-C represents a more advanced prosthesis design capable in providing 6 degrees of freedom with progressive resistivities. This should mimic the biomechanical behavior of natural IVD. Unfortunately, due to its short history, its long-term effects are unknown. In short term ($\leq$ 3 years), it had shown to provide improvements over clinical scores and patients with better ROM. The only concern is on HO & ASD. Even at 2-year and 3-year point, HO was detected with an unneglectable number in the Grade 3 & 4 level. It seems it is not enough just to mimic the biomechanical properties of the intact IVD. The smaller footprint that does not covering the entire IVD endplates may be an important factor to consider.

2.3 PRESTIGE Cervical Disc System (Prestige-ST)

Owner: Medtronic Sofamor Danek, Memphis, TN, USA

FDA approval: Case P060018, July 16, 2007, single level

Construction[44,45]:

Figure 2-3: The Prestige-ST cervical disc*

Figure illustrates the construction of the device showing its ball-and-trough

structure and the anterior anchoring screws for the fixation of the device.

* Reprint from https://musculoskeletalkey.com/wp-

content/uploads/2016/07/B9781416067269000432_f043-001-9781416067269.jpg taken on May 18,

2021 with permission.

It consists of two surgical grade stainless steel (316) components forming a ball (top) and

trough (bottom) articulating structure. The flat potion of each piece in contact with the

vertebral endplate is grit blasted with aluminum oxide. Each piece has an anterior flange

and affixed to the vertebral body with 2 bone screws, which are locked in position with a

lock screw. The bone screws are put in a divergent position in the cephalic/caudal

direction but in a convergent position in the medial/lateral direction.

It comes in 10 disc-heights x depth configurations. The available disc heights are 6, 7 and

8 mm. The available depths are 12, 14, 16 and 18 mm but not all combinations exist.

ROM[45]:

- Flexion/Extension: $\pm 10^{o}$

- Lateral Bending: $\pm 10^{o}$

- Rotation: unconstrained

- Anterior/posterior translation: 2 mm

Mechanical properties[45]:

- Axial compression: ≥74N (@0.1mm/s, the mean load for 8mm x 12mm specimen was 1343N at 2mm and 6279N at 5mm displacement)

- Compressive fatigue load: ≥74N and ≥10 million cycles (without failure to 10 million cycles under 225N axial load and 10 Hz sinusoidal load with an R values of 10)

- Subluxation shear force (force required to dislocate the upper from the lower component when the device is at different extreme angle of flexion, extension and lateral bending): ≥20N (±shear force applied to the lower component @ 0.1mm/s when device was at neutral, 10° lateral bending and 10° flexion position)

- Push-out force in absent of screws: ≥20N (axial load applied at the posterior portion @ 25mm/min until 10mm was reached, mean force measured is 129N)

- Pull-out force with screw fixations: ≥20N (pull force applied on the anterior edge @ 25mm/min, for the 8mm x 12 mm specimen, the top portion measured was 200N and bottom portion was 251N)

Clinical studies:

Sponsor had performed a 2-years 32 sites investigational study[45,46] (IDE#G010188) in US for its FDA approval application. A total of 421 patients (223 Prestige-ST, 198 ACDF) were treated to a single level (October 2002 to August 2004) and completed the 2-years follow up evaluation. The majority of the treated IVD levels were C5-C6 (51.4% Prestige-ST, 56.2% ACDF) and C6-C7 (40.9% Prestige-ST, 34.3% ACDF). Evaluations of NDI, neck and arm pain, SF-36 (PCS & MCS), sergeant's perception and patient satisfaction were performed at preoperative (within 6 months of surgery), 6-week, 3-month, 6-month, 1-year and 2-year points. Radiographic outcomes (only for smaller

subgroups) were used for elevating segmental ROM at treated and adjacent levels. For a subgroup of 116 Prestige-ST patients, the mean angular motion was 7.55° pre-op vs 7.87° @ month 24, the mean translational motion was 0.26 mm pre-op vs 0.28 mm @ month 24 and the mean lateral bending was ND pre-op vs 6.39° @ month 24. 73.3% passed the angular motion test (>4° to ≤ 20°) and 26.7% failed at month 24. On a subgroup of 123 Prestige-ST patients, 99.2% patients had no bridging bone observed with 0.8% failure. For second surgeries to treat ASD, 3 (1.1%) patients were treated in the Prestige-ST group while 9 (3.4%) patients in the ACDF group.

Praveen V Mummaneni et al[47] had continued with the 2-year IDE study and reported the 3-year's and 5-year's results. Total patients completing the 3-year and 5-year follow-up evaluations were 347 and 111 respectively (didn't specify the number in each of the Prestige-ST group and ACDF group). It had found the 3rd-year NDI score of the Prestige-ST group had significant improvement over the ACDF group but remained same in the 5th-year. No significant was found in the SF-36 and VAS score between the two groups. The Prestige-ST group had maintained a mean 7.1° in flexion and extension throughout. HO and ASD were not reported.

J. Kenneth Burkus et al[12] had completed a 7 years follow up clinical study as a continuation from the initial IDE study above. A total of 395 patients (212 Prestige-ST, 183 ACDF) from the original group had completed the 7 years study. Same clinical scores were continued to evaluate at 36, 60 and 84 months. The clinical score improvements over the 6 weeks were maintained in both groups of patients at the 7 years. The NDI scores of the Prestige-ST group were found significant improvements over the ACDF group. The Prestige-ST group had maintained mean sagittal angular motion of 6.67° and 6.75° at 60 months and 84 months respectively. In addition, bridging bone (HO Grade 4?) was observed to increase from 0.8% (of 250) Prestige-ST patients at 24 months to 6.2% (of 209) at 60 months and 10% (of 201) at 84 months. The study did not cover ASD, however it measured the sagittal angular motion of the superior adjacent segment for both groups and compared to their original values and found that they had roughly maintained their respective values from 6 weeks to 84 months.

<u>Discussion</u>

Prestige-ST has employed a basic design to provide spinal rotations. The center of rotation should be fixed or within a very small range due to its ball-on-trough mechanism. HO (bridging = Grade 4) had increased from 0.8% at 24 months to 10% at year 7. Comparing this with the HO incidents of Bryan disc reported by Gerald M.Y. Quan et al[13], HO had increased from 17.8% at year 1 to 69.2% of Grade 3 & 4 at year 8. Unfortunately, there will be typically higher number of HO patients in Grade 3 than Grade 4. Hence, without knowing the breakdown of the Grade 3 and Grade 4 in the Bryan case, comparison is not possible. With the FDA approval of the Prestige-ST on 2007, longer follow-up results may be available soon.

2.4   Prestige LP Cervical Disc (Prestige-LP)

<u>Owner</u>: Medtronic Sofamor Danek, Memphis, TN, USA

<u>FDA approval</u>: Case P090029, July 24, 2014, single level

<u>Construction</u>[48,49]:
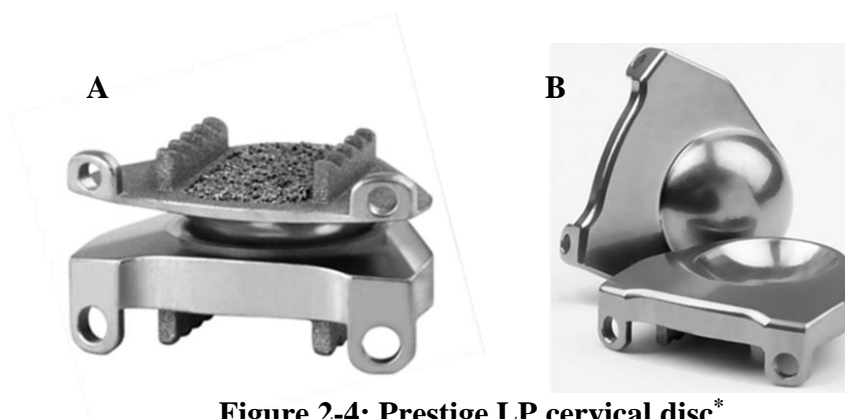
Figure 2-4: Prestige LP cervical disc[*]

Figure A shows the external feature of the device showing its fixation construction. Figure B shows the open view of the ball-and-trough articulating structure of the device.

* Reprint from article[19] with permission from *J Neurosurg Spine*.

The device consists of two plates made from a titanium ceramic composite (Ti6Al4V with 10% Titanium Carbide) forming a ball (upper plate) -and-trough (lower plate) articulating structure to provide rotational freedom. The top of the upper plate and the bottom of the lower plate both have two rails with teeth structures built-in intended to be pressed fit into two pre-drilled holes in the adjacent vertebral bodies to prevent device migration. The rail structures and areas in-between are plasma thermal spray-coated with commercially pure titanium to encourage bony in-growth from the vertebral endplates. The rest of the surfaces in contact with the vertebrae bodies are titanium ceramic roughened to enhance fixation. The two plates are further secured onto the adjacent vertebral bodies via 4 anterior screws.

The device comes in 10 disc-heights x depth configurations. The available disc heights are 6, 7 and 8 mm. The available depths are 12, 14, 16 and 18 mm but not all combinations exist.

Characteristics[49]:

- Shear forces required (applied to the inferior component) to dislocate the ball from the trough feature in any direction and lordotic angulations: $\geq$ 20N (tested mean max horizontal shear force was 357N)
- Axial compressive force without sinking device into the vertebral body endplates: $\geq$ 74N (tested mean ultimate load was 513N with a stiffness of 442 N/mm)
- Push-Out force applied in the anterior/posterior direction @ 3mm/min with a preload of 100N: $\geq$ 20N (tested mean ultimate load was 127.4N for the 6mm x 12mm device)
- Max static axial compression load applied @ 3mm/min: $\geq$ 74N (tested mean failure load was 8808N for the 7mm x 18mm device)
- Compressive fatigue: $\geq$ 5M cycles (tested on two 7mm x 18mm devices and found no failure to 10M cyclic loads of 225N with R value of 10, frequency not specified but should be in the range of 0.1 to 8Hz[50])

- Compressive-shear load (compression applied at 45° to normal[50]): $\geq$ 550N (tested mean max 4962N with a mean stiffness of 6058N)

- Compressive-shear fatigue: $\geq$ 10M cycles (tested on two 5mm x 12 mm devices with same condition as the compressive fatigue test).

Clinical studies:

Sponsor had performed a 2-years 20 sites investigational study[49] (IDE#G040086) in US for the device's FDA approval application. A total of 262 patients were treated with the device between January 13, 2005 to November 8, 2005 and the data collected till April 22, 2009. A total of 201 ACDF patients were taken from the previous Prestige-ST IDE study (IDE#G010188) and used as the control group for this study. The majority of the treated IVD levels were C5-C6 (52.5% Prestige-LD, 56.2% ACDF) and C6-C7 (38.6% Prestige-LD, 34.3% ACDF). Evaluation procedures were the same as in the Prestige-ST case [Section 2.3]. Radiographs were used to evaluate conditions of HO, angular ROM in flexion/extension, ROM in lateral bending, translation, angular ROM of adjacent discs (instead of ASD) and disc height. All clinical scores had shown comparable to superior results in comparison with the ACDF control group. HO of Grade 4 (bridging) was found to progress gradually from 0% at 6 weeks to 5.9% of patients at 24 months in the investigational group. The mean angular ROMs of the investigation group (control group) were 5.67° (7.87°) preoperative, 6.88° (0.53°) at 6 weeks and 6.15° (0.35°) at 24 months. The lateral bending ROMs were N/A (N/A), 6.25° (N/A) and 6.15° (N/A) respectively. The translation ROMs were N/A (0.26mm), 0.90mm (0.16mm), 1.03mm (0.15mm) respectively. This showed an improved ROM for the investigational group over the control group. There was a clear majority of 68.6% investigational group patients had angular ROM >4° and ≤20° at 24 months, among which 67.8% had no grade 4 HO. There were 30.7% patients had angular ROM ≤ 4°, among which a majority of 25.3% had no grade 4 HO. Hence, HO grade 4 was not the major factor in limiting angular ROM. The disc height was found to remain roughly the same values during the whole postoperative period for both groups.

T. Wu et al.[51] had performed a 24 months clinical trial on patients with non-contiguous 2-level cervical degenerative disc disease in China. The intermediate segments (IS) were normal in these cases. A total of 25 patients were treated with Prestige-LP from January 2008 to July 2015. The combined treated levels and the number of treated patients were C3-C4/C5-C6 in 18 cases, C4-C5/C6-C7 in 5 cases, C3-C4/C6-C7(skipped 2 levels) in 1 case and C2-C3/C4-C5 in 1 case. Clinical scores of SF-36 (MCS & PCS), VAS, JOA and NDI and radiographs (CT & MRI) were accessed preoperatively and post-operatively at intervals of 1 week, 3, 4, 6, 12 and 24 months. All clinical scores had significant improvements at the 24 months point over the preoperative scores. Radiographs were used for evaluating cervical lordosis(+)/kyphosis(-) (CL), ROM of cervical spine, ROM of Functional Spine Unit (FSU), disc height (DH) and HO. CL and different ROMs were measured using the Cobb's angle between different planes of the cervical spine (for measurement details please refer to the paper). It was found that the CL was maintained in all patients with no significant differences between preoperative (9.01°) and postoperative (9.86°) conditions. The mean ROM of the IS had improved at the 3 months point (14.54°) over the pre-operation (12.52°) but return back to the pre-op condition at the 24 months point (12.91°). The mean DH of the upper and lower operated levels had both remained roughly the same value throughout the 24 months postoperative period. At the 24 months point, 1 patient (4%) had developed Grade 2 HO.

Guangzhou Li et al[52] had performed a 48-months retroactive study on the correlation between preoperative and postoperative HO developed at the treated levels. 69 patients (total 89 treated levels) were selected having 1 to 3 contiguous levels treated with Prestige-LP between January 2008 to June 2012. All patients had pre- and minimum 48 months postoperative follow-up data. There were 50 patients had one level treatment, 18 had 2-levels and 1 had 3-levels. For the treated levels, 1was at C3-C4, 14 at C4-C5, 58 at C5-C6 and 16 at C6-C7. For the preoperative condition, the study used MRI and CT radiographs and classification methods devised by Miyazaki et al[53] and Kellgren-Lawrence respectively. For postoperative HO, it used 3D reconstructions of the vertebrae involved from CT scans and the McAfee classification system to evaluate the degree of HO. This study had found the incidences of postoperative HO had progress from 17.4% at 12 months, to 21.6% at 24 months and to 37.7% at 48 months. At 48 months there

were 15.7% at Grade 3 or 4. Comparing with the pre- and postoperative condition, it found no significant correlation between them. However, segments with sever preoperative degeneration might develop higher incidences of postoperative HO. It had suggested that HO development might be a continuous degenerative process irrespective of the CDA treatment.

Xu Hu et al[54] had performed a 5 years study on the change of center of rotation (COR) and ROM for a single level treatment using Prestige-LP. For an IVD prosthesis, replicating the inherent COR is considered as an important factor in restoring the quality of motion[31]. 42 patients were treated between January 2008 and July 2013. Cervical radiographs (lateral statistic and dynamic) were taken preoperatively and postoperatively at 3, 6, 12, 24, 36 and 60 months. Basing on the radiographs, flexion-extension ROM, COR, disc height, FSU angles were measured (please refer to the paper for measurement details). It found the mean disc height remained unchanged for all postoperative months. The mean ROM had improved immediately from preoperative 7.5º to postoperative 10.1º but decreased gradually and stablised at 7.8º at 60 months. The mean COR-x (+x points from posterior to anterior direction) had remained unchanged throughout the postoperative period. The mean COR-y (+y points from caudal to cranial direction) had a significant gradual increasing cranial shift in postoperative period (-16.3% pre, 12,7% at 1 year, 15.4% at 3 years and 19.2% at 5 years). (The study did not explain the percentage that the COR results were based on.)

Junfeng Zeng et al[55] had performed a 6-year follow-up study of the Prestige-LP treated at 1 or 2 consecutive levels in China. 61 patients (total 77 implants) were treated between January 2008 to July 2011 with 73.8% at one level and 26.2% at two consecutive levels. The majority of the IVDs treated were 50.6% at C5-C6 and 31.2% at C6-C7. Clinical (VAS, NDI and JOA scores) and radiographs (anteroposterior, lateral and dynamic lateral) data were collected preoperatively and postoperatively at 1 week, 3, 6, 12, 24 months and biennially up to minimum of 72 months. Radiographs were used in evaluating ROM of index and adjacent levels as well as degree of HO (McAfee). ASD was detected as enlarged ossification of the anterior longitudinal ligament, narrowing of the disc space > 30% or anterior enlarged osteophyte formation. The clinical scores were

found essentially stabilized throughout the postoperative period. The mean ROM for the index, superior and inferior levels were also roughly stabilized throughout the postoperative period. There was a progressive HO development. At the 2 years point there were 10.4% (7.8% Grade 3, 2.6% Grade 4) incidences of sever HO and at the final follow-up, there were 23.4% (13% Grade 3, 10.4% Grade 4). Since the clinical scores remains stable, it suggested that the incidences of sever HO did not affect the clinical score. ASD was detected in 29.5% of the patients at the final follow-up, however only 6.6% were symptomatic. With such a low symptomatic ASD level and sever HO didn't affect the clinical outcome, it concluded that the Prestige-LP was an effective CDA device.

Matthew F. Gornet et al[19] had conducted a 10 years FDA-approved IDE (NCT00667459) post-approval study of a single level treatment with the Prestige-LP. Study protocols were the same as in the approval application IDE study by the sponsor. Patients (CDA & ACDF group) from the original study were followed-up to 10 years. Results were compiled at 2, 5, 7 and 10 years. The number of CDA/ACDF patients at each follow-up points were 280/263, 277/260, 277/260, 274/(no ACDF group at 10 years point) respectively. All mean clinical scores (NDI (neck pain & success), Arm pain & success, SF-36(PCS, MCS)) for both the CDA and ACDF group had shown improvements over preoperative conditions and remained stable from 2 years to 10 years point. The CDA group had shown consistently better scores than the ACDF group. The mean angular ROM at the index level for the CDA group measured 6.88º at 6-week point, increase by 1º at the 1-year point and gradually returned back to 6.85º at the 10-year point. The same ROM for ACDF group at the index level was almost immobile (~0.5º) over the entire postoperative period. This study evaluated ASD using the mean angular ROM of the superior and inferior adjacent levels and found both groups increased on average without creating hypermobility and maintained overtime. The incidents of severe (Grade 3 & 4) HO increased almost threefold over time. The total incidents of severe HO detected at the 2-year, 7-year and 10-year point were 10% (8.8% Grade 3, 1.2% Grade 4), 20.5% (15.9% Grade 3, 4.6% Grade 4) and 28.5% (19.5% Grade 3, 9% Grade 4) respectively. However, the severe HO apparently did not impact on patient-reported outcomes. It concluded that the Prestige-LP with results stabled over 10 years was as an effective treatment as ACDF.

<u>Discussion</u>

Prestige-LP uses a similar construction as its predecessor, Prestige-ST, but with a harder material (titanium carbide vs stainless steel 316). With such hard articular surfaces, it is inconceivable to have any postoperative changes in its disc height, angular ROM and center of rotation (COR) throughout the patient's life. The first two points are validated by all clinical studies of this device. For the COR, the Xu Hu et al[54] study had found COR-y had a cranial movement over time. Judging from the small differences (~6.5%) between the results of the first and fifth year and the small patient size, the small upward trend may be just caused by statistical noises. However, this is the only study found on the COR for this device, it will need further studies to validate their discovery. The development of ASD is difficult to compare between different clinical studies because each had its own definition. The incidents of severe HO definitely increase over time. It increases from 10% at 2-year point to 2.9 times at the 10 years point. Comparing this with the Bryan disc from 17.8% at year 1 to 3.9 times at year 8. It seems it has a lower initial postoperative incident of severe HO and a lower long-term incident than the Bryan disc. Comparing with its predecessor, the Prestige-ST, the Grade 4 HO of the Prestige-LP was 1.2% at year 2 and increased by 7.2 times at year 10, while the Grade 4 HO of the Prestige-ST was 0.8% at year 2 and increased by 12.5 times at year 7. The Prestige-LP has comparable initial postoperative Grade 4 HO incidents but lower long-term incidents.

2.5 Cervical Prosthesis – Elastic Spine PAD (CP-ESP)

<u>Owner</u>: Spine Innovations (France) (formerly FH Ortho)

<u>CE Mark</u>[16]: 2012

<u>Construction</u>[16,56,57]:
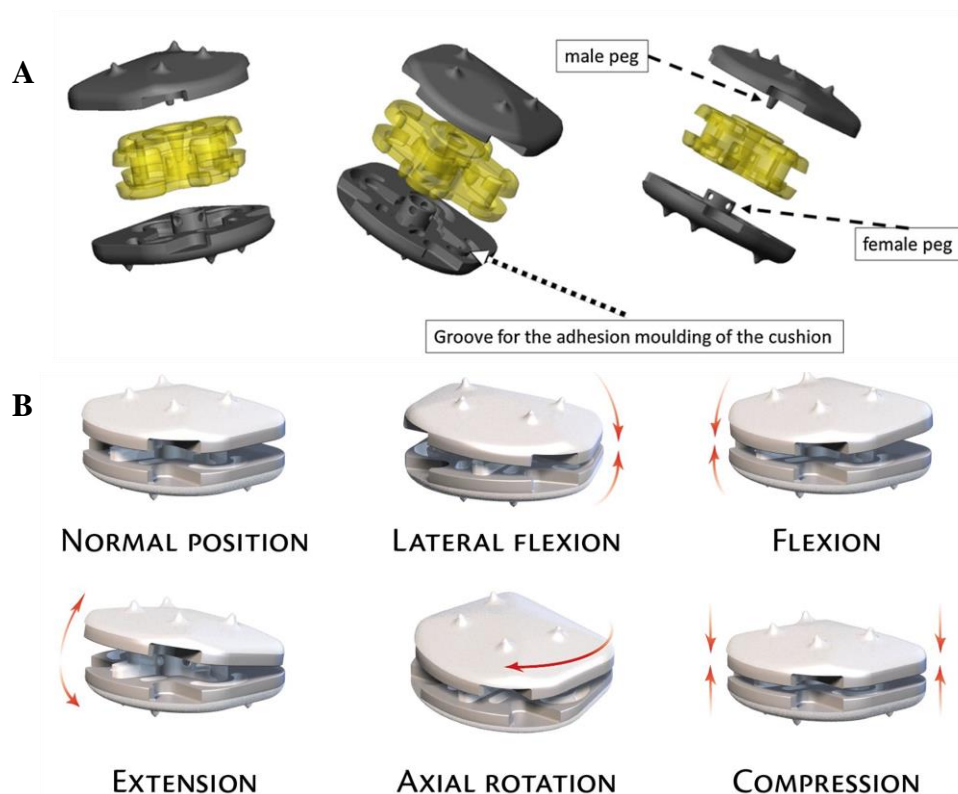
Figure 2-5: CP-ESP cervical disc*

A: shows the construction of the device having two end-plates and a special shaped PCU core. The male and female pegs on the endplates are for limiting the movement of the PCU core within range.

B: shows the 6 DOF mobility of the device.

*A: Reprint from article[16] with permission from *Eur J Orthop Surg Traumatol*.

*B: Reprint taken on May 27, 2021 from https://www.esp-disc.com/wp-content/uploads/2020/11/Cervical-motion.jpg with permission from Spine Innovations, France.

The CP-ESP is a viscoelastic deformable device designed to have 6 full degrees of freedom with shock absorption capability and adaptive instantaneous center of rotation (COR can change freely during motion). It provides elastic resistive and restoring properties for translation, compression and rotational motions.

It consists of two titanium alloy (TiAl4V) endplates sandwiching a one-piece polycarbonate-urethane (PCU, Bionate^{TM} 80A) core. The exterior surfaces of the two endplates have anchoring pegs to provide fixation and are coated with plasma sprayed

pure titanium (T40) and hydroxyapatite (HAP) to promote vertebra bone cell adhesion. The inner surfaces of the endplates also have a pair of male and female peg, together with the geometry of the PCU core, help to limit the degree of compression, rotation and translation to provide spinal stability. The PCU core is shaped in such a way to provide the optimal mobility and control of translation and shear movements. It is "bonded to the endplates via adhesion molding using a peripheral groove without using glue for reinforcement"[16].

It comes in 3 sizes (13x15, 14x17, 15x20 mm) and each with 3 heights (5, 6, 7 mm) making a total of 9 combinations for CDA treatments.

ROM[56]:

- Flexion / extension: ±7° (natural IVD ±7°)

- Lateral flexion: ±5° (natural IVD ±6°)

- Axial rotation: ±3.5° (natural IVD ±4°)

- Anterior-posterior translation: 0.8 mm[16]

Mechanical properties[16]:

- Compressive stiffness: 733 N/mm (natural IVD 492 N/mm)

- Torsional stiffness for extension: 0.03 Nm/1° (natural IVD 0.5 Nm/1°)

- Torsional stiffness for flexion: 0.03 Nm/1° (natural IVD 0.03 Nm/1°)

- Torsional stiffness for lateral bending: 0.05 Nm/1° (natural IVD 0.9 Nm/1°)

- Torsional stiffness for axial rotation: 0.24 Nm/1° (natural IVD 0.8 Nm/1°)

Clinical studies:

J. Y. Lazennec et al[16] had performed a preliminary 2 years follow-up study on 62 patients with single (53 patients) and 2 levels (9 patients) treatments totaling 71 implants. The

majority of the single level treatments were at C5-C6 (42% of total 62 patients) and C6-C7 (32%) and for 2 levels were at C4-C6/C5-C6 (3%) and C5-C6/C6-C7(10%). Clinical scores (Neck and Arm VAS, NDI, SF-36 PCS & MCS) and X-rays were collected at pre-op, 3, 6, 12 and 24 months. From the lateral X-rays, it measured the mean angular ROM at the index, upper adjacent and lower adjacent levels at the 3-, 6-, 12- and 24-months points. The mean ROM of the index level were 6.8°, 10.3°, 8.4° and 10.7° respectively. For that of the upper adjacent level were 9.7°, 11.7°, 12.9° and 13.8° respectively and that of the lower adjacent level were 6°, 10°, 9.4° and 11.1° respectively. It seemed the mean ROM for all levels had stabilized or improved slightly on month 6 and onwards. The paper also displayed the mean COR images of the 3 IVD levels for one patient with global cervical kyphosis and with a single level treatment on the extension/flexion motion from the pre-op to 24 months. Unfortunately, it did not provide any quantitative data or analysis to relate any good results with the capabilities of the device. No incidents of HO were observed.

J. Y. Lazennec et al[58] had performed another 2 years follow-up study on 89 patients treated with one (72 patients), two (16) and three-levels (1) between October 2012 to December 2015. They published a brief summary of their preliminary results in a proceeding supplement. It contained the clinical scores (VAS neck & arm, NDI, SF-36 PCS & MCS) obtained at pre-op, 3, 6, 12 and 24 months. It stated that they "did not observe local ossifications" but had revised "one C5-C6 implant for bone ingrowth failure at 6 months". The ROM had stabilized from 6 month onwards and by monitoring the location of mean COR at the index and adjacent levels "had demonstrated the adaptation ability of the implant". Unfortunately, the paper contained no further information to substantiate these statements.

Discussion

The CP-ESP is an advance CDA device that has capabilities and mechanical behaviors to mimic that of a natural IVD. However, even though it states that it is viscoelastic, no rate depending data is found in the literature. By just relying on its PCU core material properties, it is not known how tunable its IVD mimicking properties can be to match that

of a natural IVD. No HO observed (questionable) for the first two years may be a good indicator in compare with other devices. Unfortunately, with its short history and no follow-up studies beyond 2 years, its long-term benefits cannot be validated at the current time.

2.6   Experimental devices

Many experimental or research-oriented devices have been developed in the past. While most of them were only for research purpose but some even have performed some form of IDE clinical studies. However, their official approval status is not clear. The ones that are included here are those that have their concepts, designs or materials used relevant to this research but not necessary only for cervical disc applications. Unfortunately, most of them have only limited literature available to illustrate their full clinical relevance, mechanical properties, construction and materials. Hence their correctness cannot be thoroughly checked.

2.6.1   PHEMA/PMMA hydrogel composite IVD prosthesis from Antonio Gloria et al

Antonio Gloria et al[59] had developed a device with swollen fiber-reinforced composite hydrogels to mimic the structure of a natural IVD. They wound polyethylene terephthalate (PET) fibers helically on a mandrel (with diameter comparable to that of the NP) at an angle varied between 45 to 65° to mimic the structure of the AF of an IVD and molded the fibers within the poly (2-hydroxyethyl methacrylate)/polymethyl methacrylate (PHEMA/PMMA) 80/20 w/w chemically cross-linked hydrogel. Hydroxyapatite (30% w/w) reinforcing hydrogel was added as endplates material.

They had tested the compressive properties of this device at strain-rates of 1, 5 and 10 mm/min and found no yield up to a load level of 17kN. The J-shaped test stress-strain curves obtained had a toe region up to 0.09 strain followed by a linear region. The Young's moduli of the linear regions were 84 ± 9.8 MPa, 102 ± 11 MPa and 120 ± 12 MPa respectively for the three strain-rates. They had also performed compressive creep

tests on the device using an initial stress of 2 MPa and monitored the strain over 4500s. The mean strain values obtained varied from initial 0.069 to final 0.12 after 4500s, which were comparable to canine IVDs under same test conditions. The creep curves and the compressive stress-strain curves at different strain-rates had validated the device was viscoelastic. No torsional tests were performed.
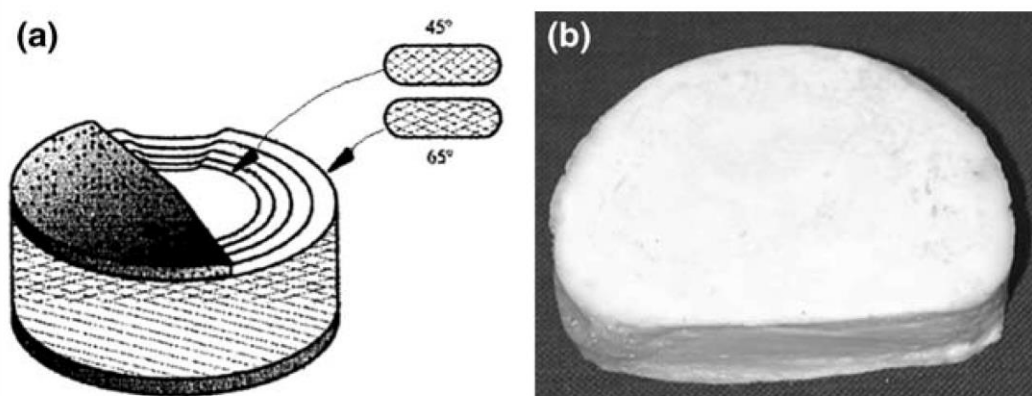
Figure 2-6: An experimental device made from PHEMA/PMMA hydrogel composite[*]

A: a schematic view of the device showing the helical winding angles of the PET fibers core sandwiched in between the hydroxyapatite reinforced endplates.

B: shows a test specimen of the device.

[*] Reprint from article[59] with permission from *J Mater Sci Mater Med* (Springer Nature license # 5075991423083)

Discussions

This device, even though using different materials, had employed a very similar construction concept as the one proposed in this PhD research. From the no-yield compressive load and the Young's moduli of the three stress-strain curves, this is a much stronger device in comparison with the findings from other researchers. Haisheng Yang et al[60] had measured the mean effective Young's modulus of human IVD from T8 to L5 to be 17.0 ± 9.8 MPa @ 0.05%/s and 25.5 ± 8.6 MPa @ 20%/s. From the derivation of the measurements reported by Manobar M. Panjabi et al[61] on human IVD C2 to T1, the Youngs's modulus was around 14.5 MPa [Section 3.5.1]. Both were much lower than the device. The device may be too strong for the CDA application. Unfortunately, the paper

did not provide a method on how to modify the strength of this device to suit the CDA application.

Judging from the low slope of its creep curve and the closeness of its stress-strain curves of the 3 strain-rates, the device is only slightly viscoelastic.

2.6.2   PHEMA/HEMA hydrogel composite IVD prosthesis from Antonio Gloria et al

Antonio Gloria et al[62] had developed another similar device as their PHEMA/PMMA device. In this device, instead of PMMA, it used 2-hydroxyethyl methacrylate (HEMA) instead. The winding arrangement of the PET fibers remained unchanged. The endplate material used became hydroxyapatite-reinforced polyethylene composite (HAPEX^{TM}). Anchoring pegs were added to the exterior surfaces of the two endplates to aid fixation of the device. The kidney shaped geometry (core & endplates) of the device was derived from an average of five porcine lumbar discs. They had performed compressive tests at a rate of 1 mm/min until yield, compressive shear test (device positioned at 45° to horizontal) with preload up to 20N at compressive rate of 1 mm/min up to 600N and torsional tests with a compressive load of 500N at torsional rate of 0.1^o/s up to a maximum of 1 Nm torque. The mean compressive curve obtained was non-linear. Initially it had a toe region, followed by a linear region, then a decrease of the slope and then followed by an increase of slope before reaching the maximum load. The compressive stiffness at the linear region was measured at 4.03 kN/mm. The nonlinearity above 5.8kN as explained was due to the failure of the HAPEX^{TM} at the outer contour of the endplate. The compressive-shear curve was more linear with a small initial toe region. The compressive-shear stiffness was found to be 205 ± 22 N/mm. The torsional curve obtained had a steep initial rise from 0 to ~1/3° and followed by a plateau with a small rising slop until failure at round 3.5^o rotation. The plateau might signify plastic deformations. The torsional stiffness found was 2.8 ± 0.3 Nm/deg.

Discussions

The compressive stiffness of this device was found to be 4.03 kN/mm. Same property of those prostheses with metal-on-metal structures will be almost infinite. A reasonable

comparison will be with those having PCU cores. The CP-ESP had reported that its compressive stiffness and that of a natural human IVD was 733N/mm and 492 N/mm respectively [Section 2.5]. Basing on this, this PHEMA/HEMA device is much stiffer than a human IVD.

Unfortunately, comparing stiffness is not meaningful because stiffness is dimension dependent. Without knowing its geometric details such as cross-sectional geometry and height, it is difficult to compare its compressive strength with other devices, even with their previous PHEMA/PMMA device. Only comparisons with dimensionally independent material properties (e.g., Young's modulus) between devices will be meaningful.

2.6.3   NeoDisc cervical disc

The NeoDisc[63,64] is a CDA device originally developed by Health Innovation Support (UK) and later sold to NuVasive Inc. (San Diego, California, USA). It consists of a solid silicone elastomer core inserted into a jacket manufactured from polyester suture material using computer-controlled embroidery. It is held in position to the adjacent vertebrae by 4 anterior titanium bone screws. Long-term fixation is expected from fibrous tissue integration with the jacket material.
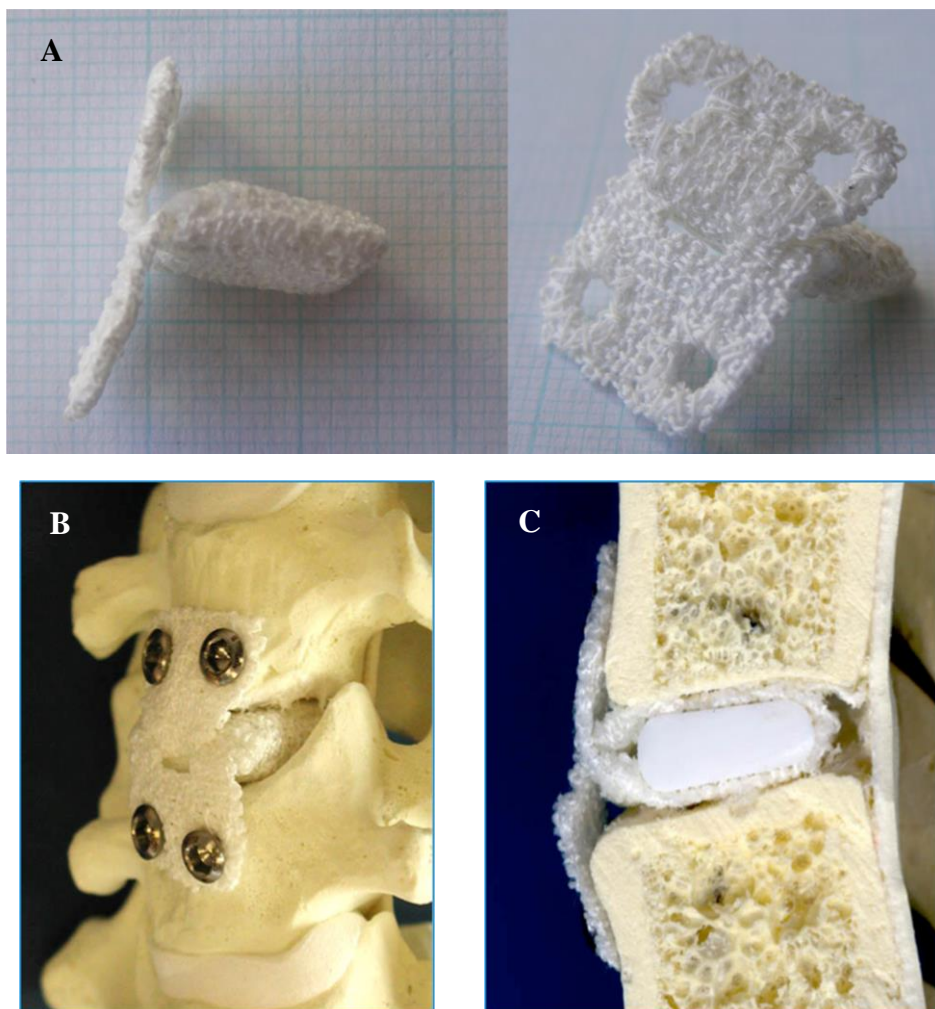
Figure 2-7: The NeoDisc cervical disc*

A: provides the side and front view of the device showing its outer jacket manufactured from polyester suture material using computer-controlled embroidery.

B: shows its fixation method employed using 4 anterior screws.

C: shows a cross-section of the device with its silicone elastomer core.

*Reprint taken on May 25, 2021 from:

A: https://www.healthinnovationsupport.co.uk/wp-content/uploads/2017/04/Neodisc-1.png.

B: https://www.healthinnovationsupport.co.uk/wp-content/uploads/2017/04/Cross-sectional-view-neodisc.png

C: https://www.healthinnovationsupport.co.uk/wp-content/uploads/2017/04/NeoDisc-mounted-on-artificial-neck-bones.png

with permission from Health Innovation Support, UK.

NuVasive had conducted a 2-years IDE (NCT00478088) clinical study[64–66] in US

involving 53 patients (28 NeoDisc, 25 ACDF) who had completed the 2-year follow-up period. The patients were treated at a single level between September 2006 to August 2010 and followed-up to March 2012. Clinical scores (VAS, NDI, patient satisfaction) and flexion/extension radiographs were evaluated on preoperation and at 6 months and 2 years follow-up. The success of the trial was defined as greater than 15 points improvements in NDI. It was achieved in 89.3% of the NeoDisc group patients and 72% in the ACDF group. As for ROM for the NeoDisc group, the pre-operative mean was 10.7º, 8.4º at the 6 months and 8.2º at 2-year follow-up. Unfortunately, for unknown reasons, NuVasive had aborted this IDE study[64] and the device is not yet approved by FDA.

<u>Discussion</u>

The NeoDisc has a non-traditional design and construction. It does not have endplates. The integration of the implant is designed to be via soft tissue ingrowth over its polyester fabric material instead of ossification. With its embroidery construction, the control of its initial translational ROM may be a concern. However, no mechanical test data found to evaluate this yet. Even though the soft tissue integration had been validated via a sheep model, its effectiveness and possibility of inflammatory response to the polyester material might need further investigation[64].

2.7 Discussion

2.7.1 Structure & core material

The CDA devices reviewed in this Chapter may be roughly classified into two classes: hard core and elastomeric core construction. The hard core class of devices is mainly based on the ball-in-trough construction, whose concept might be derived from the Bristol-Cummins disc[67] developed around 1991[68]. This class of devices is mainly constructed with hard materials (e.g., stainless steel) hence it is practically incompressible and has fix COR. It supports the bodily weight, as an ACDF implant does, and provides 3 degree-of-freedom (DOF) in rotational ROMs. This provides the basic function of a CDA device. The two CDA devices reviewed over here, Prestige-ST and Prestige-LP, belong to this class. Other popular devices of this class in the literature include the Mobi-C[69],

ProDisc-C[2] and ProDisc Vivo[5]. The elastomeric core class of devices employs a deformable polymeric material (e.g., PCU or its derivatives) as its core. It supports the bodily weight (axil compression) by slight vertical deformation and 6 DOF of motion by a combination of asymmetric deformations in opposite directions, rotation and shear/compression. Its PCU (or derivative) core generally provides some degree of viscoelasticity. Depending on its construction, there may be elastic restoration reactions. The design intent of this class of devices is to mimic the mechanical properties/behaviors of a natural IVD. The Bryan cervical disc, M6-C, CP-ESP, the two hydrogel composite discs from Antonio Gloria et al and the NeoDisc reviewed in this Chapter belong to this class. A few more examples can be found in the paper from C.A.M. Jacobs et al[64]. This class of devices can adapt to any instantaneous COR in any spinal mobility as a natural IVD, hence provides a better quality of motion.

The mono-block construction of some of the CDA devices (CP-ESP) may lead to a reduced risk of wear problem as compared with those with sliding articulating surfaces. Having a shielding sheath to enclose the entire core (Bryan Cervical & M6-C) does not solve the wear problem but preventing the debris, if produced, from leaking out. Some use extreme hard material (titanium carbide in Prestige-LP) to reduce the amount of debris produced to an acceptable level.

In general, the devices with simple structures (mono-block, ball-in-socket) may have lower chance of failure in long term. Christopher Brenke et al[70] had analyzed the failure case of an original version of a 6-year-old M6-C implant with a herniated core. The surrounding fibers were found ruptured. Apart from intuitive reasoning, the main culprit was difficult to identify after the fact in most cases. A newer version of the M6-C devise with stronger fibers and modified endplate anchoring is now available.

The experimental devices in Section 2.6 and some described in the C.A.M. Jacobs et al[64] paper have either no metallic endplates or totally without endplates. This type of devices may have an advantage over those with mantellic endplates in that they do not produce artefacts in follow-up MRI/CT radiographic images to investigate the status of the implant and spinal movements. Another possible advantage is in better matching of

interfacial material properties between the device and the vertebral bones than hard metallic materials.

2.7.2 Long-term effects

HO and ASD have been identified as long-term effects of many current CDA devices in the literature. In this review, both were evaluated on a per device basis. Cross device comparisons may be confounded by the differences of their design of the device and their postoperative duration. However, a trend is clear. Many of the clinical studies of each device having follow-up histories more than 2 years have shown both the number of patients and their severity of HO have increased in time. Some researchers had attributed the development of HO to predisposed osteoarthritis conditions at the index level. Patients having preoperative ossification history at the index vertebrae may lead to higher chance of postoperative HO. Although this can explain some of the cases, it does not explain the same trend happened in many devices. Judging from the fact that the ossification sites locate mainly on areas not covered by the endplates of the devices, this may lead to a suggestion that a device with end profiles conforming exactly with the adjacent vertebrae surfaces of a patient may reduce the incidents of HO. Hence a patient specific prosthesis may solve the long-term HO development problem.

ASD had been identified in many of the clinical studies. Unfortunately, ASD does not have a uniform definition even between clinical studies of the same device. This makes the comparison of degree of ASD development difficult between different clinical studies, let alone between different devices. Some clinical studies had used a simplified approach by measuring the ROM of the superior and inferior IVD without analyzing their HO status. Some had included both and other conditions. However, same as the HO situation, many clinical studies had identified ASD also tends to increase in number of patients and severity in time. Causes of the development of ASD are not currently identified. It may be hypothesized to be caused by additional stresses exerted onto the adjacent levels induced by the index level prosthesis device due to its spinal motion limitations or mismatched mechanical properties. A device that can fully mimic the material properties, ROM and DOF of an IVD, i.e., functions fully as a natural IVD, may reduce the incidents of ASD development.

While both incidents of HO and ASD had shown increased in time within each of the study groups, it is puzzling to find that some clinical studies had found that they did not affect the mean clinical scores of the group throughout their entire follow-up period, hence concluded that they didn't affect the health condition of the patients. Common sense will point out that a Grade 4 HO condition will turn a CDA device equivalent to an ACDF implant. This leads one to puzzle how effective these common clinical scores and lateral radiographic techniques employed can measure the quality of motion of a patient in real life situation. The quality of motion in the majority of these clinical studies were mainly determined by the simple flexion & extension ROM. May be a more complex ROM derived from motions including combinations of flexion/extension, lateral bending, axial rotation and translation would provide a better measure.

Current methods to quantify the mechanical strengths of an IVD prosthesis device in the industry, as specified in the ASTM standard[50], use compressive stiffness (force per displacement, N/mm) and torsional stiffness (torque per degree of rotation, Nm/$^{\circ}$). Unfortunately, stiffness is device dimension dependent hence not a good property to compare between a device with a human IVD or between devices. A better method will be to use dimensionally independent or normalized properties like stress, strain and modulus. In this research study, all compressive and torsional properties will be quantified in these dimensional independent properties.

In summary, this literatures review section has led to the fact that current IVD prosthesis devices haven't fully mimic the size, shape, material properties and mechanical behaviors (DOF and COR) provided by a natural IVD. The fixation damages to the vertebral bodies may be a cause to trigger their continue remodeling resulting in long term HO. All these mismatches and damages may lead to the long-term development of HO and ASD. Improvements over existing devices may be in two main areas.

The geometry (size and shape) of the prosthesis should be the same as a healthy IVD as the removed IVD of the patient. The device must have the same footprint as the IVD removed, covering the entire end-plate areas (superior and inferior) of the affected

vertebrae and with the height adjusted to treat radiculopathy. This means the prosthesis must be able to be patient-specifically molded/shaped into any shape and size required.

The device should mimic the mechanical properties of a healthy IVD in providing 6 DOF in movement and extend in each direction and variable instantaneous COR. This requires the material to be viscoelastic and has compressive and torsional strengths to match that of a healthy IVD. A single block design may be preferable over a multiple components construction to reduce the risks in component failures.

The above two themes are explored in the current research study.

Chapter 3

3 Viscoelasticity & Impact Resistance Characterization of Kangaroo Cervical Intervertebral Disc

<u>Abstract</u>

The goal of this study is to characterize the large-scale size-independent viscoelastic behavior and impact-resistance of unrestricted bulk material properties of kangaroo cervical C5-C6 intervertebral disc (IVD) under axial compression and torsion. The results should be of interest to researches in IVD prosthesis development and spinal simulation for traumatic events.

The viscoelasticity is characterized by modeling stress (compressive or torsional) as a function of time and strain. In each case, a surface was fitted (least square error with acceptable R^2 value) over experimental data of stress measured under different strain rates until yield (compression n=19 rate=0.25mm/min to 150 mm/s; torsion n=13 rate=1º/min to 90º/s). A polynomial surface of degree 3 in time and degree 1 in strain was found to provide acceptable fit for compression and torsion separately. This shows kangaroo cervical IVDs are linear viscoelastic under both compression and torsion.

A definition was proposed for quantifying the impact resistance of a viscoelastic material. A derivation method was developed basing on the "viscoelastic surfaces" obtained. A series of triangular impulse stress of 70ms duration of different peak stress values was used to illustrate this method for compression and torsion separately.

For compression (n=19), the mean yield stress found was 11 MPa (sd 3.4) and mean yield strain 0.55 (sd 0.2). The Young's modulus ranges from 20.0 MPa (t=0) to 6.7 MPa (t=379 s). For torsion (n=13), the mean yield stress was 13 MPa (sd 5.0) and mean yield strain 0.66 (sd 0.17). The torsional modulus ranges from 20.7 MPa (t=0) to 2.7 MPa (t=347 s). The comparison with human C5-C6 IVD properties, even though likely to be comparable in strength, was inconclusive due to the lack of data in literature for human C5-C6 IVD specimens tested under similar conditions.

3.1   Introduction

An IVD, being sandwiched in between two vertebrae, serves to support the bodily weight, to provide spinal mobility and to provide shock-absorption in the spinal column. Neck injuries, resulting from traumatic incidents such as in automobile collisions, sports and uncontrolled falls, are current research areas. The characterization of the bulk material properties of the cervical IVDs will allow better understanding of neck injuries during these incidents. It will also benefit many fields of spinal research, such as in the development of prosthesis for total disc arthroplasty, in the simulation of the spinal performance using finite element methods (FEM) and in the development of personal protective equipment to prevent neck injuries.

Many spinal researches have focused on the study of the lumbar section of the spine, especially on the range of motion (ROM) in flexion-extension, bending and axil rotation. Large scale viscoelastic behavior studies, especially torsional characterization and in the cervical region, are limited. The ROM determination is important for daily activities. However, in a traumatic situation, the major injury vector[71] will not stop even after the fracture of the ROM limiting structures (e.g. facet joints). To fully study the spinal behavior in a traumatic event, one requires the native material properties as well as yield characteristics of each component of the spine. This study had focused on the material properties of the IVD free from any movement limiting structures (unrestricted).

Even though the importance of torsional behavior of IVD is still under debate due to their limited ROM, some researches had shown that even low torsional motion below the yield limit can damage the IVD[72–74]. Hence characterizing the torsional behavior is important. Most earlier studies[75,76] characterized the torsional behavior by measuring torque vs rotation angle. This approach may limit the generalization of the results due to differences in the IVD size and shape. Some recent studies[72,77] had normalized the results with the polar moment of inertia of the IVD, a similar technique used in the physics of rotating shafts. However, they still fell short in defining a shape independent torsional stress, strain and modulus properties. This study followed the traditional approach used for the compression and shear behavior by defining these properties in such a way that

the area under the torsional stress-strain curve represents the same measure of the energy (work-done) absorbed by the IVD per unit volume. With this approach, the torsional analysis can use the same derivations from the compressive case, i.e., in modeling the viscoelastic and impact resistant properties of the IVD.

Studies had shown that the integrity of the endplates of an IVD is susceptible to short impact durations[78]. Damaged endplates correlate well to subsequent disc degeneration[79]. Impact resistance capacity of a material is traditionally measured using an ASTM drop test method such as the Charpy pendulum or free-falling weight. However, this method will be difficult to apply to IVDs because they are embedded between two vertebrae. Chamis et al[80] had proposed an alternate method making use of the area under the stress-strain curve of a material. This represents the energy (or work-done) absorbed by the material per unit volume induced by the impact force. For a viscoelastic material, the stress-strain behavior is also time dependent. This study extended this method to employ a time average of an impulse force over the stress-strain-time behavior to quantify this property. Effectively it is the mean energy absorbed by the material over the duration of the impact force or torque.

Traditionally viscoelasticity is analyzed by either using a set of creep curves[81], relaxation curves[82] or stress-strain curves at different strain rates. Unfortunately, even though all three methods describe the same material property, deducing results of one from another is not simple. This study introduces a "viscoelastic surface" method to model the stress-strain-time relationship of the material behavior using a polynomial model. The creep, relaxation and stress-strain curve at a given strain rate can be easily deduced from this generalized model. An additional benefit of this method is that the impact resistance of the material, when subject to an impulse force, can be derived mathematically.

The ideal candidate for studying the biomechanical properties of IVD is obviously human. Unfortunately, due to the limited availability and choices of uniform human specimens, animal models, typically quadrupeds[75,82–86], have been widely used in the in vitro spinal research. Due to our upright standing posture, our cervical IVDs are under compression due to the weight of our head. This compressive pattern and magnitude are

different from those of the quadruped animals. This study hypothesized that kangaroos, having similar upright standing posture, similar weight and height to young adult human, will be a good model for IVD studies, especially in the cervical region.

The objective of this study was to characterize the large-scale cranial compressive and torsional viscoelastic properties of the unrestricted C5-C6 cervical IVD using kangaroos as the animal model. In addition, their statistical yield limits and impact resistance capacities in each excitation type were also evaluated. Large-scale viscoelastic behavior of unrestricted kangaroo C5-C6 IVDs were tested under very slow compression rate (0.25mm/min) to very high compression rate (150mm/s) and at rotational speed of 1°/min to 90°/s. Their corresponding yield stress and strain values were also measured. The impact resistances were evaluated using a 70ms triangular impulse of various magnitude. Finally, their size independent material properties were compared with those from human C5-C6 IVD obtained from literature.

3.2   Materials and Method

3.2.1   Sample preparation and IVD Test Unit (ITU) Construction

Sixty freshly frozen kangaroo upper body spines [Figure 3-1] (Macropus rufus and Macropus giganteus, 80-110 lbs body weight without head, unknown age and gender) were procured from Australia (Hills Foods Ltd, BC, Canada). All were microCT-scanned
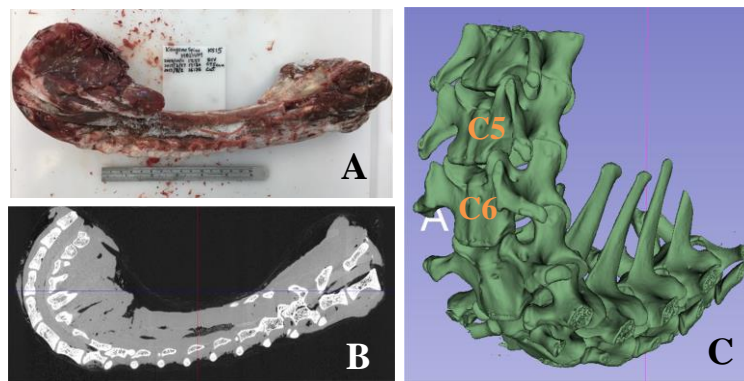
Figure 3-2: Kangaroo spine specimen

(A) is a specimen of kangaroo spine in frozen state. (B) Its CT-scan image.
(C) Its segmented 3D image with C5 & C6 identified.

(GE Locus Ultra, 154μm 3D voxel, 80kV, 50mA) and kept frozen in -20°C. The specimens chosen for testing was the IVD C5-C6 of the cervical spine. Each spine specimen was defrosted (48 hours in 2°C) with C5 to C6 section dissected out, de-fleshed and with posterior and part of lateral structures removed [Figure 3-2] to eliminate
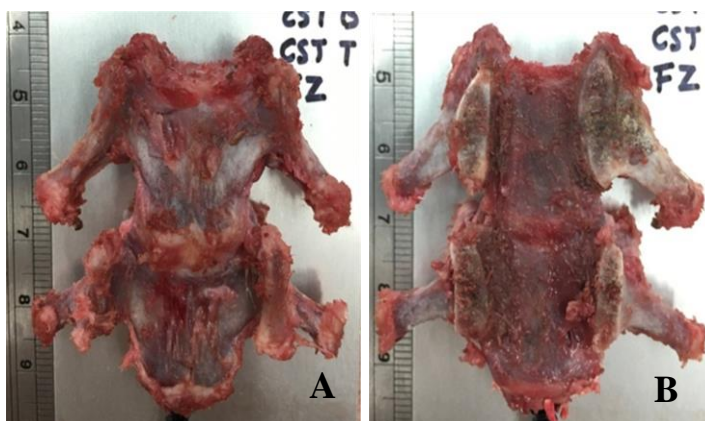
Figure 3-3: Processed C5-C6 IVD test specimen

(B) Anterior view (B) posterior view

obstructions to rotational and compressive movements of the vertebrae bodies.

The resulting specimen was cast into an IVD Test Unit (ITU) [Figure 3-5] in between 2 machine-cut ABS pipe sections (4" ID, 1-3/4" height) with top and bottom embedded (~3/8") into the casting compound (Denstone, Heraeus Kulzer, IN 46614-2517, USA). The center line of C5 & C6 was positioned vertically (C5 on top) and aligned with the center line of the two ABS sections using a jig specially designed for this process [Figure 3-3]. A wet paper towel was wrapped loosely around the exposed middle portion of the ITU to maintain a humid environment around the specimen. Each ITU was placed in a sealed plastic bag and kept frozen horizontally at -20°C before testing. Prior to testing, each specimen was defrosted (48 hrs in 2°C) horizontally and brought back to room temperature (21 °C) for ~4 hours. After testing, the IVD was transected horizontally to inspect the health condition of the IVD to determine the acceptability of its test result.
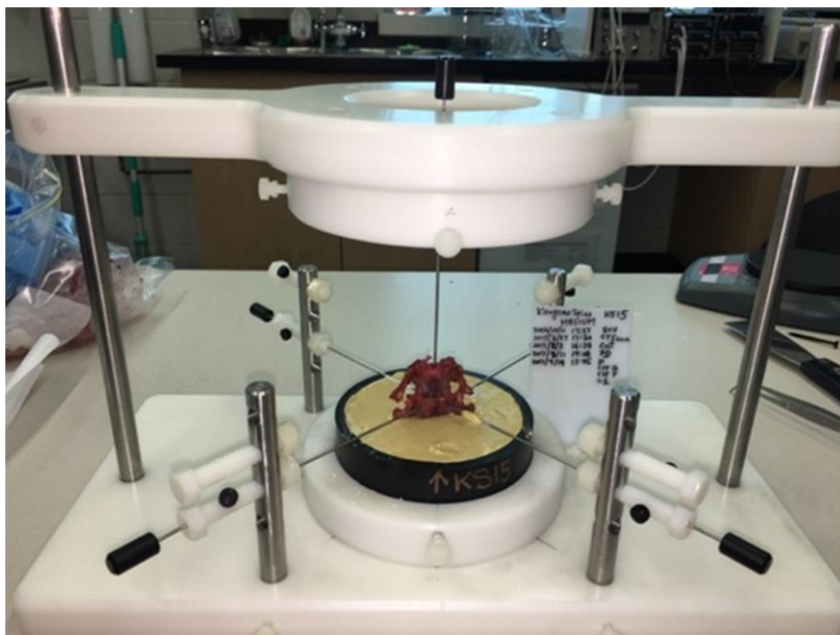
Figure 3-4: ITU casting jig

This jig allows the center line alignment of the IVD specimen, the top and the bottom cast section. The upper portion slides up and down via two vertical rails. Both the top and bottom bracket have 4 mounting screws to house the 4" (ID) ABS pipe section for casting. A removable inner insert can be mounted in the upper bracket to house a center pin to indicate the center of the ABS pipe section. This center pin is used for aligning the center of the IVD specimen when casting the lower half of the ITU. The lower part of the ITU is cast first. After the casting compound solidifies, the lower ITU is removed from the jig's lower bracket and mounted upside down on the upper mounting bracket for casting the top part of the ITU. The whole upper portion slides down with suitable distance to immerse the upper part of the IVD specimen into the casting compound and holds there for the upper ITU to solidify.

Figure 3-6: IVD Test Unit (ITU)

Then C5-C6 IVD specimen is casted with part of the vertebrae body embedded within the casting compound.
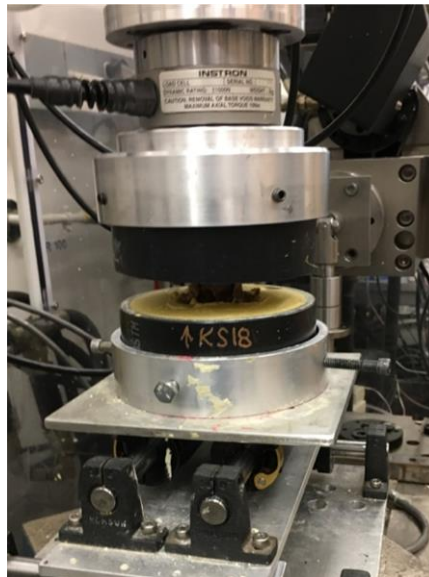
Figure 3-5: ITU mechanical testing setup

The ITU is held in place with special brackets attached to the top load cell and bottom stationary test platform. The top and bottom brackets are center aligned before the attachment of the ITU.

3.2.2   Material testing

Mechanical testing was performed on a bi-axial Instron 8874 machine using a ± 10kN
and 100Nm load cell. Each ITU was mounted onto the load cell with C5 on top via 4
horizontal screws screwed into the ABS section on top and bottom of the ITU [Figure
3-4].

Geometric dimensions of each IVD were determined from its CT-scanned image
(MicroView). The IVD image was rotated in such a way that the Sagittal plane bisected
the spinous process and the Coronal plane touched the outmost point of both C5 at the top
and C6 in the bottom. The IVD image together with the scale on the Sagittal plane was
taken as a screen capture. The disc height was taken as the arithmetic mean of the
posterior, anterior and mid disc height measurements from the Sagittal image (ImageJ)
[Figure 3-7A]. Another screen capture was taken from the IVD image together with the
scale in a Transverse plane close to the cranial portion of C6. The disc area was measured
from the cross-sectional area of the C6 cranial surface (ImageJ).

3.2.2.1   Compressive Viscoelasticity Characterization

Each ITU was subjected to a two stage-pre-conditioning steps before compression
testing. The purpose was to revitalize their original condition in the animal body. The
specimen was compressed to a maximum load of 100 N at a rate of 0.25mm/min. The
ITU was held in position for 15 minutes before the load was removed. After a resting
period of 2 minutes, the specimen was compressed to a load of 50 N at the same rate
(0.25mm/min) with a holding time of 1 minute followed by an oscillating displacement
(sine wave, 0.1Hz, amplitude ±0.05mm) for 15 min. The sample was left to rest for 2
minutes before testing.

A total of 19 ITUs were compressed at constant displacement rates as given in Table 3-1
until they yield. The elastic portion of the stress-strain curve, $\sigma_c(\varepsilon_c)$, and strain-time
curve, $\varepsilon_c(t)$, of each ITU were extracted (MS Excel) and the collective compressive
viscoelastic behavior of the C5-C6 IVDs, $\sigma_c(t, \varepsilon_c)$, was derived as a polynomial surface
using least square error fitting method (Matlab) [Section 3.3].

3.2.2.2   Torsional Viscoelasticity Characterization

Each ITU for the torsional test was subjected to a similar pre-conditioning procedure as in the compressive test case with the except that the second stage was performed by compressing the specimen to a maximum load of 50 N at a rate of 0.25mm/min. The ITU was held in position for 1 minute followed by an oscillating rotation (sine wave, 0.1Hz, angular rotation ±2º) for 15 min. The sample was left to rest for 2 minutes before testing. The positive direction of rotation was defined by the right-hand-screw rule with the thumb pointing upwards.

A total of 13 ITU were tested using constant rotation speeds listed in Table 3-2. Each test was initially rotated to -15º and then rotated in the positive direction until its yield point. Torsional stress (σ_τ) and torsional strain (ε_τ) were derived as defined in Section 3.3.2. The positive elastic portion of the stress-strain curve, $\sigma_\tau (\varepsilon_\tau)$, and strain-time curve, $\varepsilon_\tau (t)$, of each ITU were extracted (MS Excel) and the collective torsional viscoelastic behavior of the C5-C6 IVDs, $\sigma_\tau (t, \varepsilon_\tau)$, was derived as a polynomial surface using least square error fitting method (Matlab) [Section 3.3].

Table 3-1: Compression Rates

Compression rate	Strain rate*	# of specimens
0.25 mm/min	0.09/min	3
0.408 mm/s	0.15/s	3
0.980 mm/s	0.35/s	2
2.315 mm/s	0.84/s	3
4.605 mm/s	1.66/s	3
50 mm/s	18.05/s	3
100 mm/s	36.10/s	1

150 mm/s	54.15/s	1
		N=19

* Based on mean IVD geometry (Table 3-3).

Table 3-2: Rotation Rate

Rotation rate	Strain rate*	# of specimens
1 deg/min	0.03/min	4
23 deg/sec	0.71/s	3
45 deg/sec	1.39/s	3
68 deg/sec	2.09/s	2
90 deg/sec	2.77/s	1
		N=13

*Based on mean IVD geometry (Table 3-3).

3.2.2.3   Impact Resistance

For each compression and torsion test, the impact resistance values were determined using a series of 10 triangular impulses of 70 ms duration with increasing peak stress values from 0 to the mean yield value determined were evaluated according to the method described in Section 3.3.3.2.2 (Matlab). A graph of the impact resistance values (MEAD) vs the peak stresses values were obtained (Excel).

3.3   Data Analysis Method

3.3.1   Generation of the viscoelastic surface

The viscoelastic surface $\sigma(t, \varepsilon)$ can be approximated mathematically by a polynomial $P_{mn}(t, \varepsilon)$, or simply P_{mn}, of degree m in time t and n in strain ε. The coefficients of the polynomial are determined by the least-square-error fitting method giving minimum m and n values with acceptable high R^2 value, e.g., $R^2 \approx 0.9$.

$$\sigma(t,\varepsilon) \cong P_{mn}(t,\varepsilon) = \sum_{i=0}^{m}\sum_{j=0}^{n} p_{ij}\, t^i \varepsilon^j = \left[\begin{pmatrix} p_{mn} & \cdots & p_{0n} \\ \vdots & p_{ij} & \vdots \\ p_{m0} & \cdots & p_{00} \end{pmatrix}\begin{pmatrix} t^m \\ \vdots \\ 1 \end{pmatrix}\right]'\begin{pmatrix} \varepsilon^n \\ \vdots \\ 1 \end{pmatrix}$$

As will be shown in the results and discussion section, we found that, in both the compressive and torsional case, P_{31} provided a satisfactory fit for the experimental data. Hence in this Chapter, all viscoelastic surfaces are in the following form:

Equation 3-1: Viscoelastic surface polynomial P_{31}

$$\sigma(t,\varepsilon) \cong P_{31}(t,\varepsilon) = \left[\begin{pmatrix} p_{31} & p_{21} & p_{11} & p_{01} \\ p_{30} & p_{20} & p_{10} & p_{00} \end{pmatrix}\begin{pmatrix} t^3 \\ t^2 \\ t \\ 1 \end{pmatrix}\right]'\begin{pmatrix} \varepsilon \\ 1 \end{pmatrix}$$

3.3.2   Torsional Stress, Strain and Modulus Definitions

The figure shows a horizontal cross-sectional view of an IVD. Assume the area of an IVD can be approximated by an elliptical shape as shown in the figure.

(For variable definition see Section List of Abbreviations)

Perimeter of IVD $\cong \pi\sqrt{\dfrac{a^2+b^2}{2}}$

For an equivalent circle of radius $\bar{r}$ having the same perimeter:

$$\bar{r} = \frac{1}{2}\sqrt{\frac{(a^2 + b^2)}{2}}$$

The polar moment of inertia of the IVD:

$$J = \frac{\pi ab(a^2 + b^2)}{64} = \frac{A(a^2 + b^2)}{16}$$

Equation 3-2: Torsional stress as defined in this study (unit: Pa)

$$\sigma_\tau \equiv \frac{\tau \bar{r}}{J} = \frac{16\tau \bar{r}}{A(a^2 + b^2)}$$

Equation 3-3: Torsional strain as defined in this study (unit: dimensionless)

$$\varepsilon_\tau \equiv \frac{\bar{r}\theta}{h}$$

Equation 3-4: Torsional modulus (unit: Pa)

$$\Gamma \equiv \frac{d\sigma_\tau}{d\varepsilon_\tau} = \frac{h}{J}\frac{d\tau}{d\theta} = \frac{16h}{A(a^2 + b^2)}\frac{d\tau}{d\theta}$$

Note that the torsional modulus is independent on the equivalent rotational radius $\bar{r}$.

The area under the torsional stress-strain curve will be (unit: joule/m^3):

$$\int_0^{\varepsilon_\tau} \sigma_\tau \, d\varepsilon_\tau = \int_0^\theta \left[\frac{16\tau\bar{r}}{A(a^2 + b^2)} \times \frac{\bar{r}}{h} \right] d\theta = \frac{16\bar{r}^2}{Ah(a^2 + b^2)} \int_0^\theta \tau d\theta = \frac{2}{V} \int_0^\theta \tau d\theta$$

Hence, with the definitions of torsional stress and strain in this study, the area under the torsional stress-strain curve is a measure of the energy (work-done) absorbed by the IVD per unit volume. This is the same case for compression and shear. Because of this, the theory developed for the compression case (e.g., impact resistance) in this study will equally apply to the torsional case.

3.3.3   Impact Resistance

3.3.3.1   Definition of impact resistance for viscoelastic materials

When a material is subjected to an impulse stress wave $\sigma_I(t) = \int_0^T \sigma_I(t)\, dt$ of peak value S and duration T, the impact resistance (or the shock absorption) capacity of the material is defined as the mean energy absorbing capability per unit volume (initial), or the mean energy absorption density (MEAD), of the material on this impulse stress.

In general, the energy absorbed density (EAD) by a material under a stress producing a strain value ε_1 can be derived from the area under the stress-strain curve:

$$EAD = \int_0^{\varepsilon_1} \sigma(\varepsilon)d\epsilon$$

For a viscoelastic material, the stress is also time dependent. The mean energy absorbed density by the viscoelastic material is defined as:

Equation 3-5: Mean energy absorption density

$$MEAD \equiv \frac{1}{T}\int_{\varepsilon=0}^{\varepsilon_1}\left[\int_{t=0}^{t=T}\sigma_I(t,\varepsilon)dt\right]d\varepsilon = \frac{1}{T}\int_{t=0}^{t=T}\int_{\varepsilon=0}^{\varepsilon_1}\sigma_I(t,\varepsilon)d\varepsilon\, dt$$

3.3.3.2   Deriving MEAD

3.3.3.2.1   Solving for $\varepsilon_I(t)$

$\sigma_I(t,\ \varepsilon)$ in Equation 3-5 is the horizontal projection of the impulse stress $\sigma_I(t)$ onto the viscoelastic surface $\sigma(t,\ \varepsilon)$ [Figure 3-6], every point on the $\sigma_I(t,\ \varepsilon)$ surface should satisfy the following constrain:

$\sigma(t,\varepsilon) = \sigma_I(t)$, or

Equation 3-6: Constrain for projected impulse stress onto the viscoelastic surface

$$\sigma(t,\varepsilon) - \sigma_I(t) = 0$$

This is an equation in *t* and ε only. One can solve ε in terms of *t* giving $\varepsilon_I(t)$.
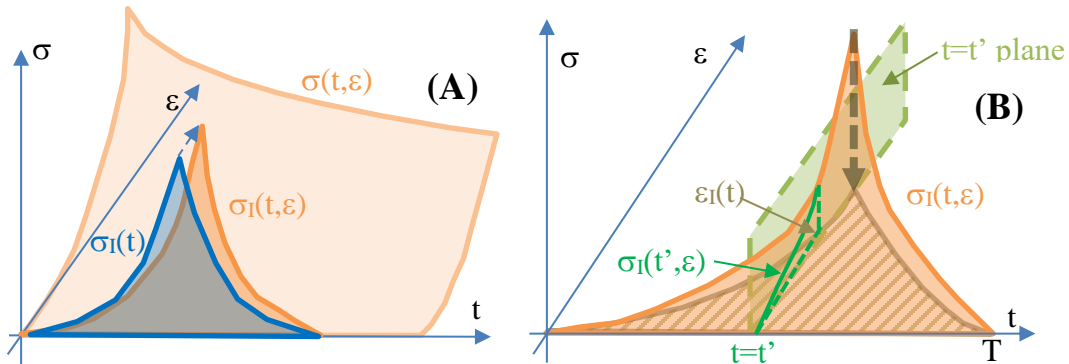
Figure 3-7: MEAD evaluation illustration

(A) shows the projection of an impulse stress $\sigma_I(t)$ (blue) onto the viscoelastic surface $\sigma(t,\varepsilon)$ (light orange) producing the projected surface $\sigma_I(t,\varepsilon)$ (deep orange). (B) shows the vertical cross-section (green) of the projected surface at a given time $t=t'$. The hashed area is the projection of $\sigma_I(t,\varepsilon)$ onto the ε-t plane where $\varepsilon_I(t)$ locates at its boundary.

$\varepsilon_I(t)$ is typically the smallest positive real root of Equation 3-6 for points within the boundary of the impulse stress pulse and within the physical extend of the viscoelastic surface of the material (i.e. within the elastic range of the material).

3.3.3.2.2   Deriving MEAD using a sawtooth impulse stress as an illustration.

The MEAD can be calculated numerically for any impulse stress waveform for any given material with its viscoelastic surface determined. In this study, as an illustration, a "saw-tooth" waveform was used for the impulse stress:

Equation 3-7: Saw-tooth impulse stress waveform

$$\sigma_I(t) = \begin{cases} \dfrac{S}{T}t, & 0 \le t \le T \\ 0, & T < t \end{cases}$$
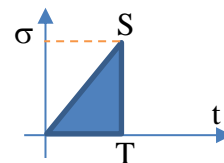
Substituting Equation 3-7 and Equation 3-1 into Equation 3-6 giving:

$$(p_{00} + p_{10}t + p_{20}t^2 + p_{30}t^3) + (p_{01} + p_{11}t + p_{21}t^2 + p_{31}t^3)\varepsilon - \frac{S}{T}t = 0$$

Solving for $\varepsilon_I(t)$:

Equation 3-8: Boundary curve for the sawtooth impulse stress projected onto the viscoelastic surface and then projected onto the strain-time plane

$$\varepsilon_I(t) = -\frac{p_{00} + (p_{10} - \frac{S}{T})t + p_{20}t^2 + p_{30}t^3}{p_{01} + p_{11}t + p_{21}t^2 + p_{31}t^3}$$

Evaluating the inner integral of Equation 3-5 using P_{31} approximation

Equation 3-9: Inner integral of MEAD equation

$$\int_0^{\varepsilon_I(t)} \sigma_I(t,\varepsilon)\,d\varepsilon \cong \int_0^{\varepsilon_I(t)} P_{31}(t,\varepsilon)\,d\varepsilon$$

$$= \int_0^{\varepsilon_I(t)} \left\{ \left[\begin{pmatrix} p_{31} & p_{21} & p_{11} & p_{01} \\ p_{30} & p_{20} & p_{10} & p_{00} \end{pmatrix} \begin{pmatrix} t^3 \\ t^2 \\ t \\ 1 \end{pmatrix} \right]' \begin{pmatrix} \varepsilon \\ 1 \end{pmatrix} \right\} d\varepsilon$$

$$= \left[\begin{pmatrix} p_{31} & p_{21} & p_{11} & p_{01} \\ p_{30} & p_{20} & p_{10} & p_{00} \end{pmatrix} \begin{pmatrix} t^3 \\ t^2 \\ t \\ 1 \end{pmatrix} \right]' \begin{pmatrix} \frac{1}{2}\varepsilon_I(t)^2 \\ \varepsilon_I(t) \end{pmatrix}$$

Approximate the continuous time interval of the impulse stress from 0 to T by a series of discrete values of fixed interval ΔT:

$[0…T] \cong [0, \Delta T, 2\Delta T, …, i\Delta T, …, n\Delta T=T]$ where $\Delta T=T/n$

For a given viscoelastic surface, all p_{ij} are known. For every $t_i = i\Delta T$, $i=0…n-1$, one can calculate $\varepsilon_I(t_i)$ from Equation 3-8 and the area under the stress-strain curve at t_i from Equation 3-9. The outer integral can be approximated by the summation of the volumes of width ΔT and area at t_i. Hence,

Equation 3-10: MEAD approximation based on equal discrete time steps

$$MEAD \equiv \frac{1}{T} \int_{t=0}^{t=T} \int_{\varepsilon=0}^{\varepsilon_I(t)} \sigma_I\,(t,\varepsilon) d\varepsilon\, dt \cong \frac{1}{T} \sum_{i=0}^{n-1} \left[\int_{\varepsilon=0}^{\varepsilon_I(t_i)} \sigma_I(t_i\,,\varepsilon)\, d\varepsilon \right] \Delta T$$

$$= \frac{1}{n} \sum_{i=0}^{n-1} \left[\int_{\varepsilon=0}^{\varepsilon_I(t_i)} \sigma_I(t_i\,,\varepsilon)\, d\varepsilon \right]$$

3.4   Results

The objective of this study was to characterize the large-range (till yield) cranial compressive and torsional viscoelastic properties of the unrestricted C5-C6 cervical IVD using kangaroos as the animal model.

3.4.1   Geometry and dimensions of kangaroo C5-C6 IVD

Kangaroo IVD has a structure similar to that of human IVD. It consists of an outer annulus fibrosus (AF) with concentric ring-like layers enclosing a gel-like nucleus pulposus (NP). Although the boundary between the AF and NP is not clearly visible, one can feel the boundary mechanically using a sharp object moving within the NP region. The NP is typically about 1/3 of the width and depth of the IVD. Figure 3-8A shows a cranial view of the C5 vertebra from its sectioned C4-C5 IVD. Figure 3-8B shows the cranial view of its C6 vertebra from its sectioned C5-C6 IVD. Both show a concentric ring like structure of the AF surrounding the NP.

A kangaroo C5-C6 vertebra is imaged using high resolution CT scan and the sagittal view is shown in Figure 3-7. It shows that the superior surface of a kangaroo C6 vertebra is convex. This is in contrast to that of the human C6 vertebra that is concave. The height or

thickness of the IVD at the center relative to the anterior and posterior locations would be larger in human than in kangaroo.
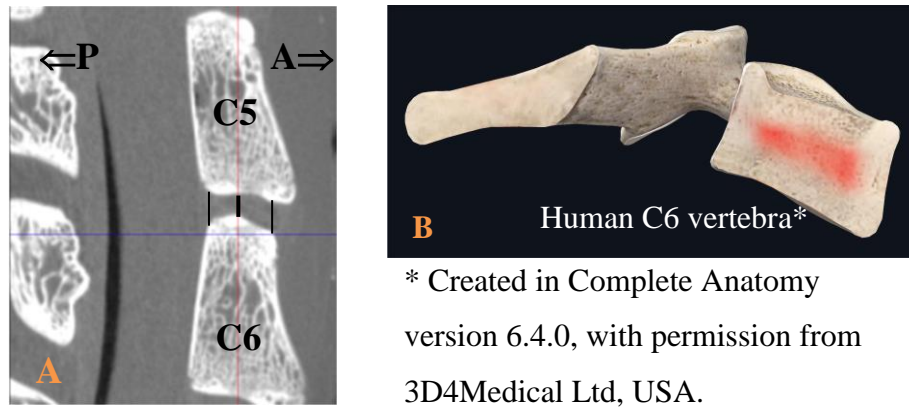
Figure 3-8: Sagittal view of a kangaroo C5-C6 IVD and a human C6 vertebra.

Figure A shows the convex nature of C6 superior surface making the mid height of the IVD shorter than its posterior and anterior height.

Figure B shows a sagittal cross-sectional view of a human C6 vertebra showing the superior surface is typically concave.
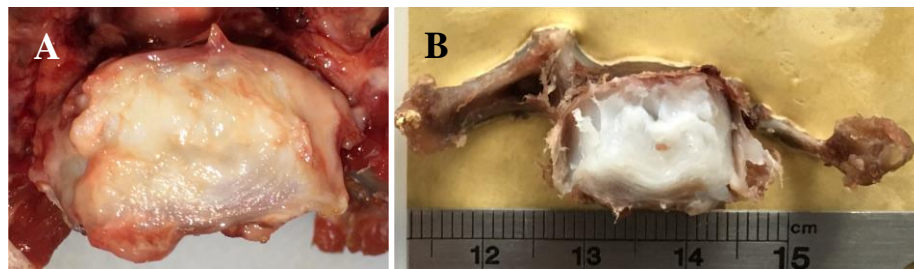
Figure 3-9: Kangaroo IVD

Figure shows the structure of kangaroo IVDs with the AF and NP region. (A) is a cranial view of C5 (C4-C5 IVD). (B) shows a cranial view of C6 (C5-C6 IVD). Both pictures belong to the same kangaroo specimen.

Using high resolution CT, frozen C5-C6 vertebral segment samples were scanned. Geometric dimensional properties of the C5-C6 IVD are collected and shown in Table 3-3. There are different ways to determine the height of an IVD in the literature. Measurements at the anterior position and at the disc center have been reported. We define the height or thickness of the disc to be the arithmetic mean of the anterior, mid and posterior height of the IVD measured on the sagittal plane. This is because the kangaroo spines we received are in frozen foldback states [Figure 3-1A&B]. Comparing to the human C5-C6 IVD, the height we determined for kangaroo IVD is about 2.8 mm, which is about 2/3 of that of human [Section 3.5.1]. The corresponding cross-sectional area of the kangaroo IVD is around 85 mm^2, which is about ¼ of the human counterpart [Section 3.5.1].

Table 3-3: Dimensions of kangaroo C5-C6 IVD

Dimensional properties	mean	SD	n	min	max	unit
Height	2.77	0.33	53	2.07	3.57	mm
Area	85.40	15.40	24	60.55	112.50	mm^2
Width *a* (left to right)	11.96	2.16	20	8.45	15.96	mm
Depth *b* (posterior to anterior)	6.93	0.95	20	5.74	6.93	mm

3.4.2   Mechanical properties

Stress-strain relationships of C5-C6 IVD were determined under compressive and torsional loads at different strain rates to failure. Typical test results are shown in Figure 3-9. The arrows in the Figure indicated the end of the elastic region. We measured their mechanical behavior and marked the end of their elastic regions, which we reported as their yield strengths. Some specimens failed right after the end of their elastic region
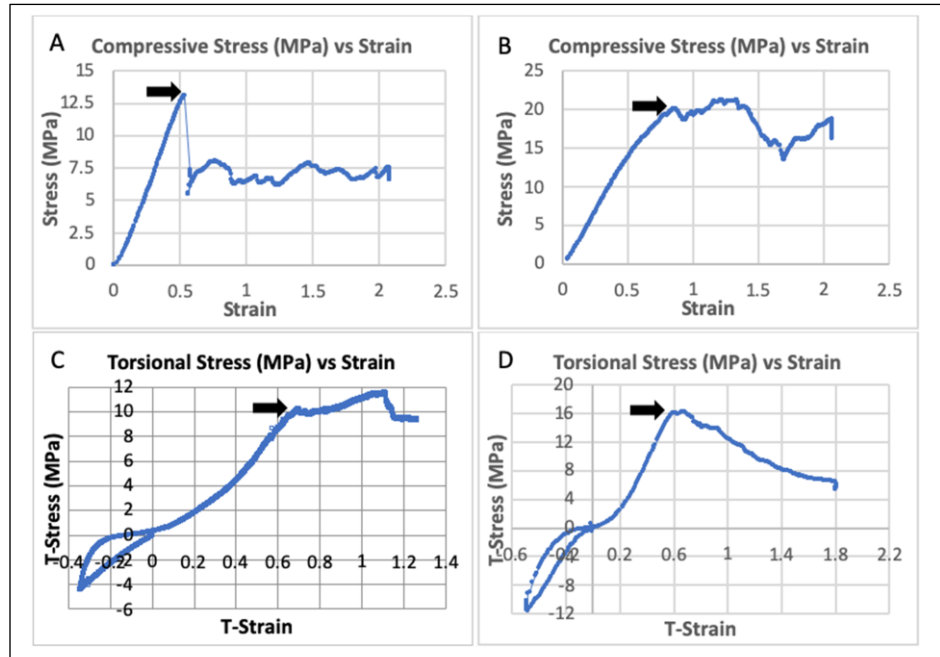
Figure 3-10: Typical compression and torsional test results.

At the end of their elastic region, some specimens failed immediately (A, D) while others continued to deform plastically (B, C). The arrow marks the end of its elastic region in each case and was taken as its yield strength.

(Figure 3-9A and D), and some had a long plastic deformation region (Figure 3-9B and C). Table 3-4 is a summary of the measured yield strength of the IVD.

Table 3-4: Yield strength of kangaroo C5-C6 IVD

Type	Property	mean	SD	n	min	max	unit
Comp yield	load	867.01	259.69	19	520.85	1671.89	N
	displacement	1.41	0.36	19	1.00	2.11	mm
	strain	0.55	0.17	19	0.36	0.87	-
	stress	10.88	3.42	19	5.16	20.18	MPa

Tor yield	torque	2.09	0.94	20	0.84	3.94	Nm
	angle	21.94	5.55	20	9.28	32.60	deg
	strain	0.66	0.17	20	0.25	1.01	-
	stress	13.31	5.00	20	4.26	21.80	MPa

3.4.3   Viscoelasticity

Mechanical behavior of the C5-C6 IVD is represented using a viscoelastic surface to correlate the stress, strain and time parameters. In this approach, a polynomial model has been found to approximate the collective viscoelastic behavior of all the specimens. The surface was generated using the least-square-error surface fitting method over all the test data of the specimens within their elastic ranges.

The use of viscoelastic surface has many advantages. The traditional viscoelastic behaviors such as creep, relaxation and stress-strain at different strain rate can be easily derived from this surface. To obtain a stress-strain curve of constant strain rate $\dot{\varepsilon}$, a stress relaxation curve of initial strain ε_0 and a creep curve of initial stress σ_0, just substitute $t = \varepsilon/\dot{\varepsilon}$, $\varepsilon = \varepsilon_0$ and $\sigma = \sigma_0$ respectively into Equation 3-1. In addition, it also allows the deduction of other material properties such as the impact resistance capacity of a given impulse stress mathematically [Section 3.3.3]. It can also be readily imported into most of the analysis software [Section 3.5.2].

The viscoelastic surfaces for compression and torsion of the C5-C6 IVD were generated using the procedure outlined and are shown in Figure 3-10. Two surfaces in each case were generated over time intervals of 0 to 500 s and 0 to 0.1 s. The long-time interval surface (Figure 3-10 A&C) indicated that the IVD is both compressive and torsional viscoelastic. The short duration plots (Figure 3-10 B&D) were used for deriving the IVD impact resistance for a series of 70 ms impulse stresses. The goodness of fit R^2 value is

shown in each case. Table 3-5 contains the coefficients (p_{ij}) of the fitted viscoelastic surface (P_{31}) of Equation 3-1.

Time	Compression $\sigma_c(t, \varepsilon_c)$	Torsion $\sigma_\tau(t, \varepsilon_\tau)$
0 to 500 sec	$R^2=0.9254$ (n=19)	$R^2=0.8588$ (n=13)
0 to 0.1 sec	$R^2=0.9475$ (n=15)	$R^2=0.9366$ (n=10)
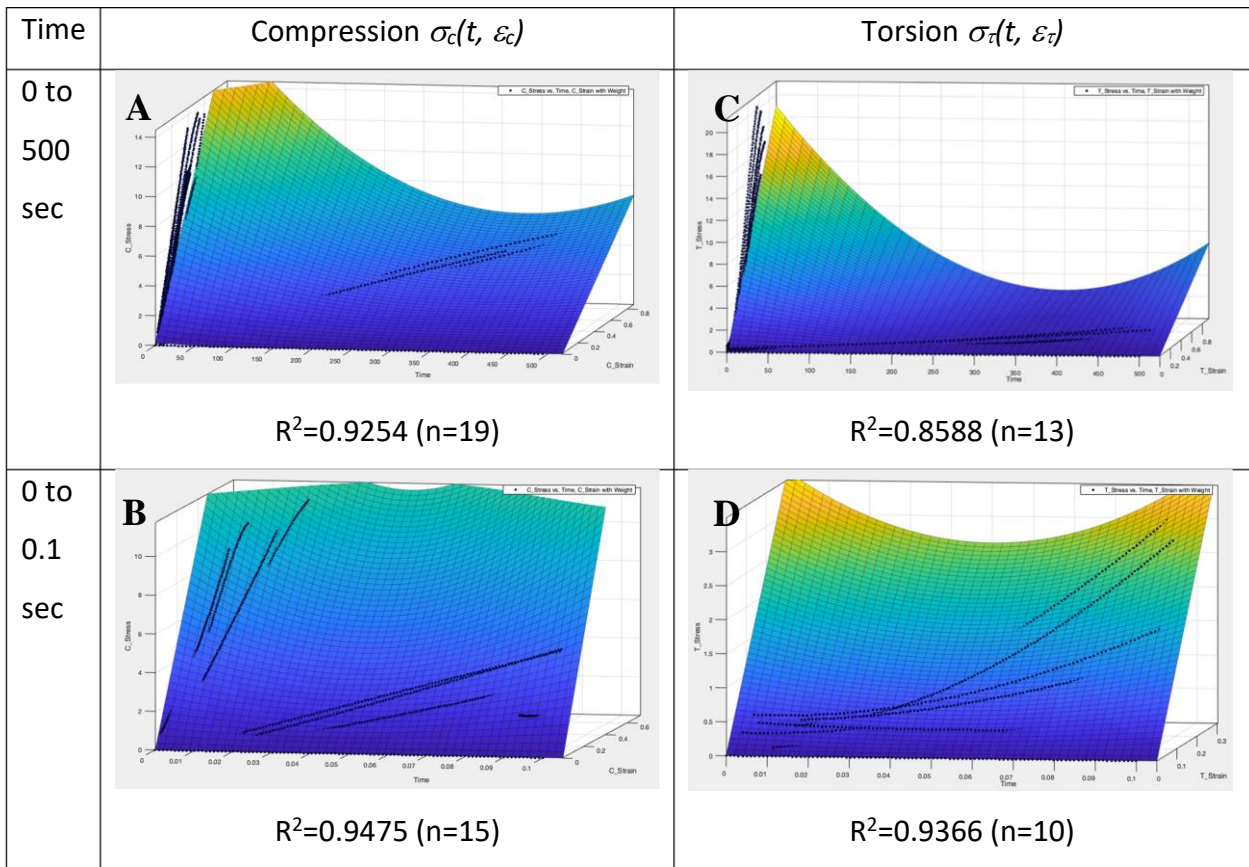
Figure 3-11: Resulting compressive (A&B) and torsional (C&D) viscoelastic surfaces.

Figure shows the resulting compressive (A&B) and torsional (C&D) viscoelastic surfaces providing the R^2 values of the goodness of fit and the number of specimens involved. A & C show that kangaroo IVDs are both compressive and torsional viscoelastic. The black dotted lines are the stress-strain data of an IVD tested under a constain strain rate. The color represents the residual error at the region. Dark colour is low and light is high.

The time axis: A&C 0→500s in 50s icrements, B&D 0→0.1s in 0.01s.

The strain axis: A&C 0→0.8 in 0.2 increments, B 0→0.6 in 0.2 and D 0→0.3 in 0.1.

The stress axis: A 0→14 MPa in 2MPa increments, B 0→10 in 2MPa, C 0→20 MPa in 2 MPa and D 0→3 MPa in 0.5 MPa

Table 3-5: Model polynomial P_{31} parameters p_{ij} values in Equation 3-1

p_{ij}	Compressive viscoelastic surface		Torsional viscoelastic surface	
	0 to 500 sec	0 to 0.1 sec	0 to 500 sec	0 to 0.1 sec
p_{00}	0.1801	-0.03681	-0.2023	0.01008
p_{10}	-0.003238	0.7946	0.002751	-0.1549
p_{01}	20.07	24.26	20.71	11.84
p_{20}	1.413e-05	33.32	-1.036e-05	1.873
p_{11}	-0.07037	-372.7	-0.1038	-132.7
p_{30}	-1.739e-08	-496.6	1.161e-08	-18.79
p_{21}	9.287e-05	4055	0.0001494	1332
p_{31}	0	0	0	0

3.4.4   Impact resistance

The impact resistance of a viscoelastic material such as the kangaroo C5-C6 IVD as defined in this study is the mean energy absorbed by the material over time [Section 3.3.3]. This is calculated as the volume sustained under the projected impulse stress curve onto the viscoelastic surface divided by the duration of the impulse stress [Figure 3-6]. This means the impact resistance value is dependent on the waveform of the impulse stress curve, $\sigma_I(t)$, its peak value S and its duration T. For a given waveform and with the viscoelastic surface determined, impulse stress can be calculated.

In this study impact resistance values of a series of impulse stresses having sawtooth waveforms with a fixed 70 ms duration but having increased peak values was determined as a function of increasing impulse stress. Figure 3-11 shows the result of the compressive and torsional impact resistance behavior. A trend curve was fitted over the

values. The curve shows the impact resistance varies almost as the square of the peak stress value in both cases.
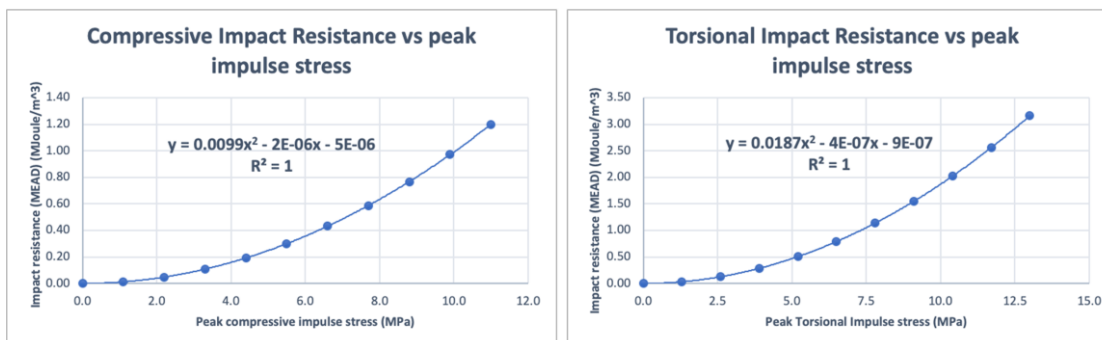
Figure 3-12: Impact resistance (MEAD) vs peak impulse stress S for a sawtooth impulse waveform Equation 3-7.

The impact resistance values were evaluated on 10 impulse stress of T=70 ms duration and peak values S from 0 to 11 MPa and 0 to 13 MPa for compressive and torsional impulses respectively. The maximum impulse stress values were taken from our measured results given in Table 3-4. The MEAD is measured in MJoule/m^3.

3.5 Discussion

3.5.1 Kangaroo vs human C5-C6 IVD properties comparison

The main purpose of using an animal model is to infer results to human applications. The ideal candidate for studying the biomechanical properties of IVD is obviously human. Unfortunately, due to the limited availability and choices of uniform human specimens, animal models, typically quadrupeds[75,82–86], are widely used in in vitro spinal research. Due to our upright standing posture, our cervical IVDs are under compression due to the weight of our head. This compressive pattern and magnitude are different from those of the quadruped animals. This study has hypothesized that kangaroos, having similar upright standing posture, similar weight and height to young adult human, will be a good model for IVD studies, especially in the cervical region.

The properties of kangaroo C5-C6 IVD can be compared to that of human in two areas:

- Yield stress & strain [Table 3-4]
- Compressive and torsional modulus values at same strain level and strain rate [Figure 3-12].

In this study, all yield stresses (compression & torsion) were measured under unrestricted (posterior and restricted structures removed) condition [Figure 3-2]. Most studies in the literature were performed with intact vertebral bodies. No values could be found for human C5-C6 IVD tested under same/similar conditions.

For compressive Young's modulus, Panjabi et al[61] had provided the following human C2-T1 IVD data (spine #87 C2-C6, #90 C3-T1, #105 C2-C7 & #106 C3-C7):

- Ellipse major axis a = mean disc width for all IVDs = 19.22 mm
- Ellipse minor axis b = mean disc depth for all IVDs = 15.36 mm
- Disc height = total disc height for all IVDs/# spines = 95.5/4= 23.88 mm
- Mean axil compression flexibility coefficient T_y = 7.1 ($\pm$ 8.4) mm/kN @ 0.7 mm
- Measurements were taken 30s after each load step application

The Young's modulus for human C2-T1 basing on these data is 14.5 MPa @ strain 0.03. The compressive Young's modulus for kangaroo found ranges from 20.0 MPa (t=0) to 6.7 MPa (t=379 s) [Figure 3-12]. At t=30s, E=18.0 MPa. Comparing these results, it would appear that the compressive strength of human C2-T1 IVD is in the same order of magnitude as that of kangaroo. However, the human IVD specimens tested was from C2-T1, not just C5-C6, and with full posterior and anterior bone structures.

For torsional modulus, human C5-C6 IVD data are taken from the following sources:

- Ellipse major axis a^{87} = mean (C5 EPWi, C6 EPWu) = 18.95 mm
- Ellipse minor axis b^{87} = mean (C5 EPDi, C6 EPDu) = 17.15 mm
- C5-C6 disc height[88] = IDH = 4.4 mm
- Secant stiffness[76] @ 11° = +RY = 1.033 Nm/deg

Applying Equation 3-4 on these data, the torsional modulus of human C5-C6 IVD is about 25 MPa. The torsional modulus for kangaroo found ranges from 20.7 MPa (t=0) to 2.7 MPa (t=347 s) [Figure 3-12]. Compare with the findings of this study, the torsional strength of human IVD would be about 17% stronger than the highest value of kangaroo but in the same order of magnitude. However, the human IVDs tested in that study had

full vertebral and discoligamentous structures preserved. Under this condition, the torsional strength measured should be higher than the unrestricted condition. In addition, the strain rate applied was not specified.

For impact resistance capacities for both compressive and torsional impact, to the best of our knowledge, we could not find comparable data in the literature for human C5-C6 IVDs evaluated or tested under similar condition to compare with the results obtained in this study.

In general, it is difficult to compare experimental results between studies because of the differences in test and data analysis methods used. In this case, due to the lack of human C5-C6 data in literature[30,89] tested under similar situation, the comparison between the kangaroo C5-C6 properties with human is inconclusive, however, they are likely to be in the same order of magnitude. In summary, our hypothesis that kangaroo cervical IVD is a good animal model for human counterpart research, though not proven, is plausible.

3.5.2   Linear viscoelasticity and Finite Element Methods (FEM)

One goal of this study, as mentioned in the Introduction section, is to derive the unrestricted viscoelastic behavior of the IVD to be used in FEM for simulating the spinal performance in a traumatic situation. In this discussion we will show how to incorporate the IVD material properties into a popular FEM software.

Linear viscoelasticity refers to viscoelastic material whose stress property is linear with respect to its strain value and only time dependent. Since the stress-strain relationship of the kangaroo IVD is represented by *P31* polynomial [Equation 3-1], its Young's (or torsional) modulus can be derived in Equation 3-11, which is independent of strain. This means that the kangaroo C5-C6 IVD is both compressive and torsional linear viscoelastic.

Equation 3-11: Compressive and torsional modulus

$$E(t) \equiv \frac{\partial \sigma}{\partial \varepsilon} \cong \frac{\partial P_{31}}{\partial \varepsilon} = p_{31}t^3 + p_{21}t^2 + p_{11}t + p_{01}$$

The time dependent compression and torsion modulus are plotted in Figure 3-12.
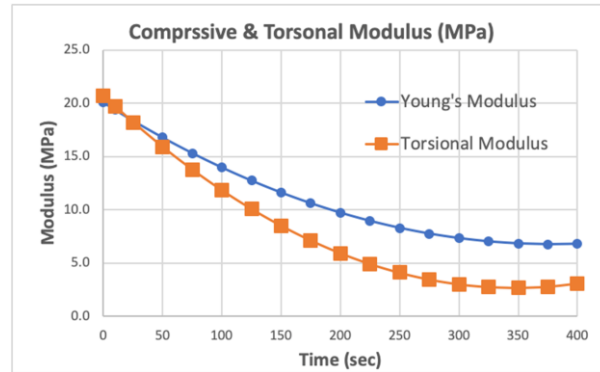
Figure 3-13: Compressive and torsional modulus.

Both were derived from the p_{ij} coefficients in Table 3-5 through Equation 3-1.

Many FEM software (e.g., ABAQUS and ANSYS) model viscoelastic behavior using the Prony series assuming the material is linear viscoelastic (at least for small strain changes). The Prony series[90] is defined as:

Equation 3-12: Prony series

$$E(t) = E_0 - \sum_{i=1}^{n} E_i \left(1 - e^{\frac{-t}{\tau_i}}\right)$$

Where E_i is the modulus from $t=0$ to time interval i, $E_0=E_{(t=0)}=p_{01}$ and τ_i is the effective time constant from $t=0$ to time interval i. The values of E_i and τ_i in Equation 3-12 can be obtained by using the least-square-error fitting of Equation 3-11 with minimum value of n having an acceptable R^2 value.

Currently most FEM software can accept the definition of a custom viscoelastic material by entering the experimental values of the Prony series, a relaxation curve, or a creep curve or both. For future development, in our opinion, the viscoelastic surface may be a more appropriate model and easier to implement. It can model both linear and non-linear viscoelasticity.

3.5.3 Method limitations

A major drawback of this method in deriving a quality representative viscoelastic surface is it requires a large number of specimens. This may be inappropriate for human specimens because of the cost and availability. In this study, due to the limited quantity of kangaroo IVDs available, the strain rates selected were more biased towards the high end for the impact resistance derivation. The mid-range was sparse resulting a slight saddle shape instead of a more ideal continuous decreasing value. An improvement can be achieved by adding a few stress-relaxation curves of high initial strain values to the data set.

Another limitation was due to Matlab. In deriving the viscoelastic surface using the Matlab curve fitting toolbox, it always returns p_{31}=0. This effectively reduces the modulus [Equation 3-11] to a quadratic relationship with t [Figure 3-12]. Since $\frac{d^2E}{dt^2} = 2p_{21} > 0$ for both compression and torsion [Equation 3-11], E decreases from its initial value p_{01} to its minimum at $t=-p_{11}/2p_{21}$. After that it will increase. This has presented a limitation in the time range for practical applications in using this model. The time limit for practical applications of the resulting model for the case of compression and torsion are t=379s and 347s respectively.

The resulting viscoelastic surfaces in this study were obtained by fitting only on the positive stress and strain values and assumed *stress* = 0 for *strain* = 0 for all time t. This essentially had ignored the small (compared to the yield value) neutral zone due to the hysteresis of the stress/strain curve in cyclic excitation situation, as in our torsional tests.

3.6 Conclusion

In this study, we have proposed a viscoelastic surface modeling method to characterize the unrestricted bulk material properties of the kangaroo C5-C6 IVD under axial compression and torsion. It has shown that they both are linearly viscoelastic. We have shown how traditional creep and relaxation behaviors can be derived from this generalized model and how to derive the Prony series constants to incorporate into popular FEM software. We have also used a simple triangular impact stress wave of

70ms duration to illustrate how one can derive the impact resistance of this impact stress from the model. Same method can be extended to a more complex impact stress wave once its stress waveform is known. The comparison of the kangaroo C5-C6 properties to that of human was inconclusive due to the lack of literature data tested under similar condition. Future studies will provide data for more conclusive comparisons. The viscoelastic surface model used in this study only models stress as a function of time and strain. The method is general enough to be extended to include multi-dimensional parameters such as temperature for example. Although temperature variation is not important for this study, other temperature sensitive viscoelastic materials can benefit from this method.

Chapter 4

4   IVD Prosthesis Development - Compression

Abstract

Although Artificial Disc Replacement (ADR) devices have been introduced for around 30 years, the long-term effects are still unclear. Recent studies on FDA-approved ADRs have reported development of adjacent segment degeneration (ASD), heterotopic ossification (HO), reduced range of motion (ROM) and subsequent fusion. This indicates rooms for improvements. We hypothesize that the culprit may due to the injuries and unnatural stress pattern introduced by current ADR devices over the affected vertebral surfaces triggering their over remodeling. To address this issue, we have developed the concept of a material candidate for an IVD prosthesis and conducted its feasibility study. The material can be patient-specifically molded into shape and fine-tuned to match the mechanical strength of an IVD. The material selected is a composite made from 10wt% polyvinyl alcohol cryo-gel (PVA) reinforced by long circumferentially oriented bamboo fibers. We have developed an analytical model on the compressive behavior of such a prosthesis. Basing on this model, we have derived the requirements of the fiber involved and have performed an evaluation on the suitability of the bamboo fiber chosen. This study has validated that the strength of the composite can be increase or decrease by changing the fiber content in the composite. The compressive results of prosthesis specimens at different strain-rates were measured and compared with that of the C5-C6 IVD obtained from our previous study using kangaroo as our animal model. Due to the unexpected substantial shrinkage of the PVA, the test results were weaker than the prediction of the analytical model and the measured animal IVD strength. However, we have shown that a 35% to 45% pre-strain of the material may resolve this issue.

4.1   Introduction

The Artificial Disc Replacement (ADR) treatment has emerged as an improvement over the traditional spinal decompression and fusion treatment by providing higher degree of spinal mobility for patients suffering from intractable radiculopathy originating from

degenerative disc diseases. One of its goals[3,22,91] was to prevent the onset of adjacent segment degeneration (ASD) observed in the fusion approach by preserving better natural spinal kinematics. Few such prosthetic devices have obtained FDA(US) and CE(EU) approval today [e.g. Bryan[13,18], ESP[16,92], M6[15,91], Mobi[93], Prestige ST[12,94], ProDisc[95], etc.]. Even though short term (< 4 years) evaluations are favorable[15,38,91,94,96], the long-term effects (>10 years) of these devices are still unclear. Some of the recently reported long-term problems include ASD[17,22], heterotopic ossification[17,22–24] (HO), subsequent fusion or spontaneous ankylosis[22], reduced ROM[17,22], postoperative kyphosis[27], myelopathy and radiculopathy[17]. While no main cause of culprit has been identified, the HO, reduced ROM and subsequent fusion may suggest that the vertebrae affected had been over remodeled to recover from injuries[22]. From other fields of orthopedic research[28,29], we learn that one main cause for bones keep remodeling is stress related, either on mismatch in stress distribution pattern or in material strength provided by the prothesis. Studying the design of current ADR devices and their associated surgical operations, we may hypothesize some of the causes of this mismatch. Due to their fixed sizes limitation, all ADR devices will have a smaller footprint than the patient's IVD replaced. This produces an unnatural higher stress pattern concentration in the middle part of the vertebrae. Most of the ADR devices are constructed with upper and lower metal plates. The vertebrae endplates have to be reshaped mechanically to fit these anchoring plates. While this does not just introduce injuries to the vertebrae, the metal plates are of much harder material. Furthermore, the contact between two hard surfaces will be spotty at best, creating micro concentrated stress points across the injured surfaces of the vertebrae. Some of the existing ADR devices are designed with fix axes of rotation or adopting a ball baring construction[94,95]. These devices only provide 3 degrees of freedom which are less than that of the human IVD. The axial alignment with patient's spine may become a problem creating different stress distribution in patient's mobility[27]. In short, there are rooms for improvements.

Our long-term research goal is to develop a prosthesis that can mimic closely the shape and mechanical properties of the human IVD. The material properties can be fine-tuned to match that of any IVD in any position in the spine. The shape can be molded to fit the target IVD of individual patient. The contact surfaces of the prosthesis with the vertebrae

should be able to adapt automatically to that of the vertebrae endplates. The aim is to maintain the original footprint of the replaced IVD, to control the stress distribution over the entire contact surfaces of the vertebrae and to reduce the damages to the affected vertebrae for its implantation. The goal of this feasibility study is to develop a proof-of-concept material candidate for such a prosthesis. The development of an actual prosthesis prototype and related implantation issues are left for future studies.

The material candidate we had chosen for this study is a composite of thermally cross-linked 10wt% polyvinyl alcohol hydrogel (PVA) reinforced by long circumferentially arranged bamboo fibers. The PVA provides a biocompatible and long-term stable body for this prosthesis. The circumferential reinforced fibers provide compressive strength to the composite body. Bamboo fiber is a renewable plant cellulosic fiber with possible antimicrobial properties[97,98]. The mechanical properties of PVA, bamboo fiber and composite and their suitability for IVD prosthesis are studied in this Chapter.

4.2 Materials and Methods

4.2.1 Experimental approach

To analyze the requirements for our IVD prosthesis material, an analytical model [Section 4.6] has been developed for the compressive behavior of a simplified IVD prosthesis (short cylindrical shape) constructed from a composite material with long circumferentially oriented embedded fibers. The assumptions of this derivation are based on ideal incompressible materials and energy conservation during the compression.

The analytic model predicts the compressive strength S (stress value) of such a composite, at a given strain value, is dependent on the Young's Modulus of the fiber E_f used and increases monotonically with the volumetric percentage of fiber content f within the composite.

The goal of the experimental validation is to establish the feasibility that, for any IVD of given strength and a given fiber type, one can find f that will meet the compressive strength of the IVD within its physiological range. Hence the key concept employed in our experiment is to validate the monotonous increasing relationship as predicted by the

model. Once this relationship is validated, one can simply use a binary search technique to find the exact fiber content *f* for this IVD. This search is left outside the scope of this study.

The experiment in this study is to validate the hypothesis that, for 3 batches of specimens of different fiber content *f* and measured strength *S* at a given strain, if $f_2 > f_1 > f_0 = 0$ (control) then $S_2 > S_1 > S_0$ (control) for all strain values.

To validate this hypothesis, the stress-strain test results of specimens from the three batches tested at the same compression rate are compared with each other. This will indicate the strength of each batch relative to the others. Because there are 11 strain rates involved, to limit the number of comparisons, we only choose the test results from a set of 6 representing strain rates for this comparison exercise. The chosen strain rates spread throughout the entire range used within the experiment.

The C5-C6 IVD is chosen as the prosthesis development target. Its mechanical behavior (compressive and torsional) has been measured from kangaroo C5-C6 IVDs as the animal model from a previous study [Section 3]. Basing on the results of this study, the requirements for the selection of our fiber are derived.

To validate the suitability of the specimen material as a candidate for IVD prosthesis, the stress-strain curves of the kangaroo IVD at the set of 6 chosen strain rates are derived from the viscoelastic surface of the kangaroo IVD. Comparisons are made between the kangaroo stress-strain curves with those from the strongest batch found from previous comparison.

4.2.2   Bamboo Fibers Characterization

Two pounds of undyed natural spinning bamboo fiber in 4 oz bundles were procured from Fiberlady (438 South Fork Drive, Lewisville, TX, USA) [Figure 4-1].
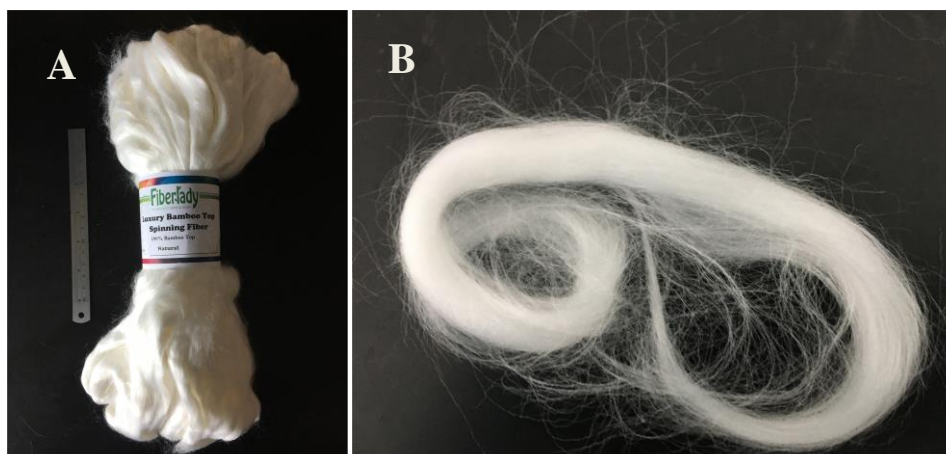
Figure 4-1: Bamboo fibers

"A" shows one of the 8 bundles of fibers purchased scaled by a 6" steel ruler. "B"
is a close-up view of a random sample of the fiber selected from the bundle
revealing the highly aligned nature of the fibers.

4.2.2.1   Basic properties investigation

The fiber density was measured using volume displacement method. 20.7g pre-weighted
fiber was submerged fully into a pre-measured 500ml DI-water (at room temperature).
The displaced volume was measured (measuring cylinder graduated in ml).

The morphology of the fibers was imaged using SEM (LEO 1540XB, precoated 5nm
Osmium). The material was investigated using FTIR (Bruker model Vector22, resolution
2 cm^{-1}, 64 scans) and results analyzed by Bio-Rad software (KnowItAll with IR Spectral
Library).

4.2.2.2   Fiber dimension and strength measurement

19 randomly sampled fibers were individually identified, length measured using scaled
photo method (iPhone 6S, 6" steel ruler, ImageJ) and mean diameter determined using
optical microscope (Olympus BX60, 8 to 10 50X images taken along the full length of

the fiber, 6 to 10 diameter measurements on each image using ImageJ, mean diameter averaged over all measurements of the fibers).

The tensile stress-strain characteristic of each fiber specimen was determined using a mechanical tester (Instron 8874, calibrated Transducer Techniques 1000g load cell, self-designed fiber attachment fixture) at a displacement rate of 0.125 mm/sec. The mean stress-strain curve, yield stress and strain value were calculated based on the 19 samples (MS Excel).

Figure 4-2 shows the complete measurement process applied to each fiber selected.

Figure 4-2: Property measurement process of a bamboo fiber

This series of photos illustrate the complete process applied to measure the geometric and mechanical properties of a typical bamboo fiber. "A" shows the length measurement using a scaled photo technique. "B" shows the fiber mounted on a microscope slide for diameter measurements under an optical microscope. "C" shows a 50X image of a portion of the fiber for diameter measurements. "D" shows the fiber mounted on a specially designed mechanical test jig. "E" shows the fiber mounted for mechanical testing.

4.2.3   Prosthesis samples preparation

The 10wt% Polyvinyl Alcohol (PVA) solution was prepared by adding PVA (Sigma-Aldrich Pcode 363065-500G) to 1X PBS (fisher scientific CAS 7647-14-5,7447-40-7) solution in 1:9 ratio by weight. The solution was mechanically stirred in a container

immersed in a paraffin oil bath maintained at 90°C. The solution was stirred continuously until the PVA was fully dissolved.

Three batches (B0, B1 and B2) of 50 samples each (mold diameter 23mm and thickness 8.67mm in 5x5 formation) were prepared containing bamboo fibers of weight 0g (control, $f_0=0v\%$), 37.3mg (sd 0.8) ($f_1\approx0.6v\%$) and 175.4mg (sd 1.6) ($f_2\approx3v\%$) respectively. The fibers were wound loosely around a 5mm spindle in a fixed direction spiraling along the length of the spindle before inserted and packed down into each mold. The spindle created a void region in the center of the mold mimicking the NP region of an IVD. Hot (~80°C) 10w% PVA solution was added to fill the molds. The molds were sealed by sandwiching in between two 3mm thick rubber sheets and two 4mm thick aluminum plates. The molds were held watertight by surrounding screws and totally immersed into a 50% antifreeze bath to go through 6 freeze-thaw cycles (FTC, +20°C ↔ -20°C). After the FTCs, the samples were removed from the mold and visually inspected to eliminate defective ones (bubbles, holes, deformation, etc.). Each remaining specimen was individually identified, cross-section area measured (average of top and bottom surface) using scale photo technique (iPhone 6S, 6" steel ruler, ImageJ) and stored individually in 1X PBS solution before testing. This had harvested 35, 31 and 26 specimens for B0, B1 and B2 respectively for compression testing.

Figure 4-3 shows some stage results of this process.
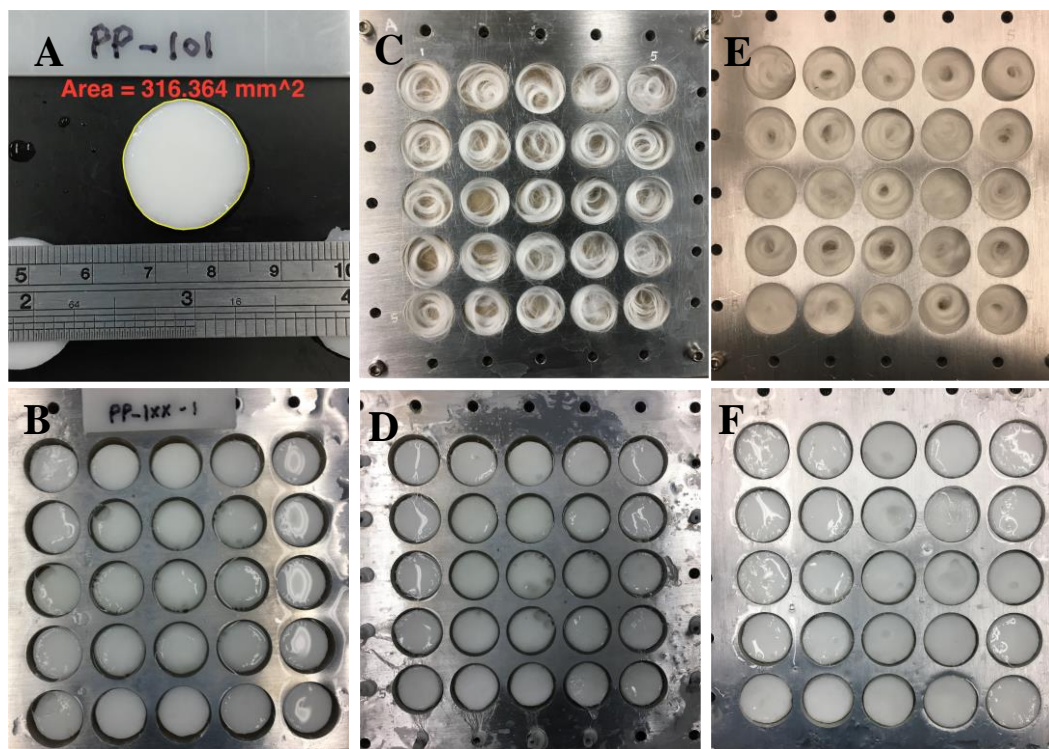
Figure 4-3: Prosthesis samples preparation process.

Picture "A" shows the area measurement of one specimen using scaled photo technique. Picture "B" shows samples of batch B0 (control) with no fibers. Picture C and D shows samples of batch B1 containing 0.6v% of bamboo fibers. Picture E and F shows samples of batch B2 containing 3v% of bamboo fibers. Picture C & E shows the bamboo fibers were inserted mainly in the outer region of the samples and wound circumferentially in one direction leaving a void center to mimic the NP region of an IVD. Note the shrinkage of the samples within the molds in B, D and F as a result of the 6 FTCs of the 10% PVA hydrogel cross-linking process.

4.2.4   Compressive Test

Mechanical testing was performed on an Instron 8874 machine using a ± 10kN and 100Nm load cell between two flat parallel aluminum surfaces. Testing was performed within a 1X PBS solution bath [Figure 4-4].
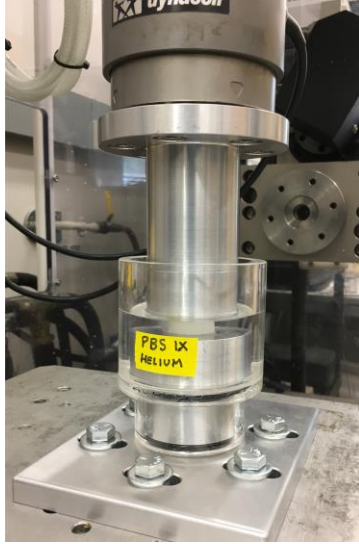
Figure 4-4: Prosthesis specimen mechanical testing setup

Each specimen was tested between two parallel circular plates immersed in a 1X PBS solution bath.

Each sample was subjected to a two-stage pre-conditioning steps. The purpose was to reduce the internal stresses built-up during the FTCs of the PVA process. The initial height of the sample was determined by lowering the distance of the two compression surfaces until a 1N force was registered. It was then slowly compressed by 0.8 mm at a rate of 0.25mm/min. The position was held for 1min and then subjected to a sine oscillation at 0.1Hz, amplitude 0.25mm for 15 minutes. Load was removed for 2 minutes to allow the sample to fully relax before the main compression test.

The height of each sample prior to the compression test was first measured by lowering the compression surfaces until a 1N force was registered. Each sample was compressed to about 0.9 strain at a compression rates given in Table 4-1. Table 4-1 also shows the number of samples in each batch using the same compression rate.

Table 4-1: Compression rates and the number of specimens involved

Compression rates	Strain Rate*	B0 (f_0=0v%)	B1 ($f_1 \approx 0.6$v%)	B2 ($f_2 \approx 3$v%)
0.25 mm/min	0.04/min	3	3	3

1.5 mm/min	0.21/min	3	-	2
0.125 mm/s	0.02/s	3	2	-
0.25 mm/s	0.04/s	2	3	3
0.5 mm/s	0.07/s	3	3	-
1 mm/s	0.14/s	3	3	3
2 mm/s	0.29/s	2	3	-
5 mm/s	0.71/s	3	3	3
10 mm/s	1.42/s	3	3	3
25 mm/s	3.57/s	3	3	3
50 mm/s	7.14/s	3	3	3
Total specimens		31	29	23

* Approximate strain rate based on mean specimen height of 7.0 mm (Table 4-4).

4.2.5　Hypothesis validation

Figure 4-5 A&B shows the test data of a typical specimen. There were short durations of delay and possible load vibrations at the beginning and end of motion. Avoiding these transient regions, the raw test data was extracted from the elastic region and converted to stress and strain values basing on the geometry of the specimen under test [Figure 4-5 C&D]. Two equations were extracted (MS Excel) from the test data: (1) the strain vs time equation and (2) the stress vs strain equation. Because of a constant compression rate used, equation (1) was a linear equation. Equation (2) was a polynomial of degree $n \leq 5$. The start and end points of equation (1) and (2) were recorded. The t_1, t_2, ε_1 and ε_2 specified the valid range of the experimental data for this specimen.

Equation (1), t1 and t2 were measured in the experimental time domain. The viscoelastic surface should be in model time domain, i.e., the stress and strain start from time zero. To convert from experimental time to model time, Equation (1) was extended to cut the experimental time axis at t0. Equation (1) was then time shifted by t0, then t1 and t2 became t1' and t2' respectively. The slope of Equation (1) also represented the strain rate the specimen was tested under. To regenerate the test data of the specimen in the viscoelastic model domain, 100 equal time intervals were inserted between t1' and t2'. If t2' was greater than 500 seconds, it was held to a maximum of 500 seconds to limit the time range of the model. For the time at the end of each time interval, the strain and stress values were generated from the time shifted Equation (1) and Equation (2) respectively. The regenerated data of all specimens in the batch were plotted in the stress-time-strain domain (MATLAB). A polynomial surface $Pmn(t, \varepsilon)$ was fitted using least-square-error technique (MATLAB Curve Fitting tool) over all these data finding the minimum m and n to result in an acceptable R^2 value. The coefficients of this polynomial and the mean end stress (or yield stress) and the mean end strain (or yield strain) were calculated as the valid boundaries of the viscoelastic surface.

To validate the strength of each batch of specimens, the stress-strain data for all specimens tested within the approximate strain rates of 0.04/min (0.25mm/min), 0.04/s (0.25mm/s), 0.14/s (1mm/s), 0.71/s (5mm/s), 1.42/s (10mm/s) and 3.57/s (25mm/s) are plotted on the same graph, one for each strain rate.

To validate the suitability of the specimen material as an IVD prosthesis material candidate, the stress-strain data of the kangaroo IVD for the set of 6 strain rates was also generated basing on the 500 second viscoelastic surface of the kangaroo IVD derived from **Error! Reference source not found.** and plotted against those of the mean stress-strain curve of all the specimens in the strongest batch found in the previous comparison.
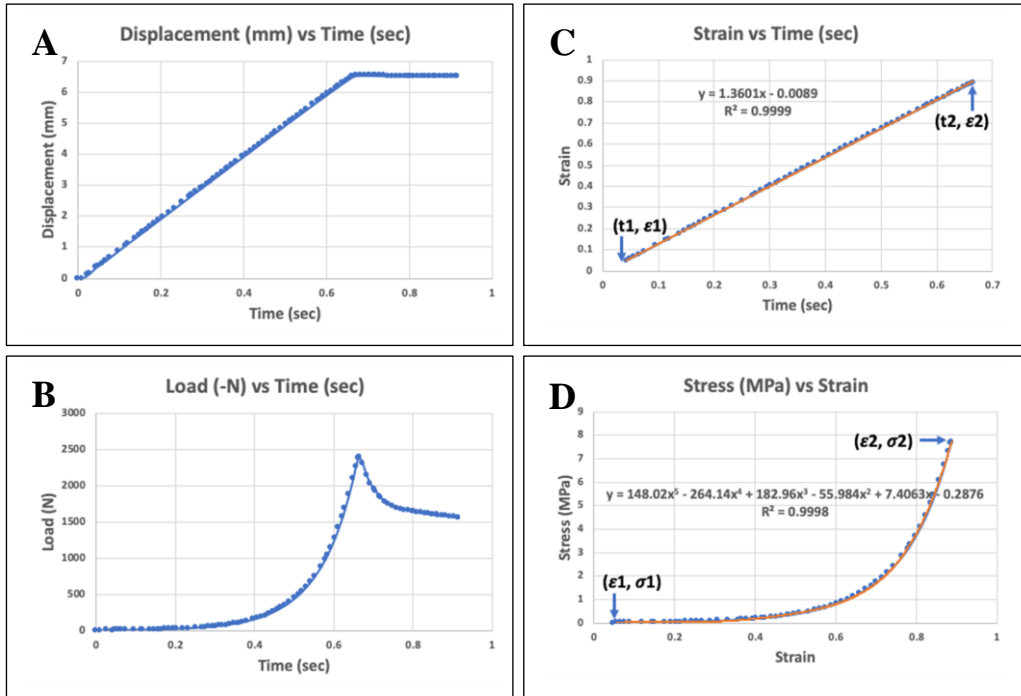
Figure 4-5: Typical test data of a specimen and processing.

"A" and "B" are data captured of the displacement vs time and load vs time respectively. "C" and "D" are the extracted elastic region from "A" and "B" and converted into stress and strain values basing on the geometry of the specimen. The linear equation of strain vs time is obtained from data in "C" and the polynomial equation of stress vs strain is obtained from the data in "D".

4.3 Results

4.3.1 Derivations from analytical model

The C5-C6 IVD was used as our prosthesis development target. We used kangaroo C5-C6 IVDs as our animal model and measured their compressive behavior in a previous study [Section 3]. Assuming the physiological compression of the IVD is around 10%. The mean compressive modulus of the kangaroo IVD (n=19) measured was 19.8 MPa (compression rate 0.14/s). At strain value of 10% and the tensile modulus of 10% PVA-C measured in Section 4.7 was 0.17 MPa (tensile strain rate 0.1/s), the analytical model

predicts the tensile modulus E_f required for the chosen fibre with volumetric fill of 0.6%, 3%, 5% and 10% are found to be 9.8 GPa, 2.0 GPa, 1.8 GPa and 590 MPa respectively.

In addition, the analytical model assumes the fibers should wind continuously around the circumference of the prosthesis, this gives additional requirements to the fiber: (1) the fibers should be highly aligned in a bundle and (2) the individual fiber length should be greater than 72mm for a 23mm diameter mold.

4.3.2   Bamboo fiber properties

Under SEM [Figure 4-6] and high-power optical microscope [Figure 4-2 C] observations, each strand of the bamboo fiber sampled for mechanical testing [Figure 4-2] was actually formed by a bundle (> 6) of fibrils (typical diameter < 10 μm) bounded together.
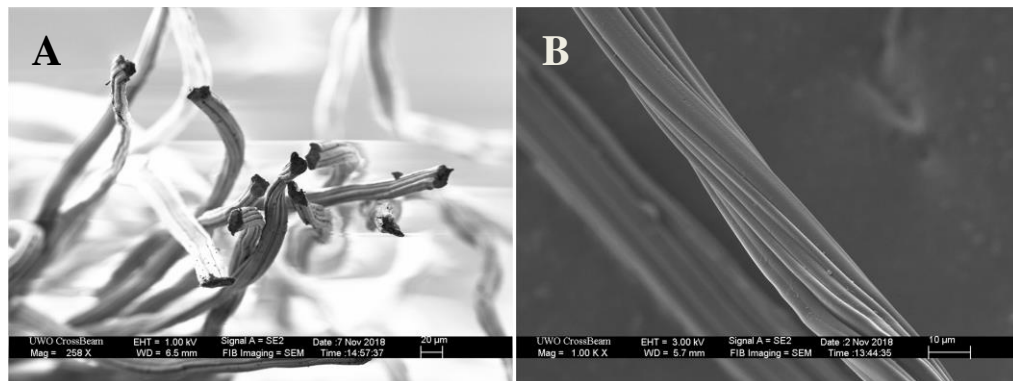
Figure 4-6: SEM images of the bamboo fibers

"A" was at 250X and "B" at 1000X magnification. The images reveal that each strand of the bamboo fiber used in this experiment was actually consisting of a bundle of fibrils bounded together.
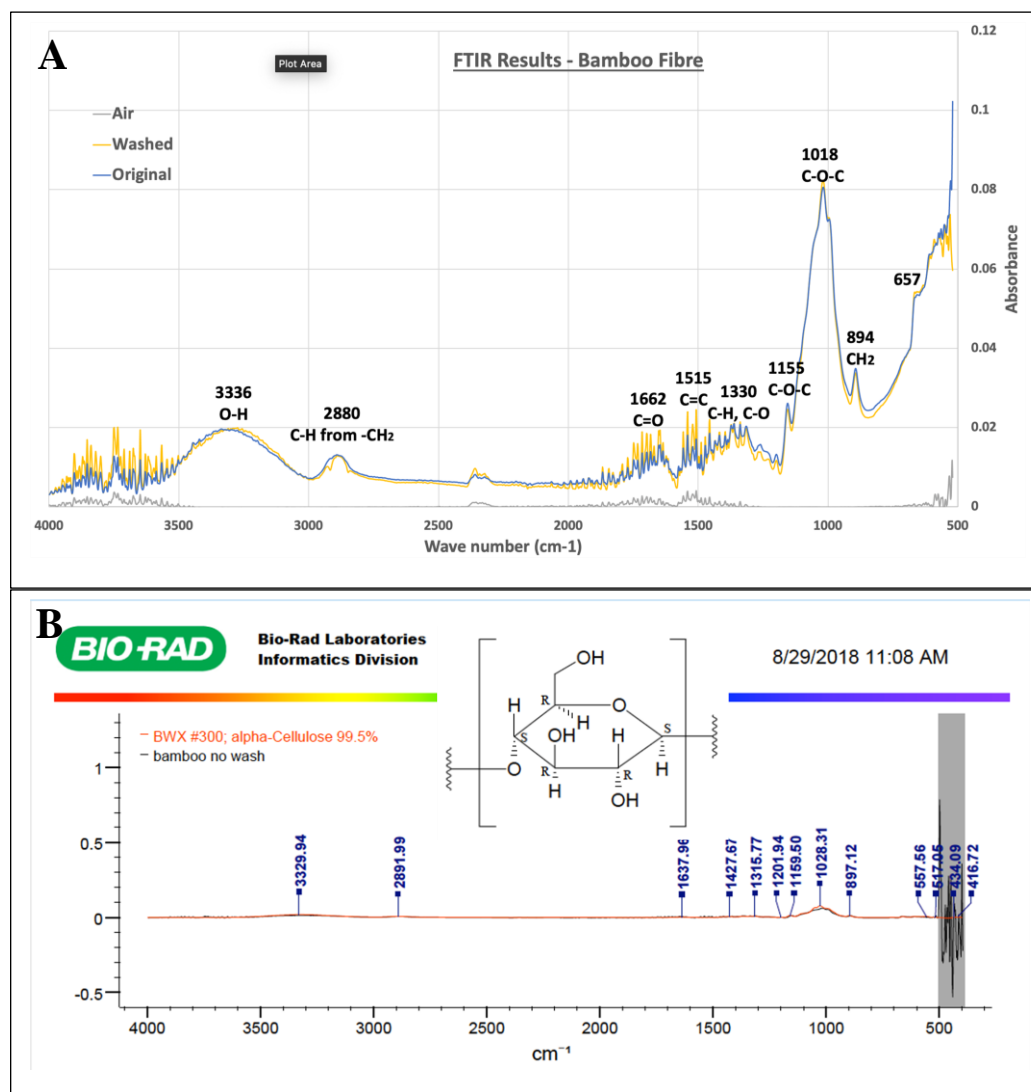
Figure 4-7: FTIR results of bamboo fiber.

A: The FTIR results of a washed sample and an original sample of the bamboo fiber. The washed sample were washed with and immersed in DI-water at room temperature for 3 days with water replaced daily and then air dried.

B: The FTIR data of the original sample was analyzed by Bio-Rad KnowItAll software, indicating that the sample's FTIR signature matches that of alpha-cellulose at 99.5%.

Figure 4-7A shows the FTIR results of a washed sample and an unwashed sample of bamboo fiber. The similar FTIR pattern indicates the washing did not alter the chemical contents of the fiber. Figure 4-7B shows the FTIR results of the unwashed fiber analyzed by BIO-RAD KnowItAll software revealing that the signature of the fibers matches those of alpha-cellulose at 99.5%. This had validated the plant origin of the fibers, however, didn't identify that they were bamboo fibers.

Figure 4-7A has identified the absorption peaks attributed to the chemical bonds[99–102] in the samples. The FTIR signature compared significantly well with those for bamboo fibers reported by Liew et al[99] and Wang et al[101]. The absorption peaks around 1018 and 1155 cm^{-1} are signatures for the C-O and C-C bonds for cellulose[102]. The C=C stretching vibration in the aromatic ring of lignin can be attributed[99] to the absorption peak around 1515 cm^{-1}. The C-H stretching vibration present in cellulose molecules commonly related to the lignin component can also be accounted[100] for the peak around 2880 cm^{-1}. Both indicate the existence of lignin in the sample.

For the density measurement, the volume displaced by 20.7g of fiber was 12.9 ml $\pm$ 0.5 ml, hence the density of the fiber was about 1.6 g/cc. The volumetric fiber content for batch B1 and B2 was based on this density measurement.
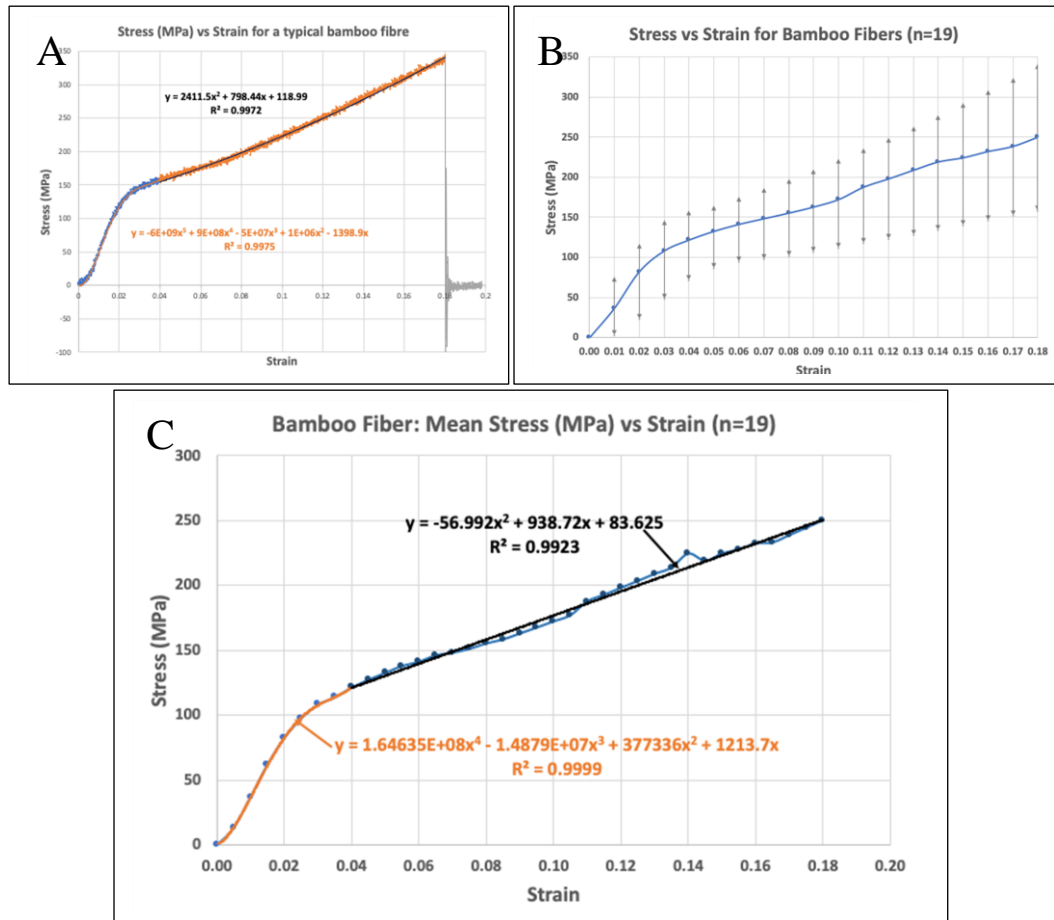
Figure 4-8: The stress-strain properties of bamboo fibers.

"A" shows the stress-strain curve for a typical bamboo fiber. "B" shows the stress-strain behavior of all 19 test samples with mean and max-min range at each strain value. "C" shows the mean stress-strain curve for all test samples. In both "A" and "C", fitted curves are provided in two segments: one below the bend and one above the bend.

For mechanical testing, Figure 4-8A shows a typical stress-strain curve of our bamboo fiber specimens. It reveals a 2-region nature of the stress-strain behavior before breaking: an "S" shape region and roughly linear region. The transition point between these two regions varies between 0.03 to 0.06 strain among our specimens. There are no known

explanations found in the literature for the cause of these two regions for bamboo fibers. The SEM images [Figure 4-6] had revealed the multi-stranded substructure of the fiber; however, it is not known that each fibril within the fiber had extended the full length of the fiber. We postulate that the initial "S" curve might be due to the strength of the bundle held together by lignin. The linear region may be due to the sliding of the fibrils within the bundle. Figure 4-8B shows the mean and extend of the stress-strain values measured among our 19 samples and Figure 4-8C and Equation 4-1 provide the two fittings of the mean stress-strain curve of all our specimen (n=19).

Equation 4-1: Mean Stress-Strain curve of bamboo fibers (n=19)

$$\bar{\sigma} = \begin{cases} 1.65 \times 10^8 \varepsilon^4 - 1.49 \times 10^7 \varepsilon^3 + 377336\varepsilon^2 + 1213.7\varepsilon & 0 \leq \varepsilon < 0.04 \\ -56.992\varepsilon^2 + 938.72\varepsilon + 83.625 & 0.04 \leq \varepsilon < 0.18 \end{cases}$$

Basing on Equation 4-1, we can calculate the Young's modulus of the fiber at different strain value [Table 4-2]. Its Young's modulus ranges from 4.95 GPa to 1.46 GPa in the S region and approximately 926 MPa in the linear region.

Table 4-2 provides the Young's modulus of the bamboo fiber at a set of strain values basing on Equation 4-1.

Table 4-2: Mean Young's modulus of bamboo fibers

Strain	Young's modulus	Unit
0.01	4.95	GPa
0.02	3.72	GPa
0.03	1.46	GPa
≥0.04	~926	MPa

Table 4-3 summarizes the results of our findings on the bamboo fiber properties.

Table 4-3: Bamboo fiber properties (n=19)

Fiber Properties	Mean	SD	Min	Max	Unit
Fiber length	92.68	10.35	78.60	120.00	mm
Fiber diameter	20.79	1.87	17.35	24.94	μm
Yield* force	64.4	15.99	32.9	89.8	mN
Yield* strain	0.108	0.055	0.025	0.193	
Yield* stress	190	64.17	102.5	338.3	MPa

* Yield represents the end of the linear region which is also the break point of the fiber.

4.3.3   Prosthesis Compressive Test Results

4.3.3.1   Dimensional and yield properties

As shown in Figure 4-3B, D and F the specimens had considerable shrinkage after the 6 FTCs. Table 4-4 summarizes the measured geometric properties of the prosthesis specimens and the shrinkage calculated based on a 23mm diameter 8.7mm height mold. This unexpected shrinkage has presented a considerable deviation from the prediction of the analytical model.

Table 4-4: Geometric properties of the prosthesis specimens (n=92)

Properties	Mean	SD	Min	Max	Unit	Mold	Shrinkage
Height	7.0	0.4	5.4	7.6	mm	8.7	20%
Area	328.7	23.4	281.4	385.3	mm^2	415.5	21%
Volume	2285.0	124.8	1913.8	2583.4	mm^3	3614.6	37%

The compression of specimens in B0 and B1 did not yield up to 0.9 strain. The same was true for specimens in B2 at compression rate of 0.25mm/min (~0.04/min). Yields only occurred for specimens in B2 at or above strain rate 0.04/s. Table 4-5 shows the yield characteristics of specimens in B2 (n=18 out of 23).

Table 4-5: Compressive properties of B2 specimens (n=18 out of 23).

Properties	Mean	STD	Min	Max	Unit
Yield* Load	3.23	0.81	2.28	5.03	kN
Yield* Strain	0.76	0.08	0.58	0.87	
Yield* Stress	8.95	2.30	6.22	14.34	MPa

* Yield represents the end of the elastic region.

4.3.3.2   Viscoelastic properties evaluation

Figure 4-9 performs an evaluation on the viscoelasticity of the prosthesis using specimens in B2. Each stress-strain curve is the mean (n=3) of the specimens at that strain rate group. The increasing strength of specimen at higher strain rate has validated that the specimens are viscoelastic. The same results are true for specimens in B0 and B1 but at a lesser degree. Figure 4-9 also derived the mean stress-strain curve of B2 specimens:

Equation 4-2: Mean stress-strain curve for B2 prosthesis specimens

$$\sigma = -3.4621\varepsilon^3 + 18.516\varepsilon^2 - 3.7763\varepsilon + 0.0759$$
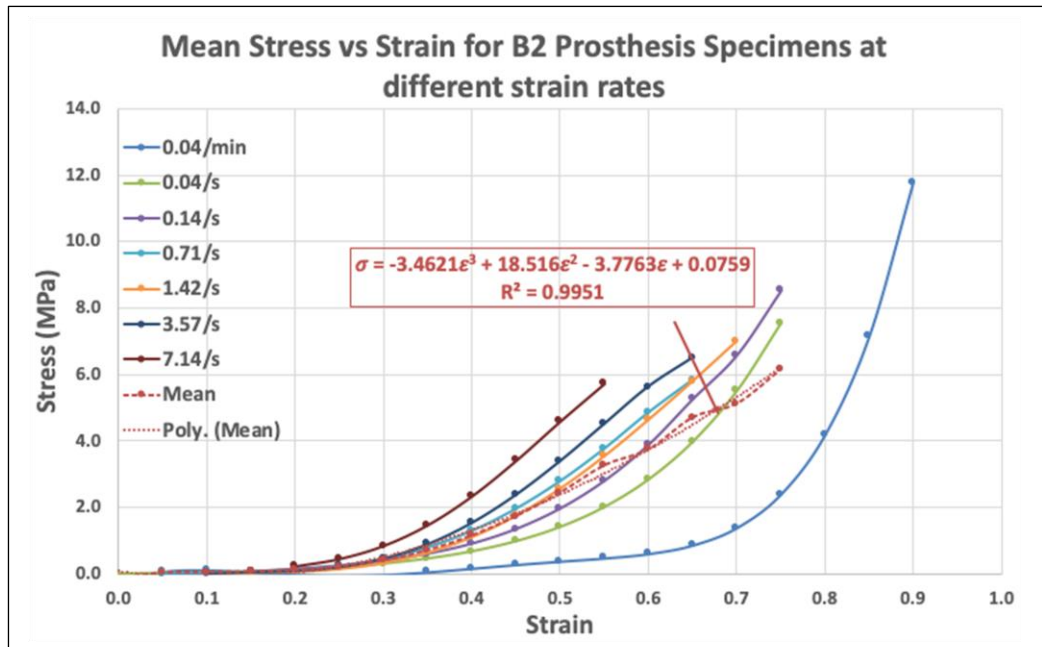
Figure 4-9: Viscoelastic properties of B2 specimens

This figure contains the mean stress-strain curve of all specimens of B2 tested at each strain rate from 0.04/min to 7.14/s showing the mean strength of the specimens increases at increasing strain rates. This illustrates that the material is viscoelastic.

4.3.4   Stress-Strain comparison for B0, B1 and B2

To compare the strength of specimens in B0 (0v%), B1 (0.6v%) and B2 (3.0v%), their stress-strain test results of specimens at the 6 selected strain rates were plotted against each other. The color code used is B0 (0v%) in green, B1 (0.6v%) in blue and B2 (3.0v%) in orange.
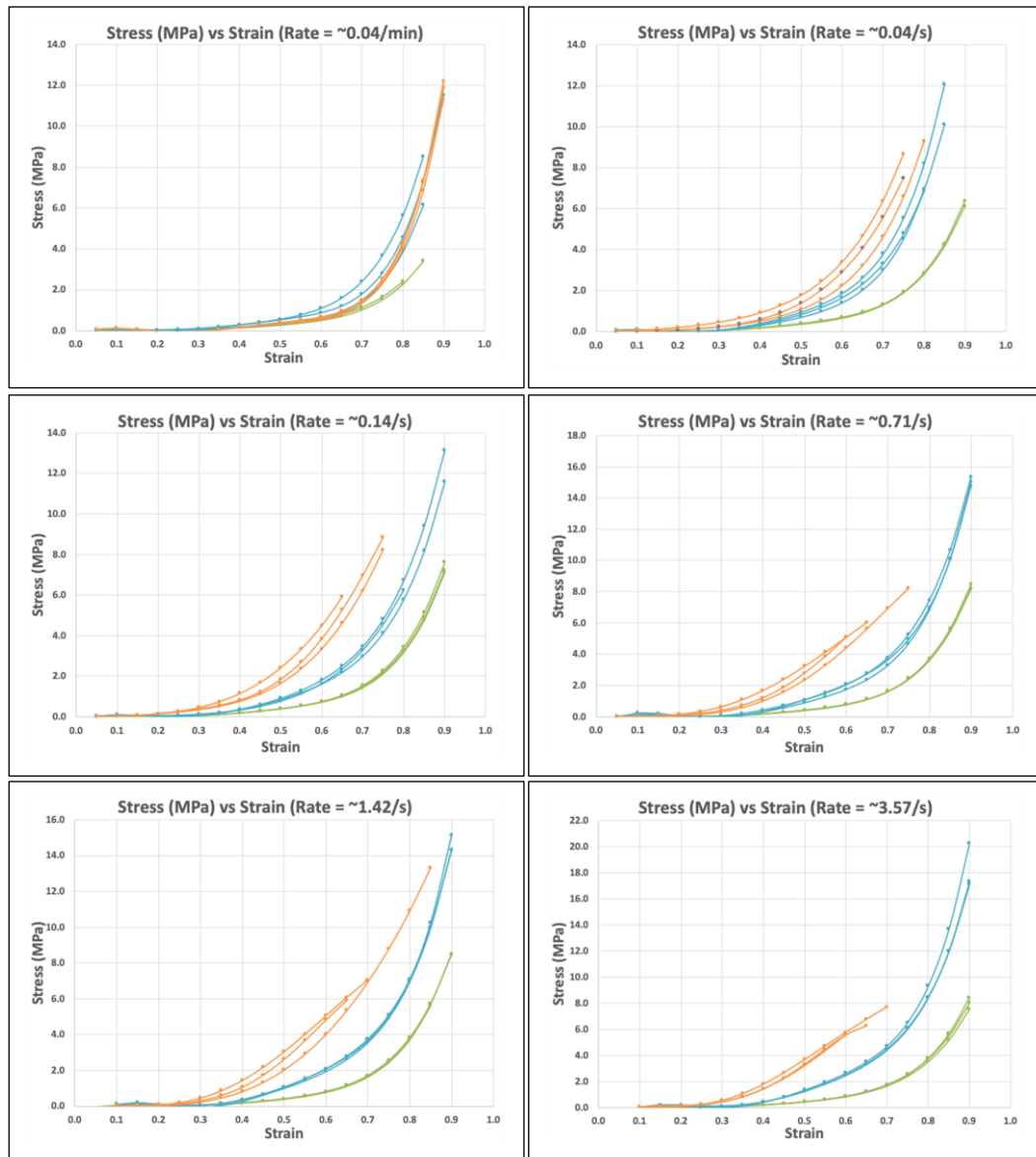
Figure 4-10: Stress-Strain curves for B0, B1 and B2 at the 6 selected strain rates.

The stress-strain compression test results for specimens in B0 (0v%) in green, B1 (0.6v%) in blue and B2 (3.0v%) in orange for the 6 selected strain rates. It illustrates that, apart from very slow strain rate (0.04/min), the strength of each sample of B2 is greater than any sample in B1 and each sample in B1 is greater than any sample in B0.

4.4   Discussion

The objective of this study is to perform a proof-of-concept evaluation on a new IVD prosthesis candidate for an ADR device. We used a model-based approach in this study. We derived an analytical model to model the compressive behavior of such a prosthetic device. From this model, we deduced the requirements of the fibers needed, validated the properties of bamboo fibers that fit this requirement, created the prosthesis specimens, and tested the specimens. This section will discuss three main issues of this study (1) validating the prediction of the model on the fiber content vs compressive strength of the specimens. (2) the accuracy of the model. (3) the suitability of the prosthesis as cervical IVDs ADR devices. For the last point, we use kangaroo C5/C6 IVDs as the animal model from our previous study for the mechanical strength target.

4.4.1   Suitability of the bamboo fiber

Basing on our test results, the procured bamboo fibers had satisfied our model predicted requirements on fiber orientation [Figure 4-1] and fiber length [Table 4-3]. The Young's Modulus of the bamboo fibers [Table 4-2] required for 3v% filled specimen was weaker than required. A more suitable fiber filled content would be 5v% or 10v% as predicted by the model. The 3v% fill was chosen basing on the limitation of our dry packing technique. This was found to be close to the maximum volume of fibers that we could fill the mold with. For future studies, the fibers may be pre-wetted with the 10wt% PVA solution. This will allow specimens of higher fiber filled contents to be made.

As a proof-of-concept study, there are many requirements for bamboo fibers on biomedical application were not included. These will be left for future studies once its usability is established.

4.4.2   Validation on fiber filled content vs compressive strength of prosthesis specimens

The analytical model predicts the compressive strength of prosthesis specimens increases monotonically as the fiber filled content increases. Figure 4-10 provides the compressive stress-strain curves of all the prosthesis specimens in B0, B1 and B2 at the 6 chosen

strain-rates. Apart from the very low strain rate of 0.04/min, it is clear that the compressive stress at any given strain value increases with the fiber content. The hypothesis of if $f_2 > f_1 > f_0$=0 (control) then $S_2 > S_1 > S_0$ (control) has been validated from the experimental results.

The stress-strain curves of all specimens in each batch of the same strain rate are closely packed together. This indicates that the results are repeatable, hence predictable. This characteristic will help in determining the correct fiber content to match the strength of a given IVD required.

4.4.3   Validating the accuracy of the analytical model

From the test results shown in Figure 4-9, the prosthesis specimens are viscoelastic. Since the source of this viscoelasticity is unknown, this property is not currently incorporated within the model. To compare with the analytical model, we took the measured mean stress-strain curve of the B2 specimens as shown in Figure 4-9 and Equation 4-2 to derive the Young's modulus vs strain for the B2 specimens.

The volumetric and area shrinkage of the specimens had presented another problem in this validation. The volumetric shrinkage will result in a higher fiber filled content. With the 37% volumetric shrinkage [Table 4-4], the effective fiber fill content of B2 will become 4.7v%. The effect of the area shrinkage of the specimen on the circumferentially oriented fibers are not known. We postulate that the fiber may be wrinkled up within the specimen. Until they are stretched back to their original state, they cannot share the load with the matrix material. The 21% area shrinkage [Table 4-4] represents a 11.1% shrinkage in the circumference of the specimens. To restore to their original circumference in the mid height of the specimen, a compressive strain of 0.148 [Equation 4-7, α_R=1.124, α_L=0.852] must be applied on the specimen. This may explain the fact that all specimens do not show significant strength before 0.15 strain [Figure 4-10 and Figure 4-9]. To compare with the analytic model, the mean Young's modulus of B2 is pre-strained by 0.15. However, this pre-strain value only represents the unwrinkled state of the fibers in the mid height of the specimen, the fibers in the rest of the specimen will still be in the wrinkled-up state and cannot reinforce the specimen until further

compression. Hence, the measured result should be weaker than the model prediction at lower strain value and approaches that of the model prediction at higher strain value.

Figure 4-11 shows the comparison results between B2 specimens and the model. The blue line is the predicted Young's modulus of a 4.7v% specimen from the model. The solid red line is the mean Young's modulus of the B2 specimens measured [Equation 4-2]. The dotted red line is the Young's modulus of the B2 specimens pre-strained by 0.15. The green line represents the percentage difference of the B2 specimens (pre-strained) from the model prediction (M). It falls form 77% at 0.05 strain to a minimum of 35% at 0.5 strain. This trend agrees with our prediction from our postulation.
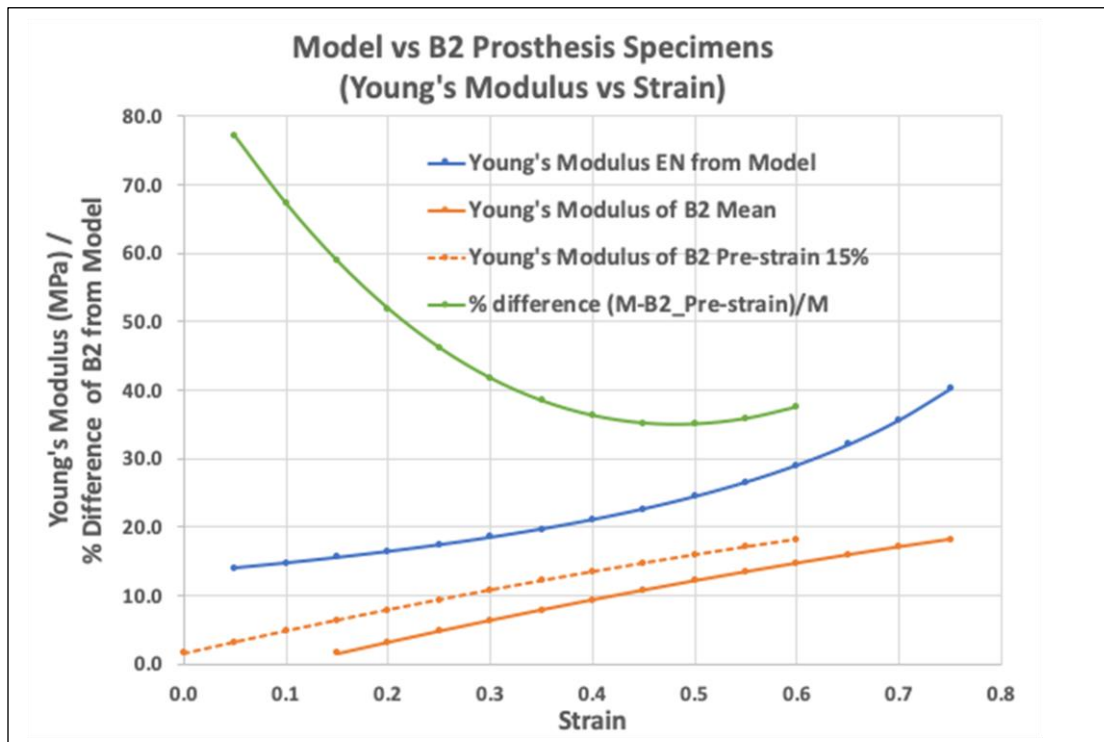
Figure 4-11: Validation of the analytical model using B2 specimens

The blue line represents the model prediction on the performance of a prothesis specimen with 4.7v% fiber fill content. The solid red line is the measured mean performance of all B2 specimens. The dotted red line is the performance of B2 specimens pre-strained by 15%. The green line represents the percentage difference between the model and the pre-strained B2 specimens.

4.4.4   Potential of the specimens as an IVD TDR device material

The key focus of this study is to evaluate if the strength of the material proposed is suitable for IVD prosthesis devices or not. To accomplish this, we compare the strength of the cervical IVD we measured from a previous study using kangaroo C5-C6 IVD as animal model with those of the B2 specimens measured in this study.

In a previous study, we measured the viscoelastic material property of kangaroo C5-C6 IVDs in compressive stress (σ) as a function of both time (t) and strain (ε) at different strain rates (r) up to their yield points. The fitted experimental data (n=19, R^2=0.93) obtained is a 3D surface, which we called the compressive viscoelastic surface. It is given as:

Equation 4-3: Viscoelastic model of kangaroo C5-C6 IVD

$$\sigma(t,\varepsilon) \cong \left[\begin{pmatrix} p_{31} & p_{21} & p_{11} & p_{01} \\ p_{30} & p_{20} & p_{10} & p_{00} \end{pmatrix} \begin{pmatrix} t^3 \\ t^2 \\ t \\ 1 \end{pmatrix}\right]' \begin{pmatrix} \varepsilon \\ 1 \end{pmatrix}$$

Where p_{31}=0, p_{21}=9.287e-05, p_{11}=-0.07037, p_{01}=20.07, p_{30}=-1.739e-08, p_{20}=1.413e-05, p_{10}=-0.003238 and p_{00}=0.1801.

The units of this viscoelastic surface are in MPa for stress and seconds for time. The boundaries of the surface are derived from mean yield points and experimental limitations. They are stress less than 10.88 MPa, strain less than 0.55 and time less than 379s.

To obtain the stress-strain curves for the 6 strain rates (r) [Section 4.2.5] used in this evaluation for kangaroo IVD specimens, one can substitute $t=\varepsilon/r$ into Equation 4-3 and then evaluate the stress values at different strain values (MATLAB).

Figure 4-12 shows the stress-strain curves of kangaroo specimens (KS) (in blue) and B2 specimens (in red) measured at strain rates from 0.04/min to 3.57/s.
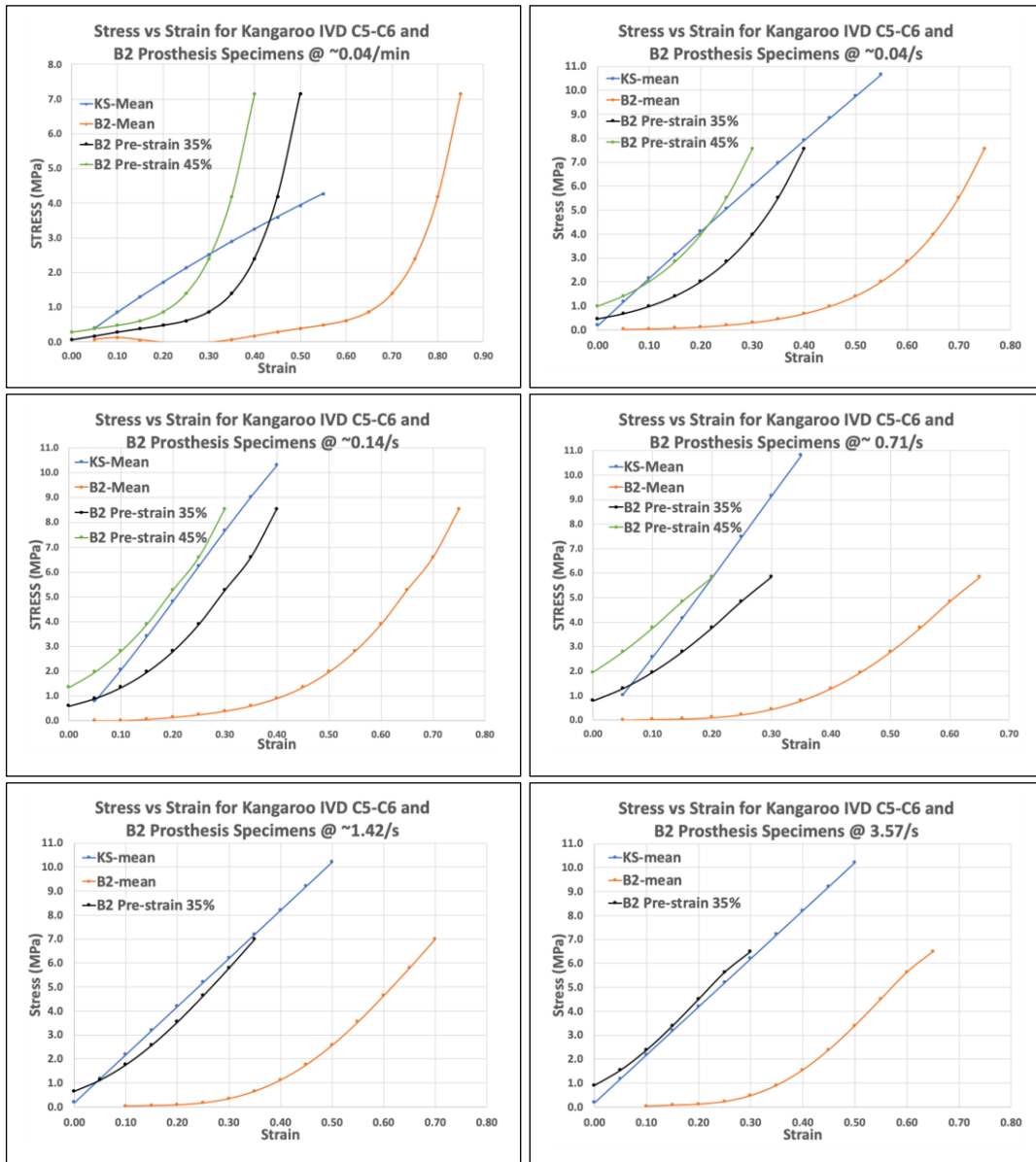
Figure 4-12: Stress-strain curves of pre-strained B2 specimens in matching those of kangaroo IVD C6-C6 specimens (KS)

This figure shows the stress-strain curves of B2 specimens (in red), with 35% pre-strain (in black), 45% pre-strain (in green) and kangaroo C5-C6 IVD specimens (in blue).

It is apparent from Figure 4-12 that the B2 specimens as a raw material is much weaker than that of KS under all strain rate conditions. However, B2 specimens have a high mean yield strain value of 0.76 [Table 4-5]. Taking advantage of this property and with the inspiration from Section 4.4.3, the B2 specimen material can be pre-strained by 35% to 45% to fulfill the required strength of IVD and still leave sufficient physiological operating room for practical IVD prosthesis application. Figure 4-12 also includes the pre-strained properties of B2 specimens with pre-strain values of 35% (in black) and 45% (in green). It is apparent that a pre-strain value of 35% provides a good match of the KS properties under a wide strain-rate values.

4.5   Conclusion

In this study, we have developed a composite material for an IVD prosthesis using 10wt% PVA and bamboo fibers arranged circumferentially. We have developed and validated an analytical model for the compressive behavior of such a prosthesis. We have validated that the strength of the prosthesis can be increase or decrease to match the mechanical properties of an IVD by changing its fiber content and applied a suitable pre-strain value. The prosthesis can be molded into any shape to fit the IVD of individual patient. Its top and bottom surfaces, even though molded flat, will conform perfectly with the vertebral endplates under compression providing even stress distribution over the entire endplates. This may address the reported drawbacks of existing ADR devices. Future development may improve the shrinkage issue of the PVA and develop an anchoring method without the need to machine the vertebral bodies.

4.6 Appendix: Modeling the compressive behavior of an IVD prosthesis

4.6.1 Variables definition
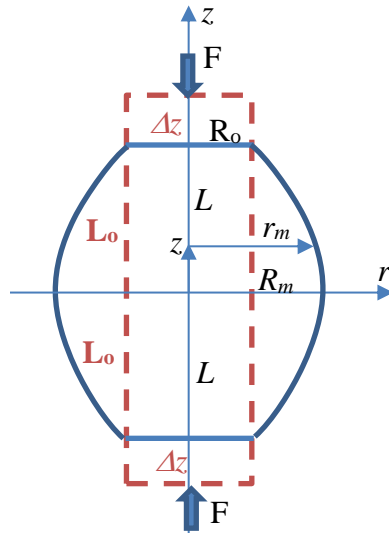
Figure 4-13: Variables used in the analysis.

The original cross-section of the cylindrical specimen (dotted orange rectangle) is compressed into a barrel shaped cross-section.

(For variable definitions see "List of Abbreviations")

4.6.2 Method & Results Summary

In this study, we used a simple short cylindrical form for our IVD prosthesis specimens. The material was made from a composite of 10wt% PVA cryogel with long circumferentially oriented fibers embedded. Under normal compression, the specimen will shorten in height and expand circumferentially forming a barrel shaped object. This will put the circumferentially reinforced fibers under tension, providing compressive strength to the specimen. The goal of this appendix is to derive an analytical model for the compressive behavior of such a composite specimen. The aim is to deduce the selection criterions for the fiber required to satisfy a given IVD strength.

In this derivation the composite material is assumed to be incompressible and linear. The compression process is also assumed to be energy conservative.

In this derivation, basing on the geometry and incompressible material assumption, we first derive the relationship between the normal compression ratio in height (α_L) to the circumferential radius expansion ratio (α_R) at the middle section of the specimen [Equation 4-7]. We then derive the internal energy stored in the barrel body due to the compression [Section 4.6.6.2] and equate this to the work done by the external compressive force [Section 4.6.6.3]. This generates the relationship between the normal compressive Young's modulus E_N of the specimen with its circumferential tensile modulus E_C and a function of the degree of compression α_L [Equation 4-9]. We call this function the compressive function F_C [Equation 4-10] and plot its value against a range of normal compressive strain value in height ε_L ($=1-\alpha_L$). After this, the next step is to derive the composite circumferential tensile modulus E_C from the properties of its components [Section 0]. We take a cylindrical shell of this composite material, cut it open along the length to form a sheet of material. When the specimen expands circumferentially, this sheet of material is under a tensile force. With the circumferential orientation of the long fibers, the fibers within this sheet of material are connected essentially in parallel with the matrix material to withstand the tensile force together. Basing on this approximation, we derive the relationship of the composite circumferential tensile strength E_C to the tensile modulus of its matrix E_m, its fiber E_f and the percentage volumetric fiber content p_f [Equation 4-11]. With equations Equation 4-7 and Equation 4-11 and the tensile strength E_m of the matrix measured, we can derive the tensile strength requirement of the fiber E_f and the percentage fiber content p_f in the composite to suit a given compressive strength E_N of an IVD.

Our study goal is to develop an IVD prosthesis to match the compressive strength of our C5-C6 IVD. We use kangaroo C5-C6 IVDs as our animal model in a previous study [Chapter 3]. Assume the physiological strain on a C5-C6 IVD is approximately 10%. The mean compressive modulus of the kangaroo IVD (n=19) measured is 19.8 MPa (compression rate 0.14/s). At strain value of 10% (α_L=0.9), the value of $F_C \cong 1.5$. This gives $E_N \cong 0.34 * E_C$. With E_N=19.8 MPa, this gives $E_C \cong 59.2$ MPa. The tensile modulus E_m of 10% PVA-C measured in this study was 0.17 MPa (ε=10%, tensile strain rate 0.1/s).

From all these data, the tensile modulus E_f required for fiber with volumetric fill of 0.6%, 3%, 5% and 10% are found to be 9.8 GPa, 2.0 GPa, 1.2 GPa and 5.9 MPa respectively.

4.6.3 Geometric constrain on the compressed object

4.6.3.1 Profile curve of the barrel

Assume the profile is a parabolic curve of the form:

$$r_m = az^2 + bz + c$$

With conditions (z=0, r_m=R_m), (z=L, r_m=R_0) and (z=-L, r_m=R_0), then the profile curve becomes:

Equation 4-4: Profile curve equation of compressed specimen

$$r_m = R_m - \frac{R_m - R_o}{L^2} z^2$$

4.6.4 Volume of the barrel

Take a slice of thickness dz, at a distance z, the volume of the slice:

$$dv = \pi r_m^2 dz$$

Hence the volume V of the barrel:

Equation 4-5: Volume of compressed specimen

$$V = \int_{-L}^{L} \pi r_m^2 \, dz = \pi \int_{-L}^{L} \left(R_m - \frac{R_m - R_o}{L^2} z^2 \right)^2 dz = \frac{2\pi L}{15} (8R_m^2 + 4R_m R_o + 3R_o^2)$$

4.6.5 Compression of a cylinder of incompressible material

When a cylindrical object is deformed into a barrel shape under a pair of compressive force applied from top and bottom, assuming the material is incompressible, the volume of the cylinder should be the same as the barrel.

$$\pi R_o^2 2L_o = \frac{2\pi L}{15}(8R_m^2 + 4R_m R_o + 3R_o^2)$$

Solving for R_m and taking only the positive root:

Equation 4-6: Equation for R_m

$$R_m = \frac{R_o}{4}\left[-1 + \sqrt{5\left(\frac{6L_o}{L} - 1\right)}\right]$$

Substitute $\alpha_L = \frac{L}{L_o}$ and $\alpha_R = \frac{R_m}{R_o}$ into Equation 4-6:

Equation 4-7: Compressive ratio of circumference in terms of height ratio

$$\alpha_R = \frac{1}{4}\left[\sqrt{5\left(\frac{6}{\alpha_L} - 1\right)} - 1\right]$$

4.6.6   Deriving the compressive modulus E_N from E_C

4.6.6.1   Energy stored in a cross-sectional slice

Take a thin circular cross-sectional slice of thickness dz at a distance z from the center of the barrel. Then the radius of the slice is r_m.

Consider a ring at a distance r from the center and thickness dr, then the length of this circular element will be: $2\pi r$
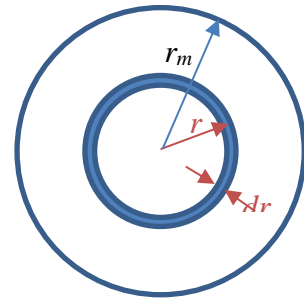
Since the original radius of the slice before compression should be R_o and now with the compression, the radius of the slice becomes r_m, hence assuming uniform expansion, then the original radius of the ring will be:

$$r_{o,r} = \frac{R_o}{r_m}r$$

The elongation of this ring is:

$$\Delta\ell = 2\pi r - 2\pi r_{o,r} = 2\pi r - 2\pi \frac{R_o}{r_m} r = 2\pi r \left(1 - \frac{R_o}{r_m}\right) = 2\pi \left(\frac{r_m - R_o}{r_m}\right) r$$

The circumferential strain of this ring due to compression of the cylinder is:

$$\varepsilon_{r,c} = \frac{2\pi r - 2\pi r_{o,r}}{2\pi r_{o,r}} = \frac{r - \dfrac{R_o}{r_m} r}{\dfrac{R_o}{r_m} r} = \frac{r_m - R_o}{R_o}$$

Note: the circumferential strain is independent of r.

If the circumferential Young's Modulus is E_c, then the circumferential tensile stress:

$$\sigma_{r,c} = E_c \varepsilon_{r,c} = E_c \frac{r_m - R_o}{R_o}$$

Note: the circumferential tensile stress, $\sigma_{r,c}$, is also independent on the radius r.

The tensile force acting on the surface of this $drdz$ element is: $f_{r,c} = \sigma_{r,c} dz dr$.

Hence the energy (or work done on) stored in the elongation of this element:

$$de = f_{r,c}\Delta\ell = E_c \frac{r_m - R_o}{R_o} dz dr 2\pi \left(\frac{r_m - R_o}{r_m}\right) r = 2\pi E_c \frac{(r_m - R_o)^2}{r_m R_o} dz\, rdr$$

The total energy stored by the slice at distance z:

$$e_z = \int_0^{r_m} 2\pi E_c \frac{(r_m - R_o)^2}{r_m R_o} dz\, rdr = \pi E_c (r_m - R_o)^2 \frac{r_m}{R_o} dz$$

4.6.6.2 Energy stored in a compressed cylinder

Total energy stored in the barrel as a result of compressing the cylinder:

Equation 4-8: Energy stored in the compressed specimen

$$e_{2L} = \int_{-L}^{L} \pi E_c (r_m - R_o)^2 \frac{r_m}{R_o} dz = \frac{\pi E_c}{R_o} \int_{-L}^{L} (r_m^3 - 2R_o r_m^2 + R_o^2 r_m) dz$$

Substituting Equation 4-4 into Equation 4-8 and solving the integral:

$$e_{2L} = \frac{16\pi E_c L}{35 R_o}(R_m - R_o)^2 \left(2R_m + \tfrac{1}{3}R_o\right)$$

4.6.6.3 Work done by external force on the cylinder

$$e_N = F_N 2\Delta z_o = \sigma_N \pi R_o^2 2(L_o - L) = E_N \varepsilon_N 2\pi R_o^2 (L_o - L) = E_N 2\pi R_o^2 \frac{(L_o - L)^2}{L_o}$$

4.6.6.4 Deriving equivalent normal Young's modulus E_N

Assuming energy conservation, the work done provided by the external normal stress will be mainly stored in the deformed cylinder (barrel shape). Hence, $e_N = e_{2L}$, giving

$$E_N 2\pi R_o^2 \frac{(L_o - L)^2}{L_o} = \frac{16\pi E_c L}{35 R_o}(R_m - R_o)^2 \left(2R_m + \tfrac{1}{3}R_o\right)$$

Solving for E_N,

$$E_N = \frac{8}{35} \times \frac{L_o L}{(L_o - L)^2} \times \frac{(R_m - R_o)^2 \left(2R_m + \tfrac{1}{3}R_o\right)}{R_o^3} E_c$$

Substituting $\alpha_L = \frac{L}{L_o}$ and $\alpha_R = \frac{R_m}{R_o}$ into above equation, giving

Equation 4-9: Normal compressive Young's modulus of specimen

$$E_N = \frac{8}{35} \times \frac{\alpha_L}{(1 - \alpha_L)^2} \times (\alpha_R - 1)^2 \left(2\alpha_R + \tfrac{1}{3}\right) E_c$$

As α_R is a function of α_L [Equation 4-7], Equation 4-9 provides the relationship of the effective compressive Young's modulus E_N to the circumferential Young's modulus E_C and the compressive strain ($\varepsilon_N = 1 - \alpha_L$) value.

4.6.6.5 Compressive function

Defining a compressive function $F_C(\alpha_L)$:

Equation 4-10: Compressive function F$_c$

$$F_c(\alpha_L) = \frac{\alpha_L}{(1 - \alpha_L)^2} \times (\alpha_R - 1)^2 \left(2\alpha_R + \frac{1}{3}\right)$$

The value of $F_C(\alpha_L)$ is a function of the degree of compression α_L. Figure 4-14 plots the value of this compressive function at different strain value.
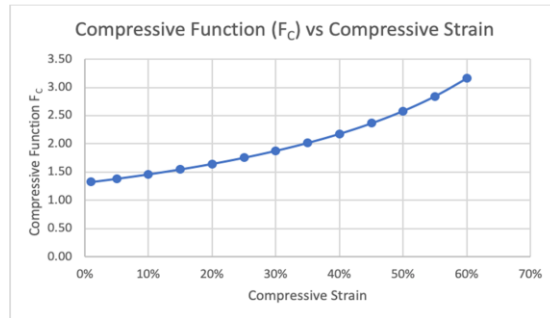
Figure 4-14: The compressive function Fc vs compressive strain (ε_N=1-α_L) value.

4.6.7 Model of composite property with circumferential fiber reinforcement

Assuming the embedded fibers in the cylinder are long (wound over more than one circle) and oriented roughly circumferentially in a horizontal position. Take a circular slice from the cylinder and cut it open. Assuming the majority of the fibers are in a horizontal position [Note 1], when the slice is subjected to a tensile force, the matrix material and the fibers are effectively connected in a parallel condition.
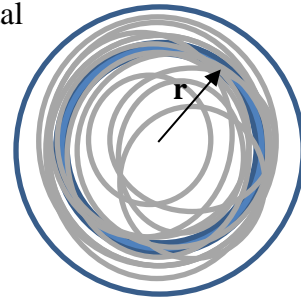
Then,

$$F_C = F_f + F_m$$

$$E_C \varepsilon (A_f + A_m) = E_f \varepsilon A_f + E_m \varepsilon A_m$$
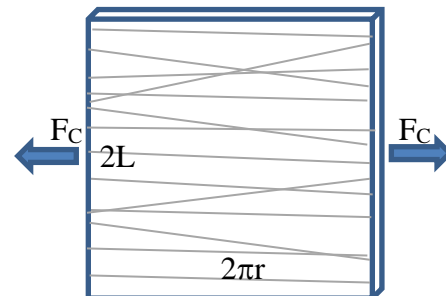
$$E_C = \frac{A_f}{(A_f + A_m)}E_f + \frac{A_m}{(A_f + A_m)}E_m$$

Since ($p_f = 1 - p_m$), giving:

Equation 4-11: Circumferential tensile modulus of specimen in terms of volumetric fiber content, tensile modulus of fiber and tensile modulus of matrix.

$$E_C = p_f E_f + (1 - p_f)E_m$$

Note 1:

If the fiber is making an angle θ to the horizontal, the horizontal tensile force from the fiber will be $F_f \cos\theta$. The maximum angle that can be made will be one in a diagonal position. In our case, the mold diameter is 23mm and height 8.7mm [Section 4.2.3]. The maximum angle will be $\tan^{-1}\frac{8.7}{23*\pi} = 6.7^o$. Since most of the fibers are packed down in the mold. The actual inclination angle in one circumferential length will be much less than 6.7°. The cos of this small angle can be approximately equal to 1.

4.7 Appendix: Tensile properties of 10wt% PVA

The analytical model requires the tensile properties of 10%PVA. To complete the assessment of the model, its measurement was included as a side study.

4.7.1 Material and Methods

An approximate 5"x5"x 2mm thick sheet of 10wt%PVA after 6 FTCs was prepared in same manner as described in Section 4.2.3. Samples were cut from the center portion of the sheet using parallel blades 5 mm apart and 3 cm long. 8 specimens with thickness and width measured were tensile tested using an Instron 8870 machine with a Transducer Techniques 1000 g load cell at a displacement rate of 1mm/s to 0.8 strain value.

The stress-strain values were derived for the 8 specimens. The mean stress-strain curve for the 8 specimens were extracted and the Young's modulus at 10% strain was derived (Excel).

4.7.2   Tensile Young's modulus for 10wt% PVA

The analytical prosthesis compressive model requires the tensile Young's modulus for the matrix material (i.e. 10wt% PVA). Figure 4-15 provides the test result for 8 specimens of pure 10wt% PVA after 6 FTCs. It provides the mean stress-strain curve and the extend (max and min) of the stress value at each strain value. The fitted stress-strain curve provides the following equation:

Equation 4-12: Mean tensile stress vs strain for 10wt% PVA

$$\sigma = 0.1268\, \varepsilon^2 + 0.1418\, \varepsilon - 0.0002$$

Equation 4-12 provides the tensile Young's modulus of 10wt% PVA to be 0.167 MPa at 0.1 strain and at a tensile strain rate of ~0.1/s.
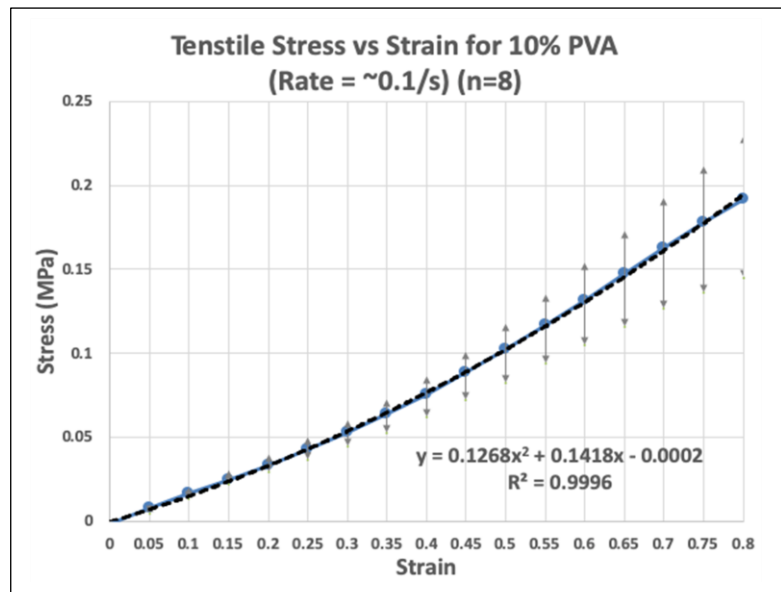
Figure 4-15: Tensile properties for 10wt% PVA

Chapter 5

5   IVD Prosthesis Development - Torsion

<u>Abstract</u>

An unrestricted IVD, as illustrated with kangaroo specimens, has shown substantial torsional strength and viscoelasticity. Even though the importance of torsional behavior of IVD is still under debate due to their limited ROM, some researches had shown that even low torsional motion below the yield limit can damage the IVD. The compressive properties of the prosthesis material proposed was fully accessed in previous Chapter 4. In this Chapter, its torsional properties are evaluated. Torsional specimens were created by gluing the composite specimen with aligned top and bottom aluminum plates and tested in specially designed jigs and a dual axis material tester. The torsional stress and torsional strain are calculated based on the definitions used for the kangaroo specimens. Three batches, B3, B4 and B5 of 27 specimens each containing fiber contents of 0v%, 0.6v% and 3.0v% respectively were used in the torsional tests. 9 strain-rates (0.03/min to 4.66/s) were used to measure the torsional stress vs strain behaviors of the specimens in each batch. The results were compared to those of kangaroo specimens. Unfortunately, the torsional strength (< 1 MPa) of specimens with fibers (B4 & B5) show indistinguishable value from those of the pure PVA specimens (B3) and much weaker than those of kangaroo specimens (mean yield stress = 13.31 MPa). The hypothesis of monotonous increase of torsional strength with increase of fiber content has not been validated. The material has a complex torsional stress vs strain-rate relationship. The weak torsional stress property may be attributed to the fibers wrinkled up caused by the PVA shrinkage due to the cryogel process. Even though it has only weak torsional strength, it is found that the material can sustain a high torsional strain value (>2.5) without yield. Compared the yield torsional strain of 0.66 obtained from the kangaroo specimens, it can provide more than adequate capability for IVD prosthesis application. Combining the compressive and torsional properties, the material proposed can functionally equivalent to the class of FDA approved IVDs such as ProDisc-C and Prestige ST. In addition, it provides extensive mobile-core rotational kinematics, important for cervical disc arthroplasty[24], not supported by these protheses.

5.1 Introduction

As the only non-rigid components of our spine, all spinal mobilities (flexion, extension and rotation) are provided mainly through our IVDs. They also provide shock absorptions in all directions to protect our brain from harm in a traumatic incident. In this study, we limit our study to cranial compression and torsion only. As shown in Section 3.4.3 and 3.4.4 using kangaroo IVD C5-C6 as our animal model, we have validated that the unrestricted IVDs [Section 3.1] have both compressive and torsional viscoelastic properties and shock absorption capabilities in both cases.

Even though the importance of torsional behavior of IVD is still under debate due to their limited ROM, some researches had shown that even low torsional motion below the yield limit can damage the IVD[72–74]. Hence it is important to characterize the torsional behavior of an IVD prosthesis to compare that with a human IVD. Despite the importance of torsional resistance and we had validated its substantial value in unrestricted kangaroo IVDs [Table 3-4], not all existing FDA(US) and CE(EU) approved IVD prostheses provide this capability. For example, ProDisc[95], SB Charite[96] and Prestige ST[12,94] will have questionable torsional resistance because of their design while Bryan [Section 2.1Figure 2-1], M6-C[15,91][Section 2.2] and CP-ESP[16,92][Section 2.5] have this capability specially incorporate in their structure. In the absence of this capability of an IVD prosthesis, the torsional resistance must be offloaded to surrounding discoligamentous structures in the spine. This may increase their operating stress level.

In Chapter 3we have introduced the concept of a possible IVD prosthesis material candidate using a composite of 10wt% PVA cryogel with long circumferentially oriented bamboo fibers and have studied its compressive properties. This Chapter is devoted to evaluating the torsional characteristics of the specimens prepared using the same materials and methods as described in the compression case [Section 4.2.3].

Similar to the case in compression, the experiment goal is to valid the hypothesis that the torsional strength will increase monotonically with increasing fiber content. Using three batches of specimens, B3, B4 and B5, of fiber volumetric content f and torsional strength S, we will try to validate experimentally the hypothesis that if $f_5 > f_4 > f_3 = 0$ (control), then

$S_5 > S_4 > S_3$. Unfortunately, unlike in the compression case, no analytic model was developed for the torsion case. The three fiber contents chosen remains the same as in the compression test, i.e., 0v%(control), 0.6v% and 3.0v% for B3, B4 and B5 respectively.

To validate this hypothesis, all strain rates given in Table 5-1 are used. Stress-strain curves were taken from the experimental results of each batch for each strain rate. Comparisons of the strength of the three batches are made basing on their stress-strain curves of the approximate same strain rate.

To validate the suitability of the specimen as a candidate for IVD prosthesis, the maximum torsional stress obtained from all stress-strain curves of all specimens was compared with the mean yield torsional stress of the kangaroo C5-C6 specimens.

5.2   Materials and Methods

5.2.1   The design of the prosthesis specimens

The specimens prepared for the compressive tests alone were inadequate for torsional testing because it is difficult to transmit the torque onto the specimens without slippage. To overcome this problem, two square aluminum plates were glued to the top and bottom of the specimen surfaces [Figure 5-1B]. The torque was applied to the top aluminum plate with the bottom one held stationary [Figure 5-3B]. The thickness of the top and bottom aluminum plates was eliminated in the specimen height calculation. Care had been taken to ensure the proper alignment of the top and bottom plates and the center of the specimen body (axis of rotation). In addition, the top surface of each specimen was carefully preserved from the PVA mold to the gluing process, so that the torque applied is always in the same direction of the fiber orientation. Special tools had been designed for aiding the gluing process [Figure 5-1] and specimens testing [Figure 5-3]. The torsional analysis method is as described in Section 3.3.2.
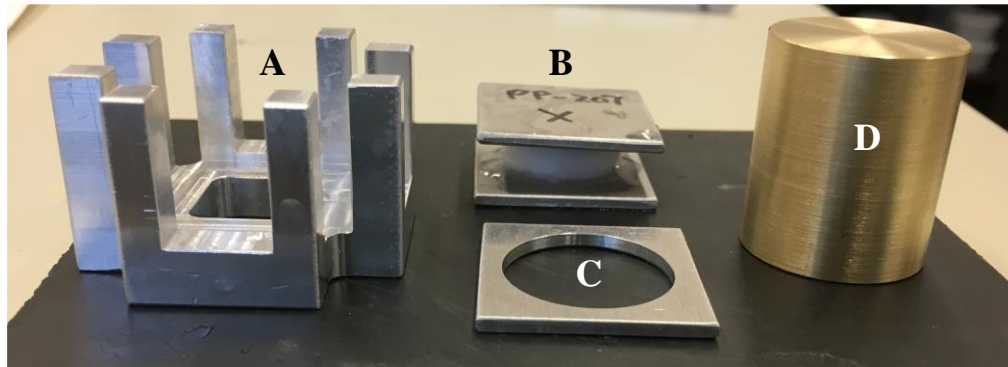
Figure 5-1: Torsional specimen gluing tools

A: gluing jig for aligning the top and bottom aluminum plates onto the specimen body during the gluing process.

B: torsional test specimen showing its specimen ID and top surface orientation.

C: centering template for aligning the axis of rotation of the specimen body and its top and bottom aluminum plates.

D: brass weight to provide consistent pressure onto the specimen during the glue hardening process.
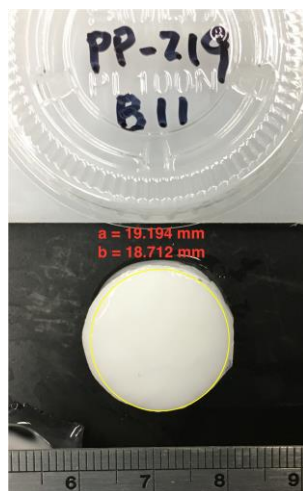
Figure 5-2: Determining the major axis (a) and minor axis (b) of the ellipse using a scaled photo in ImageJ software.
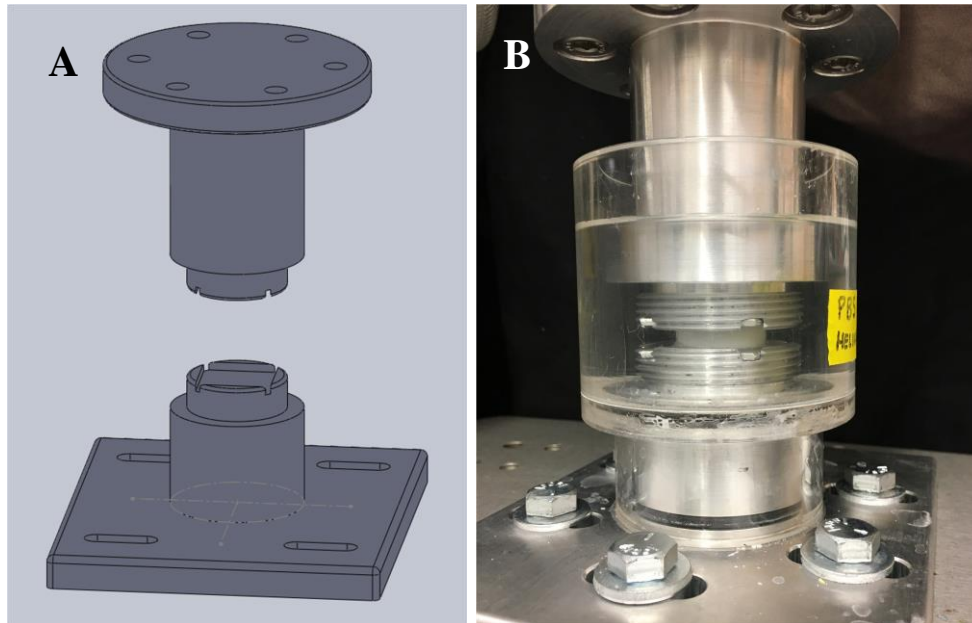
Figure 5-3: Torsional test fixtures

A: The design of the testing fixtures. The bottom cylindrical holder contains a square pocket machined into the top surface to house the bottom aluminum plate of the test specimen. Same arrangement is provided for the top holder.

B: The complete test assembly. The test specimen is fully immersed in 1x PBS solution and the top and bottom aluminum plates are inserted tightly into the pockets of the test fixtures.

5.2.2 Prosthesis specimen preparation

Three batches (B3, B4 and B5) of 50 samples each were made using same process and materials as described in the compressive case (Section 4.2.3) containing fibers of mean weight 0g (control, $f_3=0v\%$), 36.6mg (SD 0.4) ($f_4 \approx 0.6v\%$) and 173.6mg (SD 0.4) ($f_5 \approx 3v\%$) respectively. After removing defective ones via visual inspection, the resulting number of specimens in B3, B4 and B5 was 27, 27 and 36 respectively.

Basing on the knowledge that there is shrinkage of the specimen from the mold after the freeze-thaw process [Table 4-4] and no proof of uniform shrinkage in any two orthogonal

directions, the cross-section of the specimen was approximated by an ellipse instead of a circle.

To determine the polar moment of inertia J of the specimen [Section 3.3.2], each specimen was individually identified. Its top surface was fitted with an ellipse and its major and minor axis measured using scale photo technique (iPhone 6S, 6" steel ruler, ImageJ) [Figure 5-2]. Same was performed for the bottom surface. The major (*a*) and minor axis (*b*) of the specimen were taken as the corresponding mean values of its top and bottom surfaces. The cross-sectional area of the specimen was calculated to determine its shrinkage from the mold.

300 aluminum plates (28mm square, 2mm thick) were machine-cut to precise dimensions, bead-blasted to roughen both surfaces and detergent-washed to remove possible surface greases. These arrangements were to ensure good adhesion surfaces for the PVA composite specimen body. The adhesive used was a high viscosity cyanoacrylate adhesive (Sigma-Aldrich, PCode 1002603306) to limit the penetration of the adhesive into the PVA body.

The specimens were constantly immersed in 1x PBS solution (Fisher Scientific CAS 7647-14-5,7447-40-7) throughout the preparation process except the shot duration during gluing (~60 second). Afterwards they were stored in 1x PBS solution at room temperature until testing.

5.2.3   Torsional testing

5.2.3.1   Test machine setup

All specimens were tested on an Instron 8874 dual axis machine with a load cell model 49139 ($\pm$10kN/100Nm) and our special test fixture installed together with a 1xPBS bath [Figure 5-3B]. The top and bottom cylindrical specimen holders were properly aligned by adjusting the position of the bottom holder. The top and bottom square pockets were aligned by rotating the top holder via the Instron upper arm.

To measure the height of the specimens with the thickness of the top and bottom plates eliminated, an eraser of known height (61.10 mm) was placed in between two spare aluminum plates inserted in the upper and lower pockets of the fixture. The upper arm of the tester was lowered until a load of 1N was registered. With the known height of the eraser and the measured distance of the Instron upper arm, the height of each specimen body, without the top and bottom aluminum plates, could be derived.

5.2.3.2   Torsion test

The position of the top and bottom square pockets of the fixture were properly aligned before any specimen was inserted into the pockets.

The positive direction of rotation was determined using the right-hand screw rule with the thumb pointing up.

Each specimen was first subjected to a pre-conditioning step. The purpose was to reduce the internal stresses built-up during the FTCs of the PVA process. The initial height of the sample was determined by lowering the upper machine arm until a 1N force was registered. It was then slowly compressed by 1 mm at a rate of 0.25mm/min. The position was held for 1 minute and then subjected to a sinusoidal oscillation at 0.1Hz, amplitude $\pm 2^o$ for 90 cycles (15 minutes). Load was removed for 2 minutes to allow the sample to relax before the main torsion test.

The height of each sample prior to the torsion test was again measured by lowering the upper machine arm until a 1N force was registered. Each sample was then compressed by 1 mm at 0.25mm/min and hold position for 1 min. Using the rotation rates given in Table 5-1, it was first rotated to -15° and then to $+90^o$. Table 5-1 also shows the number of samples in each batch using the same rotation rate.

Table 5-1: Rotation rates and the number of specimens involved

Rotation rates	Strain rate[*]	B3 (f_3=0v%)	B4 ($f_4 \approx$0.6v%)	B5 ($f_5 \approx$3.0v%)

1º /min	0.03/min	3	3	3
7º /min	0.18/min	3	3	3
11º /s	0.28/s	3	3	3
23º /s	0.60/s	3	3	3
45º /s	1.17/s	3	3	3
68º /s	1.76/s	3	3	3
90º /s	2.33/s	3	3	3
135º /s	3.50/s	3	3	3
180º /s	4.66/s	3	3	3
	Total	27	27	27

*The strain rate is calculated from the mean geometric properties of the prosthesis specimens [Table 5-2].

5.2.4   Test results extraction

Figure 5-4 shows the test data of a typical specimen. Except for those tests using very low rotation rates, there are short durations of vibrations at each start and stop motion [Figure 5-4B]. To avoid these vibrations, the specimen is first rotated in the negative direction slightly (-15º) before rotating in the positive direction to the final position (+90º). The captured torque and rotation values were converted to torsional stress and torsional strain according to the methods described in Section 3.3.2 and the measured geometry of the specimen. Only the data in the positive strain and positive stress region are considered [Figure 5-5]. Two equations were extracted (MS Excel) from the test data:

(1) the strain vs time equation and (2) the stress vs strain equation. Because of a constant rotation rate used, equation (1) is a linear equation. Equation (2) is a polynomial of degree n <=4 [Figure 5-5B]. The initial time t1 of equation (1) and the end strain value $\varepsilon 2$ (end of elastic region or yield) of equation (2) are taken. From equation (1) the start strain value $\varepsilon 1$ and the end time t2 are derived. The t1, t2, $\varepsilon 1$ and $\varepsilon 2$ specify the valid range of the experimental data for this specimen.
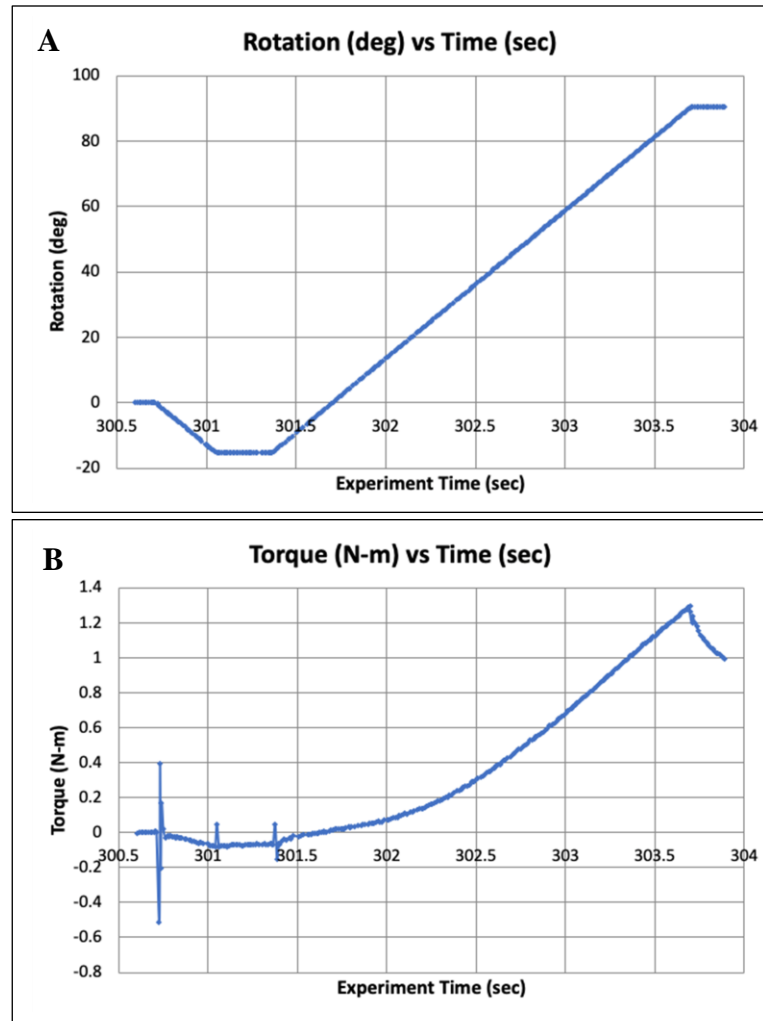
Figure 5-4: Typical torsional test curves

A: the driving function: rotation vs time. The specimen is first rotated to -15º, stop and then rotate to +90º. The stop was introduced by the Instron controller.

B: the measured torque vs time showing transient vibrations in the measured torque when the rotation starts, stops and changing direction.
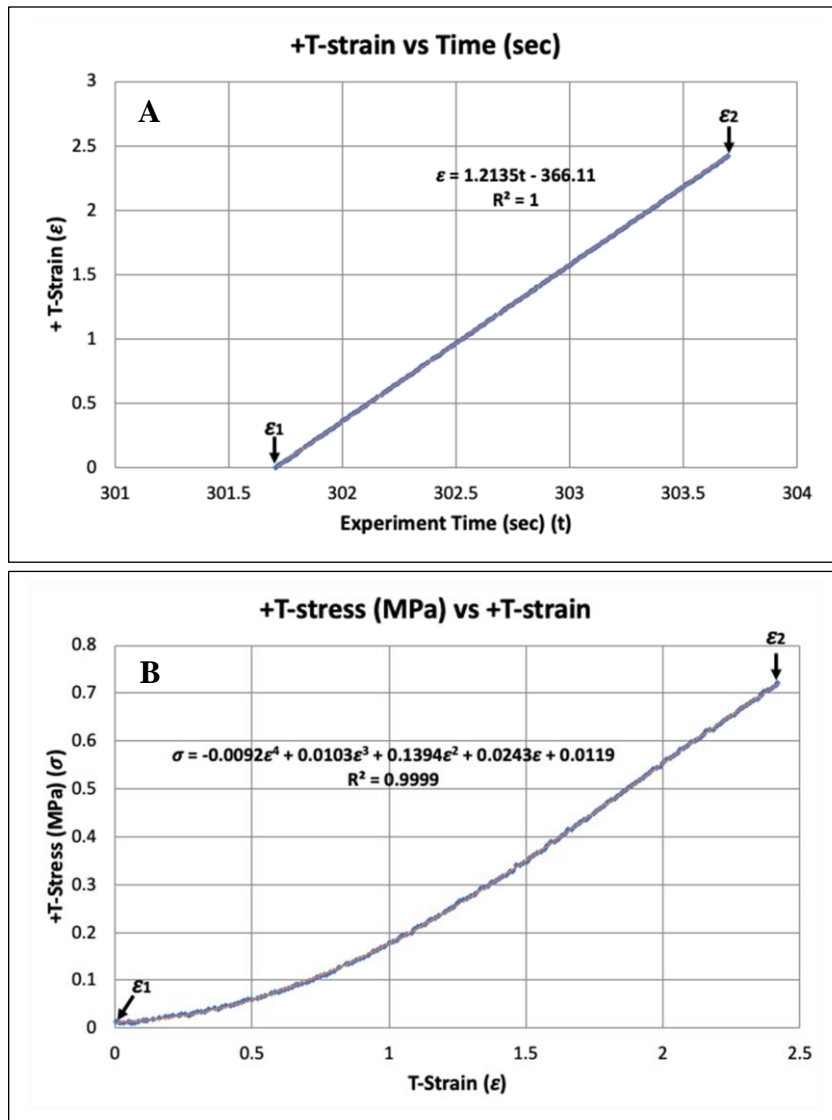
Figure 5-5: Specimen test results processing

Basing on the geometry of the specimen, its torsional stress vs strain curve (B) was extracted from the experiment data. The stress/strain curve extracted covers only the positive range of the stress and strain value. The start (ε1) and end strain (ε2) values were identified for each specimen to indicate the valid range of the fitted stress/strain curve. The time curve (A) provides the actual strain rate the specimen was tested in.

5.3   Results & Analysis

5.3.1   Geometric properties

As shown in Figure 4-3, the specimens had considerable shrinkage after the 6 FTCs.
Table 5-2 shows the measured geometric properties of the specimens used for torsional
testing. The shrinkage is calculated basing on the dimension of the mold with 23 mm
diameter and 8.7 mm height.

Table 5-2: Geometric properties of prosthesis specimens (n=81)

Properties	Mean	SD	Min	Max	Unit	Mold	Shrinkage
Major axis a	20.2	0.8	18.8	21.6	mm	23.0	12%
Minor axis b	19.8	0.7	18.4	21.0	mm	23.0	14%
Area	314.5	23.5	272.2	353.1	mm^2	415.5	24%
Height	6.74	0.7	4.9	7.7	mm	8.7	22%
Volume	2119.2	241.9	1355.1	2511.0	mm^3	3614.6	41%

5.3.2   Torsional properties

5.3.2.1   Torsional strength comparison between B3, B4 and B5

For the torsional test, none of the specimens had yield under the maximum torsional
strain condition applied and all of the aluminum plates remain attached to the specimen
body, indicating that the glue chosen was effective.

The three batches of specimens were tested using rotation rates described in Section
5.2.3.2 and the test results extracted as described in Section 5.2.4 are shown in Figure
5-6.
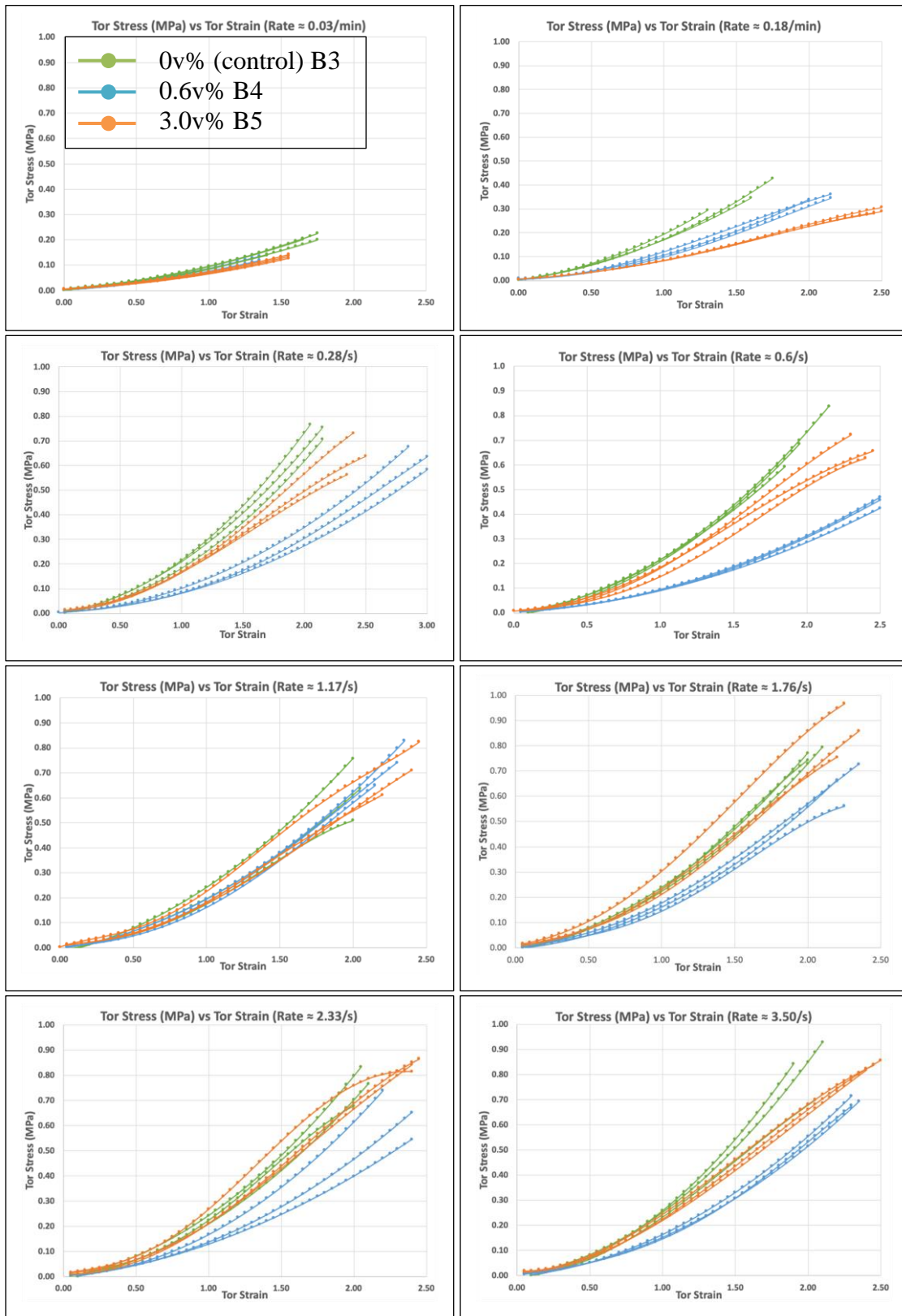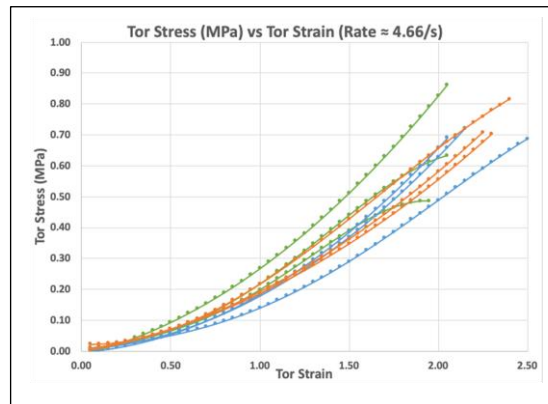
Figure 5-6: Torsional test results for specimens in B3, B4 and B5

Shows the torsional test results of all specimens in batch B3 (0v%), B4 (0.6v%) and B5 (3.0v%) with the 9 strain rates given in Table 5-1. For the test results of strain rate ≈ 0.03/min, the test result of the B4 specimens were hidden behind those of the B5 specimens.

The torsional test results for the specimens in B3, B4 and B5 are shown in Figure 5-6. The stress/strain curves of the specimens at different strain rate in each batch were generally closely bundled together, indicating that the results are probably reproducible. It is also seen that the specimens had much weaker peak torsional strength (<1 MPa) as compared with the mean torsional yield strength of 13.31 MPa measured from kangaroo specimens (Table 3-4). However, all specimens in B3, B4 and B5 can withstand much higher strain (around 2.5 to 3) without yield than those of kangaroo (mean yield strain = 0.66, Table 3-4). There is no clear trend in comparing the strength between specimens at different torsional strain rates in the three batches of different fiber contents. Hence the hypothesis of monotonous torsional strength increases with increase of fiber contents [Section 5.1] has not been validated.

5.3.2.2   Torsional viscoelastic behavior analysis

Viscoelasticity is the effect of strain rate on stress. Figure 5-6 has indicated that the specimens had a complex torsional stress vs torsional strain rate relationship. Figure 5-7

provides a better illustration on this relationship using the mean stress value vs strain for specimens tested within the same strain rate and compare that between specimens in B5 and B3(control). Even though plot A and C show some aspect of this relationship, plot B and D illustrate this relationship better. For specimens in B5, at each strain level, plot B shows the stress value increases from very low value to a dominant peak around strain-rate =1.76/s and then decreases. For specimens in B3 (control), at each strain level, plot D shows a few weak peaks for stress vs strain rate. A weak peak also appears at strain-rate = 1.76/s as in plot B, but a more dominate peak obtained at 3.5/s. In both B5 and B3, there are no monotonous increase relationship between torsional stress vs torsional strain-rate, however, torsional stress increases monotonously with increasing strain.
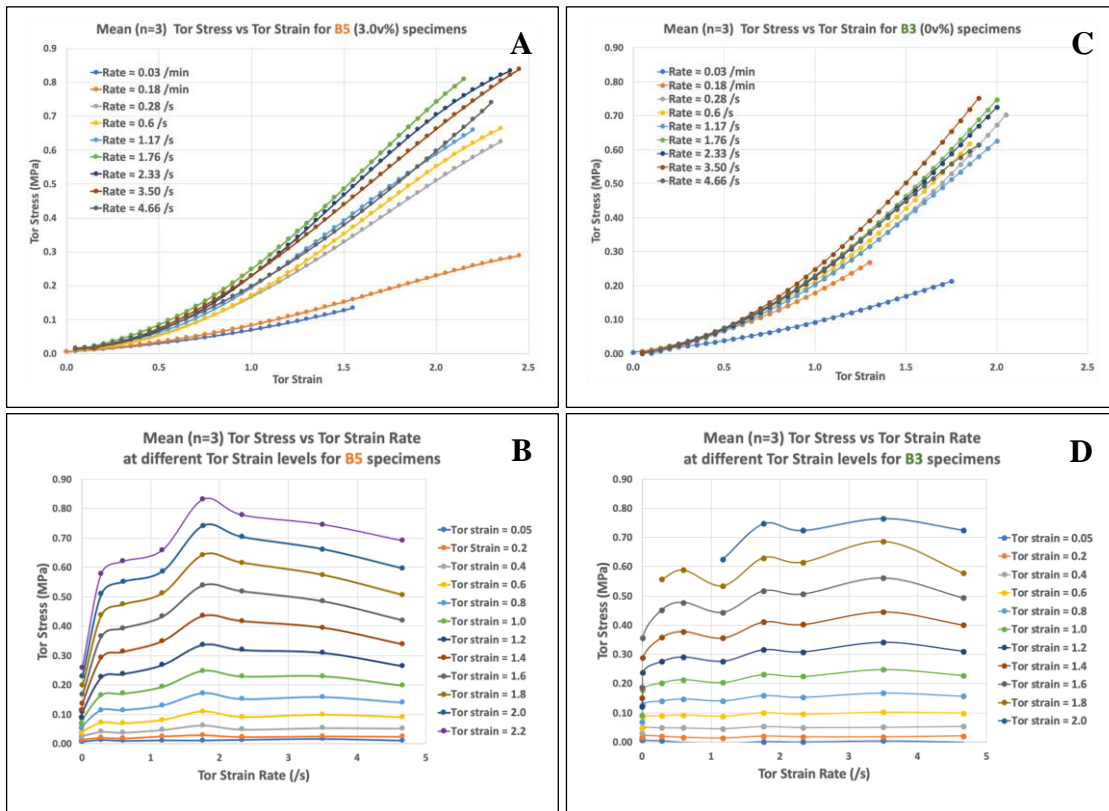
Figure 5-7: Mean torsional stress vs torsional strain at different torsional strain rates for B5 & B3 specimens

A & C: Mean (n=3) torsional stress vs strain curves at different strain rate. A is for specimens in B5 and C is for specimens in B3 (control)

B & D: Mean (n=3) torsional stress vs strain-rate at given strain level. B is for specimens in B5 and D is for specimens in B3 (control)

The torsional viscoelasticity can also be modelled using the viscoelasticity surfaces method (stress vs time & strain) as illustrated in the kangaroo case (Figure 3-10). Figure 5-8 provides the surfaces of a low time order fit (P_{12}) and a high time order fit (P_{52}) on the test results of specimens in B5 and B3. The coefficients (p_{ij}) of the polynomials P_{12} and P_{52} of both B5 and B3 are provided in Table 5-3.

However, it is found that, even though with acceptable R^2 fit values, both lower and higher order surface fits, P_{mn} (Matlab limits m & n <=5), do not show the stress vs strain-rate behavior as clear as that in Figure 5-7 plot B & D.

	B5	B3
P_{12}	R^2=0.983	R^2=0.986
P_{52}	R^2=0.986	R^2=0.987
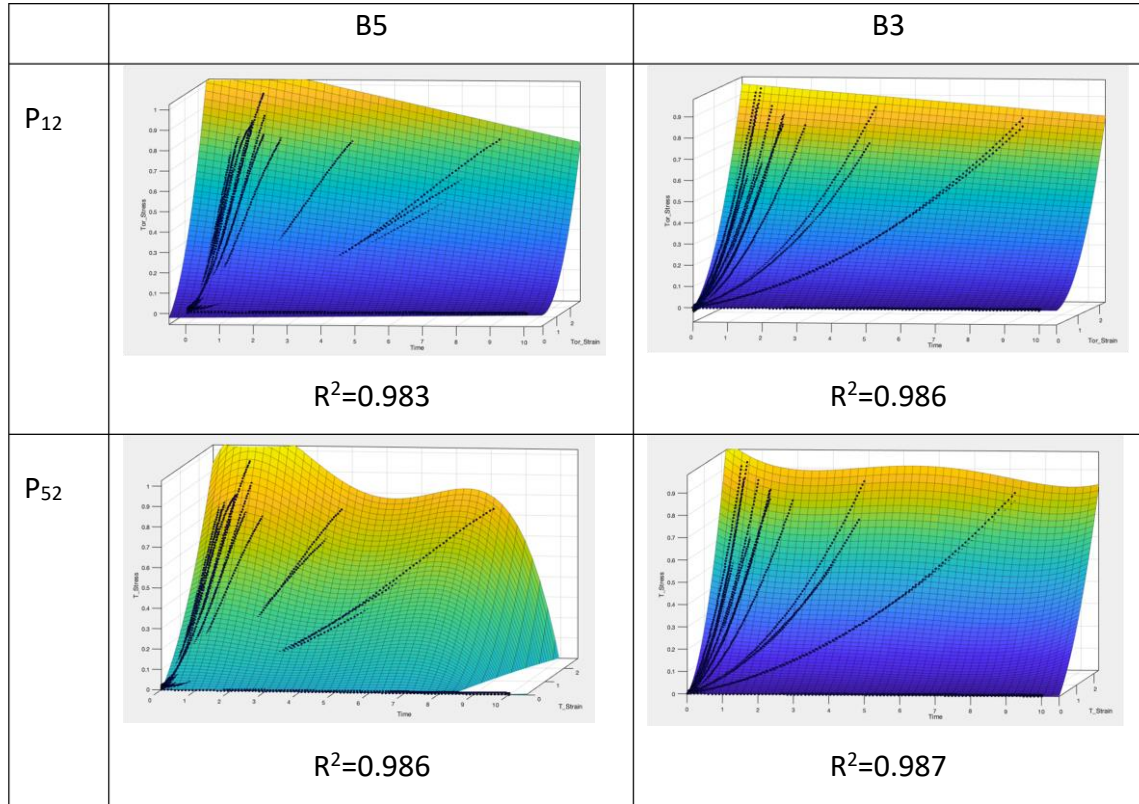
Figure 5-8: Viscoelastic surface P$_{12}$ & P$_{52}$ fits for B5 and B3 specimens test results with time <= 10 sec.

The time axes for all plots are 0→10s in 1s increments.

The torsional strain axes for all plots are 0→2 in 1 increment.

The torsional stress axes for B5 plots are 0→1MPa in 0.1MPa increments and for B3 are 0→0.9MPa in 0.1MPa increments.

Table 5-3: Coefficients for fit polynomials of B5 and B3.

p_{ij}	B5		B3	
	P_{12}	P_{52}	P_{12}	P_{52}
p_{00}	-0.001535	-0.004403	-0.0004806	-0.00305
p_{10}	0.0002446	0.005504	0.0001078	0.004904
p_{01}	0.1312	0.1442	0.08455	0.08792
p_{20}		-0.002975		-0.002504
p_{11}	-0.01351	-0.001191	-0.005734	-0.01835
p_{02}	0.1006	0.07259	0.1442	0.1571
p_{30}		0.0007398		0.0005582
p_{21}		-0.02792		0.007346
p_{12}		0.0466		-0.01889
p_{40}		-8.21e-05		-5.599e-05
p_{31}		0.008948		-0.001752
p_{22}		-0.01686		0.006244
p_{50}		3.304e-06		2.07e-06
p_{41}		-0.0006975		0.000123
p_{32}		0.001392		-0.0004864

5.4   Discussion

5.4.1   Effect of fiber content and orientation on the torsional strength of the specimens.

As stated in Section 5.3.2.1, the hypothesis on the monotonous increasing of torsional strength with increasing fiber content has not been validated experimentally. Comparing the peak torsional strength of B5 and B3 at strain = 2.0 (Figure 5-7 plot B & D) and strain-rate=1.76/s are roughly the same. This shows that the fiber content has little effect on the torsional strength of the specimens.

The original idea of embedding fibers circumferentially to increase the torsional strength of the specimens is, when the specimen is under torsion, the rotation will extend the fibers in each layer of the composite material to provide a tensile strength to resist the torque applied. However, the geometric shrinkage introduced by the PVA cryogel process has introduced an unknown effect on the torsional strength of the specimens. For compression, it has shown a strain shift effect on its compressive strength (Sections 4.4.3 & 4.4.4) due to the circumferential wrinkled fibers. The compression has theoretically unstretched the fibers in the mid portion of the prosthesis body. Under the same assumption, the fibers have to be fully unwrinkled before they can start to provide the tensile strength expected. Consider one fiber on the outer-circumference of the specimen and for one circumferential length, if r_o is the initial radius of the specimen and r_s is the shrunk radius after the PVA cryogel process ($r_s <= r_o$), then to un-wrinkle this fiber, one has to rotate the top surface of the slice of the specimen where the fiber is embedded in by an angle θ along the orientation of the fiber. θ (in radian) can be determined by this relation: $(2\pi + \theta)r_s = 2\pi r_o$,

Giving: $\theta = 2\pi \left(\dfrac{r_o}{r_s} - 1 \right)$.

Taking the mean values from Table 5-2, $r_o = 23mm/2$ and $r_s \approx \sqrt{ab/4} = \sqrt{20.2 * 19.8/4}$. This gives $\theta = 0.94 \, rad = 54^o$.

As the fibers are packed in the mold, one circumferential travel of the fiber will be embedded into a very thin slice of the specimen. θ will be accumulated from all these thin slices from the bottom of the specimen to the top of the specimen. This means there have to be substantial rotation (i.e., torsional strain) of the specimen before the fibers can reach the unwrinkled state to produce torsional strength. This may explain the low torsional stress measured from the specimens even at high strain value [Figure 5-6]. This may also explain the reason why there are not many differences in torsional stress values between the three batches of different fiber contents. Because of the non-contributing fiber, the specimens with zero fiber contents (B3) had shown a slightly higher torsional strength than those in B4 & B5 under the strain-rates tested in.

In this research, the aim was to evaluate the feasibility of the circumferentially embedded fiber concept. All specimens were prepared with fibers embedded in a fixed orientation following the right-hand-screw rule with thumb pointing upwards. All specimens were carefully tested with torsional strain applied in this direction. Under this construction, the torsional strength of the specimens is unidirectional. For real IVD prosthesis application, half of the fibers should be packed in another direction to provide bi-directional torsional strength. The fiber orientation should have no effect on the compressive strength. However, the shrinkage of the PVA matrix has to be solved before any possible torsional strength can be obtained.

No explanation can be found on the complex torsional strength vs strain-rate relationship as shown in Figure 5-7 plot B & D. The fiber in B5 seems to smooth out the peaks and valleys in the control B3. Fiber slippage or yield due to tensional stresses may be factors to consider to explain the rise and fall of torsional strength vs strain-rate in B5. However, the reasons for the variations of torsional strength vs strain-rate in B3 still need further investigation.

5.4.2 Suitability of specimens for IVD prosthesis material

The compressive properties measured in Section 4.3 & 4.4 have shown that the prosthesis specimens with 3v% fiber contents have comparable compressive strength as the kangaroo specimens measured after applying a pre-strain value about 35% to 45%

(Section 4.4.4). As the hypothesis on monotonous increasing compressive strength vs fiber contents has been validated (Section 4.3.4), by increasing the fiber content to about 5v% to 10v% will increase the compressive strength of the specimens and decreases the pre-strain value required to match that of the kangaroo specimens. The specimen material is feasible for supporting the upper body weight required by the IVD.

The torsional properties measured in Section 5.3.2 has shown that the specimen material has very low torsional strength. The properties measured was under no pre-strain condition. The fiber content does not substantially increase the torsional strength of the pure PVA cryogel (Section 5.4.1). Even though it has little torsional strength, it can withstand a high torsional strain (> 2.5) without yield. Comparing with the torsional yield strain of 0.66 for kangaroo specimens (Table 3-4), the material is more than adequate to provide the torsional strain required for an IVD prosthesis.

Combining the compressive and torsional properties, the material is functionally comparable with those FDA approved IVD prostheses such as the ProDisc-C[95] and Prestige ST[12,94]. In addition, the material candidate can provide extensive mobile-core rotational kinematics, important for cervical disc arthroplasty[24], not supported by these protheses.

5.5   Conclusion & Future works

Unlike the compressive strength, the torsional strength does not increase monotonously with the fiber content. It is essentially the same as that of straight 10% PVA cryogel. There is a doubt that the lack of torsional strength may be due to the shrinkage introduced by the PVA cryogel process. With a 35% to 45% pre-strain condition applied, the fibers in the mid portion of the specimens may be stretched to remove the wrinkle introduced by the PVA shrinkage. Torsional test conducted under this condition may eliminate this doubt. This is left for future research work.

<div align="center">Chapter 6</div>

6 Conclusion and Future Work

This Chapter provides a short recapitulation of this research including motivation, objectives, results obtained and final conclusion. A summary of the contributions of this research is included. Recommendations for future works is also provided.

6.1 Summary of Research

6.1.1 Motivation and Goal

Many of the CDA devices have been developed within the last 30 years to improve on the clinical outcomes of the standard ACDF approach. Their main goal, apart from the primary function to treat pain originated from myelopathy and radiculopathy, is to improve the patient's quality of life by providing improved range of mobility. Earlier designs following the Bristol-Cummins disc concept using a ball-and-socket construction to provide 3 degrees of rotational freedom. More recent ones employ a polycarbonate urethane (PCU) core to provide 6 degrees of freedom (DOF) to mimic the natural mechanical and material properties of the human IVD. Due to the material properties of the PCU, these CDA devices may provide some degree of viscoelasticity. Even though with the added new degree of freedom, many papers in the literature had reported incidents of heterotopic ossification (HO) and adjacent segment degeneration/disease (ASD). The literature reviews in Chapter 2 have pointed to the same observation and also shown that the number of incidents and severity may increase in time. Unfortunately, their cause(s) are still unknown.

This research has hypothesized on these outcomes may be attributed to the mismatched footprints to the vertebrae endplates, mismatched material properties to a healthy IVD and the injuries introduced to the vertebrae endplates due to their intrusive fixation methods.

This research has proposed a new prosthesis that can be made patient specific to match the size and shape of the vertebrae endplates involved. This will leave no room for HO to develop. The material properties should be viscoelastic to provide shock absorption

properties and 6 DOF. Its strength can be fine-tuned with simple parameters to match that of the human IVD. This will reduce abnormal stresses introduced by the prosthesis, hence will reduce the chance of ASD development. It should employ a non-intrusive fixation method to minimize the injuries introduced to the vertebrae body, hence will eliminate the triggering of the remodeling process of vertebrae which may result in HO development.

The material proposed is a composite made from 10wt% polyvinyl alcohol cryogel (PVA) with embedded long and circumferentially-oriented bamboo fibers. The material can be molded into any required shape via a suitable mold through the freeze-thaw process.

Theoretically when such a specimen is under compression, as its height decreases the middle of the specimen will enlarge putting the circumferentially- and helically-oriented embedded fibers in tension. This will enhance the compressive strength of the specimen. When it is under torsion, the rotational torque will put the embedded fibers under tension to provide torsional strength. Such a specimen will have 6 DOF in motion and variable instantaneous center of rotation.

The goal of this research is to validate if this new material can be a viable material for a cervical IVD prosthesis material.

6.1.2   Results summary

Due to the scarcity of the human cervical IVD data in the literature tested under similar conditions, the C5-C6 IVD of kangaroo was used as our animal model and the data extracted served as the gold standard for comparison with the prosthesis specimens prepared. In comparison with the human IVD from data in the literature, though inconclusive, this study had shown that the compressive strength of kangaroo IVD and human IVD were in the same order of magnitude.

The experimental results of the prosthesis specimens had shown that the material is compressive viscoelastic, i.e., strength increases with compressive strain-rate. The compressive strength increases with the volumetric fiber content, i.e., the material

compressive strength can be fine-tuned by changing the volumetric content of fibers to match the required strength of any IVD. The compressive strength of the specimens with 3v% fiber content measured is found lower than that of the model prediction by about 40% (between a strain value of 0.3 to 0.6). This may be attributed to the 37% volumetric and/or 21% cross-sectional area shrinkages of the 10wt% PVA matrix material putting the embedded fibers in a wrinkle state. The embedded fibers will not contribute to the compressive strength of the specimen until the cross-sectional area at mid height of the specimen enlarge enough to unwrinkled the fibers at that section. For the specimens with 3v% fiber content, it was found a 35% to 45% pre-strain value of the specimen can match the compressive stress-strain curves of the kangaroo IVD at a wide range of strain-rates. Hence by increasing the bamboo fiber content to, say, 5v%, a lower pre-strain value can be achieved to match the same requirement of the kangaroo IVD.

The experimental test data had shown all specimens had very weak torsional strength. No trend was found between specimens with different fiber contents. However, no yield condition detected in any of the specimen up to the maximum rotation (-15° to +90°, about a torsional strain value of 2.5). The specimens were found to have a complex torsional stress vs torsional strain-rate relationship. The torsional stress for the specimens with 3v% fiber content was found to increase with strain-rate initially until a peak value around 1.8/s strain-rate and dropped back down slowly. No logical explanation of this behavior was found at present. As for the weak torsional strength, similar to the compression case, it can be attributed to the 41% volumetric and 24% cross-sectional area shrinkages of the specimens. Only under a substantial rotation (about 54° per layer of fiber accumulating from the bottom to the top of the specimen) before the fibers can be unwrinkled to provide the rotational strength required.

6.1.3   Conclusion

The positive attributes of the proposed composite material to be used as an IVD prosthesis material are:

1. It can be molded into any shape and size required to conform with the cervical IVD requirement at any location and for any patient.

2. Its compressive strength can be tuned to match that of any health IVD by simply changing its fiber content.

3. It is resistive viscoelastic. It can provide shock absorption.

4. It can provide 6 DOF in motion and can permit variable instantaneous center of rotation of the attached vertebrae.

5. The pre-strain requirement may reduce the surgeon's work in preparing the fixation site. Even the specimen is molded with flat top and bottom surfaces, it will expand automatically to conform with the contours of the attached superior and inferior vertebrae endplates.

6. It is cost effective and can be made in about a week.

The drawbacks of the proposed composite material are:

1. It lacks the torsional strength required. This may put the burden on the surrounding tissues.

2. The PVA shrinkage may introduce technical challenges in the mold design to fit a specific shape and size required. A compensation strategy has to be developed to counteract with the volumetric and area shrinkage.

3. For a given required disc height, the pre-strain requirement will put additional complications on the mold design.

4. Among the 6 DOF, this research had tested only two DOF and found only the cranial compression motion has shown to have restorative resistance to motion. Very little resistance to motion was found on cranial rotation. The other 4 degrees of motion had not been tested, hence unknown.

Taking all the pros and cons of this material in consideration, an IVD prosthesis made from this material will mimic our natural IVD behavior better than those in the market using a ball-and-socket design. Both types will have 3 degrees of rotational freedom with

no torsional resistance. On top of this, the proposed material is simple in design and construction, will provide 6 DOFs in motion, 1 DOF with resistive viscoelastic property and variable instantaneous center of rotation. In conclusion, this material, though improvements may still be needed, is a suitable material candidate for IVD prosthesis.

6.2   Major Research Contributions

In biomedical application, this research has demonstrated that the proposed composite material, even though lacks torsional strength but has sufficient compressive strength, can become a viable cervical IVD prosthesis material. It is also very cost effective. This can benefit patients in parts of the world that cost of the prosthesis may be a prohibiting factor preventing them from receiving a suitable CDA treatment.

Another contribution of this research is in the area of modeling and analyzing the mechanical properties of viscoelastic materials, including but not limited to IVD. This is necessary because the mechanical behaviors of viscoelastic materials in many areas are typically poorly or insufficiently defined in the literature.

This research has proposed to use a multivariable polynomial to formulate the stress behavior of a viscoelastic object under the influences of strain and time and employed a least-square surface fitting method to extract the coefficients of this polynomial from a set of experimental test data. The resulting surface is tentatively called a "viscoelastic surface" in this research. A 3-d plot of the stress over strain and time is not a new concept. However, the proposed multivariable polynomial method has provided a good mathematical description of the mechanical behavior of a viscoelastic material. Basing on this mathematical model, other properties (such as impact resistance) can be derived analytically. The viscoelastic surface can model the mechanical behavior of both linear and nonlinear viscoelastic materials. This may be a better method over the Prony series which is limited to linear viscoelastic materials only. The Prony series method is widely used in current finite element modeling software. The multivariable polynomial approach can be further extended to cover other independent variables (such as temperature) that can influence the stress behavior of a viscoelastic material. The viscoelastic surface can be treated as a unifying mechanical behavior model of the material, through which, all

traditional methods (such as sets of stress-relaxing, creep and constant strain-rate curves) can be derived from it.

The torsional behavior of a material is traditionally derived through its shear modulus G by integrating the effect on an infinitesimal layer from the bottom of the object to the top. This derivation is good for a linear material in which G is a constant. However, for a non-linear material, G is shear strain dependent and not a constant. A viscoelastic material provides even further complications, G is also strain-rate dependent. The derivation, if possible, becomes very complicated. A more direct approach would be through torsional stress and torsional strain similar to compression and shear. However, these two mechanical properties are not well defined in the literature. This research has proposed new definitions for these two mechanical properties with the geometry of the object taken into account. They are defined in such a way that the area under the torsional stress-strain curve measures the work-done on (energy absorbed by) the object by the torsional force applied. This is exactly the same as in the compression and shear cases. A new material property, torsional modulus, is also defined accordingly (hopefully it should be dimensional independent like the Young's and shear modulus but have not been validated in this research). With the new definitions, all energy-based derivations (e.g., impact resistance) for the compression or shear can be applied equally to the torsion case.

How to quantify the impact resistance of a viscoelastic object when subject to an external impact force (compressive, shear or torsional) is not well defined in the literature. It is because this value is dependent on the waveform (magnitude and time) of the impact force interacting with the strain and strain-rate dependent behavior of the object. This research has proposed a definition for this property and the method to derive it analytically from the viscoelastic surface of the object. Using an impact force with a simple sawtooth waveform as an example, this research has demonstrated the method proposed to evaluate the impact resistance of the kangaroo C5-C6 IVD. Impact resistance is an important attribute for researches on injuries involving in an automotive accident and the design of related personal protective equipment. Hopefully this research can contribute to the improvements on these researches in future.

The new material properties and derivation methods proposed in this research are just an initial attempt to formulate these concepts in better forms. Hoping future researchers can continue to improve on these so that one day we all can have better understanding on the behavior of more complex viscoelastic objects like the human body.

6.3 Future work

The key factor preventing the material to achieve its theoretical strength is the shrinkage of the PVA. Future research effort should address this issue. It may be necessary to replace the PVA with a biocompatible and stable matrix material with zero or little shrinkage.

In outlining the scope of this research, Chapter 1 has identified two out-of-scope areas that were explicitly excluded from current research domain. Reasons for the exclusion were explained. Future research efforts should address these areas.

This research had only studied the strength of 2 of the 6 DOFs provided by our IVD to conserve research effort. Future research efforts should cover the characterization of the other 4 DOFs to complete the coverage.

Current clinical studies mainly measure the flexion-extension ROM to access the quality of motion of the patients. This may not be a good yardstick. Movements with a combination of compression, torsion and translation in different direction may provide a better measure to access the quality of motion for the patients treated with CDA.

References

1. Alhashash M, Shousha M, Boehm H. Adjacent Segment Disease after Cervical Spine Fusion. *Spine (Phila Pa 1976)*. 2018;43(9):605-609. doi:10.1097/BRS.0000000000002377

2. Delamarter RB, Zigler J. Five-year reoperation rates, cervical total disc replacement versus fusion, results of a prospective randomized clinical trial. *Spine (Phila Pa 1976)*. 2013;38(9):711-717. doi:10.1097/BRS.0b013e3182797592

3. Staudt MD, Das K, Duggal N. Does design matter? Cervical disc replacements under review. *Neurosurg Rev*. 2018;41(2):399-407. doi:10.1007/s10143-016-0765-0

4. Stanton P, Eck JC. Materials and design characteristics of cervical arthroplasty devices. *Tech Orthop*. 2010;25(2):93-96. doi:10.1097/BTO.0b013e3181df2ef3

5. Mehren C, Heider F, Sauer D, et al. Clinical and Radiological Outcome of a New Total Cervical Disc Replacement Design. *Spine (Phila Pa 1976)*. 2019;44(4):E202-E210. doi:10.1097/BRS.0000000000002799

6. Veruva SY, Steinbeck MJ, Toth J, Alexander DD, Kurtz SM. Which Design and Biomaterial Factors Affect Clinical Wear Performance of Total Disc Replacements? A Systematic Review. *Clin Orthop Relat Res*. 2014;472(12):3759-3769. doi:10.1007/s11999-014-3751-2

7. Yan SZ, Di J, Shen Y. Adjacent segment degeneration following anterior cervical discectomy and fusion versus the bryan cervical disc arthroplasty. *Med Sci Monit*. 2017;23:2692-2700. doi:10.12659/MSM.905178

8. Zou S, Gao J, Xu B, Lu X, Han Y, Meng H. Anterior cervical discectomy and fusion (ACDF) versus cervical disc arthroplasty (CDA) for two contiguous levels cervical disc degenerative disease: a meta-analysis of randomized controlled trials. *Eur Spine J*. 2017;26(4):985-997. doi:10.1007/s00586-016-4655-5

9.   Coric D, Kim PK, Clemente JD, Boltes MO, Nussbaum M, James S. Prospective randomized study of cervical arthroplasty and anterior cervical discectomy and fusion with long-term follow-up: Results in 74 patients from a single site - Presented at the 2012 Joint Spine Section Meeting. Clinical article. *J Neurosurg Spine*. 2013;18(1):36-42. doi:10.3171/2012.9.SPINE12555

10. Verma K, Gandhi SD, Maltenfort M, et al. Rate of adjacent segment disease in cervical disc arthroplasty versus single-level fusion: Meta-analysis of prospective studies. *Spine (Phila Pa 1976)*. 2013;38(26):2253-2257. doi:10.1097/BRS.0000000000000052

11. MacDowall A, Canto Moreira N, Marques C, et al. Artificial disc replacement versus fusion in patients with cervical degenerative disc disease and radiculopathy: A randomized controlled trial with 5-year outcomes. *J Neurosurg Spine*. 2019;30(3):323-331. doi:10.3171/2018.9.SPINE18659

12. Burkus JK, Traynelis VC, Haid RW, Mummaneni P V. Clinical and radiographic analysis of an artificial cervical disc: 7-year follow-up from the Prestige prospective randomized controlled clinical trial. *J Neurosurg Spine*. 2014;21(4):516-528. doi:10.3171/2014.6.SPINE13996

13. Quan GMY, Vital JM, Hansen S, Pointillart V. Eight-year clinical and radiological follow-up of the bryan cervical disc arthroplasty. *Spine (Phila Pa 1976)*. 2011;36(8):639-646. doi:10.1097/BRS.0b013e3181dc9b51

14. Byval'tsev VA, Kalinin AA, Stepanov IA, Pestryakov YY, Shepelev V V. Analysis of the results of total cervical disc arthroplasty using a M6-C prosthesis: a multicenter study. *Vopr neirokhirurgii Im NN Burdenko*. 2017;81(5):46. doi:10.17116/neiro201781546-55

15. Pham M, Phan K, Teng I, Mobbs RJ. Comparative Study Between M6-C and Mobi-C Cervical Artificial Disc Replacement: Biomechanical Outcomes and Comparison with Normative Data. *Orthop Surg*. 2018;10(2):84-88. doi:10.1111/os.12376

16. Lazennec J yves, Aaron A, Ricart O, Rakover JP. The innovative viscoelastic CP ESP cervical disk prosthesis with six degrees of freedom: biomechanical concepts, development program and preliminary clinical experience. *Eur J Orthop Surg Traumatol*. 2016;26(1):9-19. doi:10.1007/s00590-015-1695-1

17. Zhao Y, Zhang Y, Sun Y, Pan S, Zhou F, Liu Z. Application of cervical arthroplasty with bryan cervical disc 10-year follow-up results in China. *Spine (Phila Pa 1976)*. 2016;41(2):111-115. doi:10.1097/BRS.0000000000001145

18. Pointillart V, Castelain JE, Coudert P, Cawley DT, Gille O, Vital JM. Outcomes of the Bryan cervical disc replacement: fifteen year follow-up. *Int Orthop*. 2018;42(4):851-857. doi:10.1007/s00264-017-3745-2

19. Gornet MF, Burkus JK, Shaffrey ME, Schranck FW, Copay AG. Cervical disc arthroplasty: 10-year outcomes of the Prestige LP cervical disc at a single level. *J Neurosurg Spine*. 2019;31(3):317-325. doi:10.3171/2019.2.SPINE1956

20. Miller J, Sasso R, Anderson P, Riew KD, McPhilamy A, Gianaris T. Adjacent Level Degeneration. *Clin Spine Surg*. 2018;31(2):E98-E101. doi:10.1097/bsd.0000000000000598

21. Radcliff K, Lerner J, Yang C, Bernard T, Zigler JE. Seven-year cost-effectiveness of ProDisc-C total disc replacement: Results from investigational device exemption and post-approval studies. *J Neurosurg Spine*. 2016;24(5):760-768. doi:10.3171/2015.10.SPINE15505

22. Putzier M, Funk JF, Schneider S V., et al. Charité total disc replacement - Clinical and radiographical results after an average follow-up of 17 years. *Eur Spine J*. 2006;15(2):183-195. doi:10.1007/s00586-005-1022-3

23. Jin YJ, Park SB, Kim MJ, Kim KJ, Kim HJ. An analysis of heterotopic ossification in cervical disc arthroplasty: A novel morphologic classification of an ossified mass. *Spine J*. 2013;13(4):408-420. doi:10.1016/j.spinee.2012.11.048

24. Zeng J, Liu H, Chen H, et al. Comparison of Heterotopic Ossification After Fixed-

and Mobile-Core Cervical Disc Arthroplasty. *World Neurosurg*. 2018;120:e1319-e1324. doi:10.1016/j.wneu.2018.09.075

25.   McAfee PC, Cunningham BW, Devine J, Williams E, Yu-Yahiro J. Classification of heterotopic ossification (HO) in artificial disk replacement. *J Spinal Disord Tech*. 2003;16(4):384-389. doi:10.1097/00024720-200308000-00010

26.   Zhou F, Ju KL, Zhao Y, et al. Progressive bone formation after cervical disc replacement: Minimum of 5-year follow-up. *Spine (Phila Pa 1976)*. 2018;43(3):E163-E170. doi:10.1097/BRS.0000000000002264

27.   Yanbin Z, Yu S, Zhongqiang C, Zhongjun L. Sagittal alignment comparison of Bryan disc arthroplasty with ProDisc-C arthroplasty: A prospective, randomized controlled clinical trial. *J Spinal Disord Tech*. 2011;24(6):381-385. doi:10.1097/BSD.0b013e318201855f

28.   Li C, Granger C, Del Schutte H, Biggers SB, Kennedy JM, Latour RA. Failure analysis of composite femoral components for hip arthroplasty. *J Rehabil Res Dev*. 2003;40(2):131-145. doi:10.1682/jrrd.2003.03.0133

29.   Bennett D., Hill J., Dennison J, et al. Metal-Carbon Fiber Composite Femoral Stems in Hip Replacements. *J Bone Jt Surgery-American Vol*. 2014;96(24):2062-2069. doi:10.2106/jbjs.m.01542

30.   Oxland TR. Fundamental biomechanics of the spine-What we have learned in the past 25 years and future directions. *J Biomech*. 2016;49(6):817-832. doi:10.1016/j.jbiomech.2015.10.035

31.   Anderst W, Baillargeon E, Donaldson W, Lee J, Kang J. Motion path of the instant center of rotation in the cervical spine during in vivo dynamic flexion-extension: Implications for artificial disc design and evaluation of motion quality after arthrodesis. *Spine (Phila Pa 1976)*. 2013;38(10). doi:10.1097/BRS.0b013e31828ca5c7

32.   Tetreault L, Kopjar B, Nouri A, et al. The modified Japanese Orthopaedic

Association scale: establishing criteria for mild, moderate and severe impairment in patients with degenerative cervical myelopathy. *Eur Spine J*. 2017;26(1):78-84. doi:10.1007/s00586-016-4660-8

33. KELLGREN JH, LAWRENCE JS. Radiological assessment of osteo-arthrosis. *Ann Rheum Dis*. 1957;16(4):494-502. doi:10.1136/ard.16.4.494

34. Broekema AEH, Molenberg R, Kuijlen JMA, Groen RJM, Reneman MF, Soer R. The Odom Criteria: Validated at Last: A Clinimetric Evaluation in Cervical Spine Surgery. *J Bone Jt Surg - Am Vol*. 2019;101(14):1301-1308. doi:10.2106/JBJS.18.00370

35. Delgado DA, Lambert BS, Boutris N, et al. Validation of Digital Visual Analog Scale Pain Scoring With a Traditional Paper-based Visual Analog Scale in Adults. *JAAOS Glob Res Rev*. 2018;2(3):e088. doi:10.5435/jaaosglobal-d-17-00088

36. Food and Drug Administration. *P060023A Premarket Approval (BRYAN Cervical Disc)*.(2009). www.fda.gov.

37. Food and Drug Administration. *P060023B Summary of Safety and Effectiveness Data (BRYAN Cervical Disc)*.(2009). www.fda.gov.

38. Cheng L, Nie L, Li M, Huo Y, Pan X. Superiority of the Bryan ® disc prosthesis for cervical myelopathy: A randomized study with 3-year followup. *Clin Orthop Relat Res*. 2011;469(12):3408-3414. doi:10.1007/s11999-011-2039-z

39. Han X, He D, Zhang N, Song Q, Wang J, Tian W. Comparison of 10-year Outcomes of Bryan Cervical Disc Arthroplasty for Myelopathy and Radiculopathy. *Orthop Surg*. 2019;11(6):1127-1134. doi:10.1111/os.12565

40. Lavelle WF, Riew KD, Levi AD, Florman JE. Ten-year Outcomes of Cervical Disc Replacement with the BRYAN Cervical Disc: Results from a Prospective, Randomized, Controlled Clinical Trial. *Spine (Phila Pa 1976)*. 2019;44(9):601-608. doi:10.1097/BRS.0000000000002907

41. Food and Drug Administration. *P170036A Premarket Approval (M6-C)*.(2019). www.fda.gov.

42. Food and Drug Administration. *P170036B Summary of Safety and Effectiveness Data (M6-C)*.(2019). www.fda.gov.

43. Lauryssen C, Coric D, Dimmig T, Musante D, Ohnmeiss DD, Stubbs HA. Cervical total disc replacement using a novel compressible prosthesis: Results from a prospective Food and Drug Administration-regulated feasibility study with 24-month follow-up. *Int J Spine Surg*. 2012;6(1):71-77. doi:10.1016/j.ijsp.2012.02.001

44. Food and Drug Administration. *P060018A Premarketing Approval (Prestige-ST)*.(2007). www.fda.gov.

45. Food and Drug Administration. *P060018B Summary of Safety and Effectiveness Data (Pestige-ST)*.(2007). www.fda.gov.

46. Mummaneni P V., Burkus JK, Haid RW, Traynelis VC, Zdeblick TA. Clinical and radiographic analysis of cervical disc arthroplasty compared with allograft fusion: A randomized controlled clinical trial. *J Neurosurg Spine*. 2007;6(3):198-209. doi:10.3171/spi.2007.6.3.198

47. Mummaneni P V., Haid RW, Zdeblick TA, Burkus JK, Traynelis VC. Three- and 5-year Results from a Prospective, Randomized United States Investigational Device Exemption Study of the PRESTIGE ST Cervical Disc. *Neurosurgery*. 2009;65(2):408-408. doi:10.1227/01.neu.0000358693.71422.3b

48. Food and Drug Administration. *P090029A Premarketing Approval (Prestige-LP)*.(2014). www.fda.gov.

49. Food and Drug Administration. *P090029B Summary of Safety and Effective Ness Data (Prestige-LP)*.(2014). www.fda.gov.

50. ASTM International. F2346-18: Standard Test Methods for Static and Dynamic

Characterization of Spinal Artificial Discs. doi:10.1520/F2346-18

51. Wu T, Wang B, Ding C, et al. Artificial cervical disc replacement with the Prestige-LP prosthesis for the treatment of non-contiguous 2-level cervical degenerative disc disease: A minimum 24-month follow-up. *Clin Neurol Neurosurg*. 2017;152:57-62. doi:10.1016/j.clineuro.2016.11.015

52. Li G, Wang Q, Liu H, Yang Y. Postoperative Heterotopic Ossification After Cervical Disc Replacement Is Likely a Reflection of the Degeneration Process. *World Neurosurg*. 2019;125:e1063-e1068. doi:10.1016/j.wneu.2019.01.244

53. Miyazaki M, Hong SW, Yoon SH, Morishita Y, Wang JC. Reliability of a magnetic resonance imaging-based grading system for cervical intervertebral disc degeneration. *J Spinal Disord Tech*. 2008;21(4):288-292. doi:10.1097/BSD.0b013e31813c0e59

54. Hu X, Jiang M, Liu H, et al. Five-Year Trends in Center of Rotation After Single-Level Cervical Arthroplasty with the Prestige-LP Disc. *World Neurosurg*. 2019;132:e941-e948. doi:10.1016/j.wneu.2019.07.042

55. Zeng J, Liu H, Rong X, et al. Clinical and radiographic outcomes of cervical disc arthroplasty with Prestige-LP Disc: a minimum 6-year follow-up study. *BMC Musculoskelet Disord*. 2018;19(1):1-7. doi:10.1186/s12891-018-2201-9

56. Orthopedics F. CP LP ESP documentation. https://spine-innovations.com/wp-content/uploads/2020/09/doc_cp_lp_esp_eng.pdf. Accessed March 27, 2021.

57. Orthopedics F. Material composition CP ESP. https://spine-innovations.com/wp-content/uploads/2020/09/ft_composition_disc_esp_eng.pdf. Accessed March 27, 2021.

58. Lazennec JY, Rischke B, Rakover JP, Ricart O, Rousseau MA. CP-ESP VISCOELASTIC CERVICAL DISC REPLACEMENT: TWO YEARS' FOLLOW-UP WITH CLINICAL AND RADIOLOGICAL RESULTS. EVOLUTION OF SEGMENTAL MOBILITY AND LOCATION OF MEAN

CENTRES OF ROTATION. Orthopaedic Proceedings. doi:10.1302/1358-992X.2019.5.096

59. Gloria A, Causa F, De Santis R, Netti PA, Ambrosio L. Dynamic-mechanical properties of a novel composite intervertebral disc prosthesis. *J Mater Sci Mater Med*. 2007;18(11):2159-2165. doi:10.1007/s10856-007-3003-z

60. Yang H, Jekir MG, Davis MW, Keaveny TM. Effective modulus of the human intervertebral disc and its effect on vertebral bone stress. *J Biomech*. 2016;49(7):1134-1140. doi:10.1016/j.jbiomech.2016.02.045

61. Panjabi MM, Summers DJ, Pelker RR, Videman T, Friedlaender GE, Southwick WO. Three-dimensional load-displacement curves due to force on the cervical spine. *J Orthop Res*. 1986;4:152-161.

62. Gloria A, De Santis R, Ambrosio L, Causa F, Tanner KE. A multi-component fiber-reinforced PHEMA-based hydrogel/HAPEXTM device for customized intervertebral disc prosthesis. *J Biomater Appl*. 2011;25(8):795-810. doi:10.1177/0885328209360933

63. McLeod A. NeoDisc. https://www.healthinnovationsupport.co.uk/experience/. Accessed April 3, 2021.

64. Jacobs CAM, Siepe CJ, Ito K. Viscoelastic cervical total disc replacement devices: Design concepts. *Spine J*. 2020;20(12):1911-1924. doi:10.1016/j.spinee.2020.08.007

65. NuVasive. Evaluating The Safety and Effectiveness of The NeoDisc[TM] Versus ACDF in Subjects With Single-Level Cervical Disc Disease (NeoDisc[TM]). https://www.clinicaltrials.gov/ct2/show/NCT00478088. Accessed April 3, 2021.

66. Pettine KA. Clinical and Radiographic Outcome of the NeoDisc Cervical Total Disc Replacement (TDR) at 2-Year Follow-up. *Spine J*. 2010;10(9):S44. doi:10.1016/j.spinee.2010.07.123

67. Mummaneni P V., Robinson JC, Haid RW. Cervical arthroplasty with the PRESTIGE LP cervical disc. *Neurosurgery*. 2007;60(4 SUPPL. 2):310-315. doi:10.1227/01.NEU.0000255376.42099.13

68. Kim DH. *Dynamic Reconstruction of the Spine* . 2nd ed. Stuttgart, [Germany: Thieme; 2015.

69. Radcliff K, Davis RJ, Hisey MS, et al. Long-term evaluation of cervical disc arthroplasty with the Mobi-C© cervical disc: A randomized, prospective, multicenter clinical trial with seven-year follow-up. *Int J Spine Surg*. 2017;11(4):244-262. doi:10.14444/4031

70. Brenke C, Schmieder K, Barth M. Core herniation after implantation of a cervical artificial disc: case report. *Eur Spine J*. 2015;24:536-539. doi:10.1007/s00586-014-3677-0

71. White A, Panjabi M. *Clinical Biomechanics of the Spine*. 2nd ed. J.B. Lippincott Company; 1990.

72. Showalter BL, Beckstein JC, Martin JT, et al. Comparison of animal discs used in disc research to human lumbar disc: Torsion mechanics and collagen content. *Spine (Phila Pa 1976)*. 2012;37(15). doi:10.1097/BRS.0b013e31824d911c

73. Espinoza Orías AA, Mammoser NM, Triano JJ, An HS, Andersson GBJ, Inoue N. Effects of Axial Torsion on Disc Height Distribution: An in Vivo Study. *J Manipulative Physiol Ther*. 2016;39(4):294-303. doi:10.1016/j.jmpt.2016.03.002

74. Bezci SE, Eleswarapu A, Klineberg EO, O'Connell GD. Contribution of facet joints, axial compression, and composition to human lumbar disc torsion mechanics. *J Orthop Res*. 2018;36(8):2266-2273. doi:10.1002/jor.23870

75. Wilke HJ, Krischak S, Claes L. Biomechanical comparison of calf and human spines. *J Orthop Res*. 1996;14(3):500-503. doi:10.1002/jor.1100140321

76. Wen N, Lavaste F, Santin JJ, Lassau JP. Three-dimensional biomechanical

properties of the human cervical spine in vitro. I. Analysis of normal motion . *Eur spine J Off Publ Eur Spine Soc Eur Spinal Deform Soc Eur Sect Cerv Spine Res Soc* . 1993;2(1):2-11. doi:10.1007/BF00301048

77.   Bezci SE, Klineberg EO, O'Connell GD. Effects of axial compression and rotation angle on torsional mechanical properties of bovine caudal discs. *J Mech Behav Biomed Mater*. 2018;77(June 2017):353-359. doi:10.1016/j.jmbbm.2017.09.022

78.   Nikkhoo M, Wang JL, Parnianpour M, El-Rich M, Khalaf K. Biomechanical response of intact, degenerated and repaired intervertebral discs under impact loading – Ex-vivo and In-Silico investigation. *J Biomech*. 2018;70:26-32. doi:10.1016/j.jbiomech.2018.01.026

79.   Dudli S, Haschtmann D, Ferguson SJ. Fracture of the vertebral endplates, but not equienergetic impact load, promotes disc degeneration in vitro. *J Orthop Res*. 2012;30(5):809-816. doi:10.1002/jor.21573

80.   Chamis CC, Hanson MP, Serafini TT. Designing for impact resistance with unidirectional fiber composites. *Composites*. 2003. doi:10.1016/0010-4361(72)90390-4

81.   Van der Veen AJ, Bisschop A, Mullender MG, van Dieën JH. Modelling creep behaviour of the human intervertebral disc. *J Biomech*. 2013;46(12):2101-2103. doi:10.1016/j.jbiomech.2013.05.026

82.   Cassidy JJ, Hiltner A, Baer E. The response of the hierarchical structure of the intervertebral disc to uniaxial compression. *J Mater Sci Mater Med*. 1990;1(2):69-80. doi:10.1007/BF00839071

83.   Smit TH. The use of a quadruped as an in vivo model for the study of the spine - Biomechanical considerations. *Eur Spine J*. 2002;11(2):137-144. doi:10.1007/s005860100346

84.   Wilke HJ, Geppert J, Kienle A. Biomechanical in vitro evaluation of the complete porcine spine in comparison with data of the human spine. *Eur Spine J*.

2011;20(11):1859-1868. doi:10.1007/s00586-011-1822-6

85. Wang CS, Chang JH, Chang TS, Chen HY, Cheng CW. Loading effects of anterior cervical spine fusion on adjacent segments. *Kaohsiung J Med Sci*. 2012;28(11):586-594. doi:10.1016/j.kjms.2012.04.024

86. Ohnishi T, Sudo H, Tsujimoto T, Iwasaki N. Age-related spontaneous lumbar intervertebral disc degeneration in a mouse model. *J Orthop Res*. 2018;36(1):224-232. doi:10.1002/jor.23634

87. Panjabi MM, Duranceau J, Goel V, Oxland T, Takata K. Cervical human vertebrae. Quantitative three-dimensional anatomy of the middle and lower regions . *Spine* . 1991;16(8):861-869. doi:10.1097/00007632-199108000-00001

88. Busscher I, Ploegmakers JJW, Verkerke GJ, Veldhuizen AG. Comparative anatomical dimensions of the complete human and porcine spine. *Eur Spine J*. 2010;19(7):1104-1114. doi:10.1007/s00586-010-1326-9

89. Newell N, Little JP, Christou A, Adams MA, Adam CJ, Masouros SD. Biomechanics of the human intervertebral disc: A review of testing techniques and results. *J Mech Behav Biomed Mater*. 2017;69(January):420-434. doi:10.1016/j.jmbbm.2017.01.037

90. Barrientos E, Pelayo F, Noriega Á, Lamela MJ, Fernández-Canteli A, Tanaka E. Optimal discrete-time Prony series fitting method for viscoelastic materials. *Mech Time-Dependent Mater*. 2018:1-14. doi:10.1007/s11043-018-9394-z

91. Thomas S, Willems K, Van Den Daelen L, Linden P, Ciocci MC, Bocher P. The M6-C cervical disk prosthesis first clinical experience in 33 patients. *Clin Spine Surg*. 2016;29(4):E182-E187. doi:10.1097/BSD.0000000000000025

92. Lazennec JY, Aaron A, Brusson A, Rakover JP, Rousseau MA. The LP-ESP® lumbar disc prosthesis with 6 degrees of freedom: Development and 7 years of clinical experience. *Eur J Orthop Surg Traumatol*. 2013;23(2):131-143. doi:10.1007/s00590-012-1166-x

93.   Patwardhan AG, Havey RM. Prosthesis design influences segmental contribution to total cervical motion after cervical disc arthroplasty. *Eur Spine J*. 2019;(0123456789):1-9. doi:10.1007/s00586-019-06064-4

94.   Wu JC, Huang WC, Mummaneni P V. Prestige cervical arthroplasty. *Tech Orthop*. 2010;25(2):108-113. doi:10.1097/BTO.0b013e3181de1aa4

95.   Garg H, Ramachandran R, Yue J. ProDisc-C. *Tech Orthop*. 2010;25(2):118-126. doi:10.1097/BTO.0b013e3181df2f8e

96.   McAfee PC, Fedder IL, Saiedy S, Shucosky EM, Cunningham BW. SB Charité Disc Replacement. *J Spinal Disord Tech*. 2003;16(4):424-433. doi:10.1097/00024720-200308000-00016

97.   Qin G, Liu J, Xue Y, et al. Enhanced stability of antimicrobial bamboo fiber by launching ultra fine silver particles in a sodium dodecyl sulfate microemulsion system. *Text Res J*. 2017;87(20):2505-2512. doi:10.1177/0040517516673329

98.   Afrin T, Kanwar RK, Wang X, Tsuzuki T. Properties of bamboo fibres produced using an environmentally benign method. *J Text Inst*. 2014;105(12):1293-1299. doi:10.1080/00405000.2014.889872

99.   Liew FK, Hamdan S, Rahman MR, et al. Synthesis and characterization of cellulose from green bamboo by chemical treatment with mechanical process. *J Chem*. 2015;2015(March). doi:10.1155/2015/212158

100.   Pacheco CM, Bustos C, Reyes G, Aguayo MG, Rojas OJ. Characterization of Residues from Chilean Blueberry Bushes: A Potential Source of Cellulose. *BioResources*. 2018;13(4). doi:10.15376/biores.13.4.7345-7359

101.   Yueping W, Ge W, Haitao C, et al. Structures of Bamboo Fiber for Textiles. *Text Res J*. 2010;80(4):334-343. doi:10.1177/0040517509337633

102.   Afrin T, Tsuzuki T, Wang X. UV absorption property of bamboo. *J Text Inst*. 2012;103(4):394-399. doi:10.1080/00405000.2011.580543

103. Heller JG, Sasso RC, Papadopoulos SM, et al. Comparison of BRYAN cervical disc arthroplasty with anterior cervical decompression and fusion: Clinical and radiographic results of a randomized, controlled, clinical trial. *Spine (Phila Pa 1976)*. 2009;34(2):101-107. doi:10.1097/BRS.0b013e31818ee263

104. Sasso RC, Smucker JD, Hacker RJ, Heller JG. Clinical outcomes of BRYAN cervical disc arthroplasty: a prospective, randomized, controlled, multicenter trial with 24-month follow-up. *J Spinal Disord Tech*. 2007;20(7):481-491. doi:10.1097/BSD.0b013e3180310534

Curriculum Vitae

Name: Helium Mak

Post-secondary Education and Degrees: Hong Kong Polytechnic University
Hong Kong, China
1972-1974 Higher Diploma in Electronic Engineering
1975 Associateship in Electronic Engineering

Twickenham College of Technology
London Borough of Richmond upon Thames, UK
1977-1978 Diploma in Electrical, Electronic and Control Eng.

Brunel University
Uxbridge, London, UK
1978-1982 (Part-time) MSc in Digital System

Honours and Awards: Professional Engineer (P. Eng)
Professional Engineers Ontario, Canada
2016 - now

Related Work Experience Senior Research Officer
National Research Council Canada
1991-2015, Ottawa & London, Canada

Project Leader
Gandalf Data Limited
1989-1991, Ottawa, Canada

Product Development Manager
Bell Northern Research (Nortel)
1982-1989, Ottawa, Canada

Engineering Manager
Beale Electronics
1979-1982, London, UK

Development Engineer
Euromatic Flowmeter
1978-1979, London, UK

Laboratory Technician & Part-time Lecturer
Hong Kong Polytechnic University

1975-1977, Hong Kong, China.

Publications:

Wankei Wan, A Dawn Bannerman, Lifang Yang, Helium Mak. Poly (vinyl alcohol) cryogels for biomedical applications. Springer, Cham. Polymeric Cryogels (2014), 283-321